2015

Optical Fibers for Space-Division Multiplexed Transmission and Networking

Cen Xia
University of Central Florida

OPTICAL FIBERS FOR SPACE-DIVISION MULTIPLEXED TRANSMISSION AND NETWORKING

by

CEN XIA
B.S. Zhejiang University, China, 2009

A dissertation submitted in partial fulfillment of the requirements
for the degree of Doctor of Philosophy
in CREOL, The College of Optics & Photonics
at the University of Central Florida
Orlando, Florida

Summer Term
2015

Major Professor: Guifang Li

ABSTRACT

Single-mode fiber transmission can no longer satisfy exponentially growing capacity demand. Space-division multiplexing (SDM) appears to be the only way able to dramatically improve the transmission capacity, for which, novel optical fiber is one of the key technologies. Such fibers must possess the following characteristics: 1) high mode density per cross-sectional area and 2) low crosstalk or low modal differential group delay (DMGD) to reduce complexity of digital signal processing. In this dissertation, we explore the design and characterization of three kinds of fibers for SDM: few-mode fiber (FMF), few-mode multi-core fiber (FM-MCF) and coupled multi-core fiber (CMCF) as well as their applications in transmission and networking.

For the ultra-high density need of SDM, we have proposed the FMMCF. It combines advantages of both the FMF and MCF. The challenge is the inter-core crosstalk of the high-order modes. By applying a hole-assisted structure and careful fiber design, the LP_{11} crosstalk has been suppressed down to -40dB per km. This allows separate transmission on LP_{01} and LP_{11} modes without penalty. In fact, a robust SDM transmission up to 200Tb/s has been achieved using this fiber.

To overcome distributed modal crosstalk in conjunction with DMGD, supermodes in CMCFs have been proposed. The properties of supermodes were investigated using the coupled-mode theory. The immediate benefits include high mode density and large effective area. In supermode structures, core-to-core coupling is exploited to reduce modal crosstalk or minimize DMGD. In addition, higher-order supermodes have been discovered in CMCFs with few-mode

cores. We show that higher-order supermodes in different waveguide array configurations can be strongly affected by angle-dependent couplings, leading to different modal fields. Analytical solutions are provided for linear, rectangular and ring arrays. Higher-order modes have been observed for the first time using S^2 imaging method.

Finally, we introduce FMF to gigabit-capable passive optical networks (GPON). By replacing the conventional splitter with a photonic lantern, upstream combining loss can be eliminated. Low crosstalk has been achieved by a customized mode-selective photonic lantern carefully coupled to the FMF. We have demonstrated the first few-mode GPON system with error-free performance over 20-km 3-mode transmission using a commercial GPON system carrying live Ethernet traffic. We then scale the 3-mode GPON system to 5-mode, which resulted in a 4dB net gain in power budget in comparison with current commercial single-mode GPON systems.

Dedicated to my family.

ACKNOWLEDGMENTS

Throughout the six years of my Ph. D., I've received many helps. There is a saying, "if I have seen a little bit further it is by standing on the shoulders of giants," which I felt very true. Every of my subtle achievements came from a lot of assistances.

First of all, I'd like to thank my advisor, Dr. Guifang Li. His great insights and step-by-step guidance lead me into the field of fiber-optic communication. Dr. Li has been extremely patient and helpful during my Ph. D. study and research. His rigorous academic attitude, deep understanding and creative thinking have given me great influences. He has also provided me with precious opportunities to collaborate with top-level institutes and companies. During the collaboration, I was able to interact with prominent scholars. Without him, there is no way for me to finish my Ph. D. and enter my future professional career so smoothly.

I also would like to give my great thanks to Dr. Xiang Liu, who is my mentor during my internships in Bell Labs and Futurewei Technologies. I am so grateful that I had the chance to work so closely with such a talented and helpful scholar. He has given me a big impact not only in doing research but also how to work and live.

I'd like to thank Prof. Rodrigo Amezcua Correa and Dr. Jose Enrique Antonio-Lopez in particular, who collaborate with our group on many projects. They have taught me a lot about fiber design, fabrication and test. It wouldn't be possible for me to have these accomplishments if they are not here.

My mentors in Bell Labs, Dr. Nicolas K. Fontaine and Dr. Roland Ryf and my mentors in Futurewei Technologies, Dr. Frank Effenberger and Dr. Naresh Chand have given me

tremendous helps and guidance. Their enthusiasm and intelligence have motivated me to be more initiative and agile in research.

I feel grateful to be in our group, where we always help and support each other, including Dr. Xiaobo Xie, Dr. Ibrahim Ozdur, Dr. He Wen, Dr. Neng Bai, Dr. Likai Zhu, Bing Huang, Huiyuan Liu and all my previous group members.

I've received valuable suggestions and great encouragement from all the members of my dissertation committee: Prof. Ayman Abourady, Prof. Demetrios Christodoulides and Prof. M. G. "Jim" Moharam and Prof. Thomas Wu. In addition, Prof. Demetrios Christodoulides and M. Amin Eftekhar have made a great contribution to our invited paper about supermodes, which I do appreciate.

There are so many people I own thanks to during my Ph. D.. I can never forget Prof. Shin-Tson Wu and his wife Choyan Hsieh, who have taken care of me since the day I came to CREOL and walked me through the toughest days of my life. And all my friends in CREOL, who lent me equipment, shared knowledge with me and colored my life over the years.

Lastly but most importantly, I'd like to give my biggest thanks to my family: my husband Zhenyue Luo, my parents and the one who guides me. They are always there for me. No matter what I can always keep smiling, forget behind and reach forward, because love never fails.

TABLE OF CONTENTS

LIST OF FIGURES x

LIST OF TABLES xv

LIST OF ABBREVIATIONS xvi

CHAPTER 1 INTRODUCTION TO SPACE DIVISION MULTIPLEXING 1

1.1 Limit of Single-Mode Transmission 1

1.2 Space Division Multiplexed Transmission 3

1.2.1 Core Multiplexing using Multi-Core Fibers 3

1.2.2 Mode Division Multiplexing using Few-Mode Fibers 4

1.3 Dissertation Outline 8

CHAPTER 2 FEW-MODE MULTI-CORE FIBERS FOR SDM TRANSMISSION 10

2.1 Introduction 10

2.2 Fiber Design and Fabrication 11

2.2.1 Fiber Design 11

2.2.2 Fiber Fabrication 13

2.3 Fiber Characterization 15

2.4 Initial Transmission Experiment 19

2.5 Collaborated 200Tb/s Transmission Experiment 20

CHAPTER 3 COUPLED MULTI-CORE FIBERS FOR SDM TRANSMISSION 23

3.1 Introduction 23

3.2 Supermodes in Coupled Single-Mode Core Fibers 25

3.2.1 Coupled-Mode Theory for Supermodes 25
3.2.2 Design for Short-Distance Applications 29
3.2.3 Design for long-distance applications 32
3.3 Higher-Order Supermodes in Coupled Few-Mode Core Fibers 37
3.3.1 Higher-Order Supermodes in a Two-Core Structure 39
3.3.2 Higher-Order Supermodes in Linear-Array Structures 43
3.3.3 Higher-Order Supermodes in 2D Rectangular-Array Structures 46
3.3.4 Higher-Order Supermodes in Ring-Array Structures 49
3.3.5 Observation of Higher-Order Supermodes 53
CHAPTER 4 FEW-MODE PASSIVE OPTICAL NETWORKS 2
4.1 Introduction and Background 2
4.2 Principle of Few-Mode PON 3
4.3 Low-Crosstalk Few-Mode PON 5
4.4 Demonstration of the First Few-Mode GPON System 8
4.5 Alternatives and Discussion 10
4.6 Scaling to 5-mode PON 12
CHAPTER 5 SUMMARY 18
APPENDIX: DERIVATIONS 20
LIST OF REFERENCES 23

LIST OF FIGURES

Figure 1-1. Cross-sectional view of a fabricated trench-assisted multi-core fiber and its index profile 4

Figure 1-2. Schematic of a step-index circular fiber with an increasing cross-sectional area and profiles of supported modes along the fiber. 5

Figure 1-3. Schematic of (a) an ideal two-mode fiber in which the two parallel line represent two orthogonal modes and (b) a real fiber that has distributed cross talk. 7

Figure 2-1. Inter-core LP_{11} mode crosstalk between two adjacent cores of a hole-assisted few-mode MCF as a function of the air hole-to-pitch ratio d/Λ as well as that of a trench-assisted few-mode MCF at λ=1550nm. 13

Figure 2-2. Cross section of the fabricated FMMCF 14

Figure 2-3. The schematic setup for LP11 crosstalk measurement 16

Figure 2-4. Simulated LP_{11} free-space excitation-induced crosstalk value as a function of the propagation distance from phase plate to the FMMCF as well as the intensity pattern at FMMCF facet 18

Figure 2-5. (a) The setup for LP01 and LP11 transmission over 1km FMMCF (b) Q2 factor v.s. OSNR for back-to-back, LP01 and LP11 transmission. 20

Figure 2-6. FMMCF PDM/WDM/SDM transmission experimental setup. (a) the entire experimental setup; (b) the decorrelated wavelength spectrum after being interleaved by a wavelength selective switch; (c) 3D waveguide facet; (d) FM-MCF facet which butt-coupled to the 3D waveguide; (e) saturated camera image taken at the FM-MCF receiver side. 22

Figure 3-1. Schematic of a coupled four-core fiber structure. 25

Figure 3-2. Field distributions of the 1st (a), 2nd (b), 3rd (c) and 4th (d) supermodes for four-core CMCFs. (Black lines indicate the boundaries of the cores)..... 28

Figure 3-3. Field distributions of the 1st (a), 2nd (b), 3rd (c), 4th (d), 5th (e) and 6th (f) supermodes for the six-core CMCF. (Black lines indicate the boundaries of the cores)..... 31

Figure 3-4. A_{eff} vs. ΔN_{eff} for CMCFs and FMFs (ΔN_{eff} refers to the minimum ΔN_{eff} for one mode to any other mode); (b) Confinement factor vs. ΔN_{eff} for CMCFs and FMFs. 32

Figure 3-5. (a) (b) (c) $\frac{dc}{d\omega}$ at V=1.6, 1.7 and 1.9. (d) $\frac{d}{d\lambda}\left(\frac{dc}{d\omega}\right)$ at V=1.7..... 34

Figure 3-6. (a) maximum DMGD vs. wavelength at V=1.707 @1.55μm and Δ=0.06%, (b) (c) (d) field distribution of the 1st, 2nd and 3rd supermode of a three-core CMCF..... 36

Figure 3-7. Coupling between two arbitrarily oriented LP_{11} degenerate modes as a function of their initial angles φ_1 and φ_2 . The arrow points to the position of zero coupling $\kappa(\varphi_1 = 0, \varphi_2 = \pi/2) = 0$ between the LP_{11x} and LP_{11y} modes; the inset shows the coordinate system of the two cores including reference axes and two initial angles. 40

Figure 3-8. Modal fields of LP_{01} supermodes (a & b) and LP_{11} supermodes (c-f) of a basic two-core structure. In-phase supermodes are shown in (a), (c) and (d) while out-of phase supermodes are shown in (b), (e) and (f). 43

Figure 3-9. Modal fields of LP_{01} supermodes (a-d) and LP_{11} supermodes (e-l) of a 4-core linear-array structure. 45

Figure 3-10. (a) A rectangular array of waveguides. The LP_{01} mode in each waveguide cross-talks with nearest neighbors along the horizontal and vertical directions as well as with diagonal

elements. (b) Coupling interactions in this same array when each element involves instead the LP_{11} mode. 47

Figure 3-11. (a) Scheme of mode basis selection for LP_{11} supermode analysis of a 4-core grid-array structure; modal fields of LP_{01} supermodes (a-d) and LP_{11} supermodes (e-l) of a 4-core grid-array structure computed using COMSOL 48

Figure 3-12. (a) Scheme of mode basis selection for LP_{11} supermode analysis of a 3-core ring-array structure; modal fields of LP_{01} supermodes (b-d) and LP_{11} supermodes (e-j) of a 3-core ring-array structure computed using COMSOL. 53

Figure 3-13. (a) Schematic of S^2 imaging setup using a tunable laser and a CCD camera; (b) wavelength-scanning results of the multi-path interference pattern for one pixel of the CCD camera and (c) the result of intensity vs. differential group delay (DGD) after taking Fourier transform of (b). Inset of (c) shows the resolved LP modes after picking the information for every pixel at the corresponding DGDs of different modes and mapping them together. 56

Figure 3-14. (a) Cross-sectional view of the fabricated coupled-3-core fiber and (b-j) resolved supermodes of the fabricated coupled-3-core fiber shown in amplitude (x1) and phase (x2): (b) the fundamental LP_{01} supermode; (c, d) the degenerate pair of LP_{01} supermodes; (d) the fundamental LP_{11} supermode; (e, f) the first degenerate pair of LP_{11} supermodes; (g) the fourth LP_{11} supermode; (h, i) the second degenerate pair of LP_{11} supermodes. 1

Figure 4-1. PON architectures with low upstream loss using (a) multiple feeder fibers and a multimode combiner (MC); and (b) a single FMF with a mode transforming coupler (MTC)..... 3

Figure 4-2. (a) The cross-section of the mode-selective lantern output; (b) measured LP01, LP11a & LP11b intensity patterns at the lantern near-field, far-field and the end of lantern-to-20km FMF. 5

Figure 4-3. (a) Picture of the few-mode segment of the ODN; (b) measured LP01, LP11a and LP11b impulse responses of the few-mode ODN segment. 7

Figure 4-4. Schematic of a few-mode GPON system using a 20km FMF and a mode-selective lantern for upstream transmission. OLT: commercial optical line terminal; ONUs: commercial optical network units. 9

Figure 4-5. (a) BER measurements of the few-mode ODN segment; (b) eye diagrams of the cases of B2B (with SSMF), 20km LP01, LP11a and LP11b transmission. 10

Figure 4-6. Simulation results of modal group delay for 10-mode fiber design of trench-assisted graded-index profile. Inset: the FMF index profile with parameters indicated. 12

Figure 4-7. (a) The cross-sectional view of the photonic lantern output. (b) Intensity patterns of 5 modes for the near-field and far-field output of the photonic lantern and after 20km propagation via the FMF at 1.3μm. 13

Figure 4-8. Index profile of the few-mode fiber. Inset: cross-sectional view. 14

Figure 4-9. Impulse measurements and (b) eye diagrams of the 5-mode optical link composed of the photonic lantern spliced with 20km FMF spool. 15

Figure 4-10. BER measurements of the 5-mode optical link 16

Figure 4-11. Schematic of 5-mode GPON system using the PL spliced to 20km FMF for upstream transmission with commercial Huawei OLT and ONUs. OLT: optical line terminal; ONU: optical networking unit; PL: photonic lantern. Red line represents 1490nm downstream

transport; blue line stands for 1310nm downstream transport; and gray line corresponds to: bidirectional transmission. 17

LIST OF TABLES

Table 2-1. Parameters of Fabricated FMMCF 14

Table 2-2. Simulated and Measured characteristics of Fabricated FMMCF 15

LIST OF ABBREVIATIONS

Aeff	Effective area
CMCF	Coupled Multi-Core Fiber
DEMUX	Demultiplexer
DMGD	Differential Modal Group Delay
DMGDS	Differential Modal Group Delay Slope
DSP	Digital Signal Processing
EDFA	Erbium-Doped Fiber Amplifier
FMF	Few-Mode Fiber
FMMCF	Few-Mode Multi-Core Fiber
GI	Graded Index
GPON	Gigabit-capable Passive Optical Network
MC	Multimode Combiner
MCF	Multi-Core Fiber
MDL	Mode-Dependent Loss
MDM	Mode Division Multiplexing
MIMO	Multiple-Input-Multiple-Output
MMF	Multi-Mode Fiber
MTC	Mode Transforming Coupler
MUX	Multiplexer
Neff	Effective index
ODN	Optical Distribution Network

OLT	Optical Line Terminal
ONU	Optical Network Unit
PL	Photonic Lantern
PON	Passive Optical Network
QAM	Quadrature Amplitude Modulation
SDM	Space Division Multiplexing
SFP	Small Form-factor Pluggable transceiver
SMF	Single-Mode Fiber
SNR	Signal-to-Noise Ratio
TDM	Time Division Multiplexed
WDM	Wavelength Division Multiplexing
XT	Crosstalk

CHAPTER 1 INTRODUCTION TO SPACE DIVISION MULTIPLEXING

1.1 Limit of Single-Mode Transmission

Optical fiber communication is the backbone for the telecommunications infrastructure that supports the internet. Fueled by emerging bandwidth-hungry applications and the increase in computer processing power that follows the Moore's Law, the internet traffic has sustained an exponential growth in the past and this trend is expected to continue for the foreseeable future. It is well known that the capacity of a communication channel cannot exceed the Shannon limit, In the past two decades, the internet traffic demand was mainly met by the wavelength-division multiplexing (WDM) technology [1], which can increase the spectral bandwidth of the fiber-optic communication channel by two orders of magnitude. It should be noted that the spectral bandwidth of the fiber-optic communication channel can be further increased by exploiting the low-loss transmission window of the optical fiber beyond the C and L bands. However, this bandwidth expansion is limited to below one order of magnitude. Furthermore, lack of an integrated amplification platform makes such a system unattractive from a technical and economic perspective.

Recently, coherent detection has attracted much attention to provide capacity increase for optical fiber communication systems [2]. Coherent detection can maximize the signal-to-noise ratio (SNR) of the fiber-optic communication channel in comparison with direct detection. High SNR enables high-spectral efficiency quadrature amplitude modulation (QAM) that transmits

information in both the amplitude and phase of the optical signal. Digital coherent fiber-optic communication systems have recently become commercially available. Further increase in SNR can only be achieved by increasing the signal power. However, the increase in channel capacity scales logarithmically with the increase in signal power. This logarithmical channel capacity scaling ultimately cannot meet the demand of exponential traffic growth from a technical perspective as well as the perspective of power consumption per bit. In addition, fiber nonlinearity imposes an upper limit on how much power that can be transmitted in a fiber. Digital coherent optical communication does make polarization multiplexing practical, providing a factor of two increase in channel capacity.

While it might be impossible to provide exponential growth in optical fiber communication capacity to match the exponential growth in capacity demand, multiplicative growth in optical communication capacity, for example using WDM, has satisfied traffic demand in the past. As today's WDM coherent optical communication has already taken advantage of all degrees of freedom of a lightwave in a single-mode fiber (SMF), namely frequency, polarization, amplitude, and phase, further multiplicative growth has to explore new degrees of freedom that do not exist in single-mode fibers. Similar to the multiple-input-multiple-output (MIMO) architecture in wireless communication, space is the degree of freedom that is being considered for optical fiber communication beyond WDM. Space-division multiplexing, including mode-division multiplexing (MDM) using multimode fibers or few-mode fibers (FMF) [3-31] and/or core multiplexing using multi-core fibers (MCF) [32-71], has attracted much attention in the last three to five years for the next multiplicative capacity growth for optical communication [72-76].

1.2 Space Division Multiplexed Transmission

In optical fiber transmission, two SDM schemes have been proposed. These are (i) core multiplexing using multicore fibers (MCF), where a single strand of glass fiber contains a number of independent single- (or multi-) mode cores each capable of communicating optical signals; and (ii) mode division multiplexing (MDM) using multimode fibers (MMF) or few-mode fibers (FMF), where a single strand of fiber has one core with sufficiently large cross-section area to support a number of independent guiding modes.

1.2.1 Core Multiplexing using Multi-Core Fibers

Mode coupling, or called mode crosstalk is a major and fundamental obstacle for SDM transmission, which is unavoidable after long-distance propagation within imperfect fibers. One important reason that makes MCF a strong candidate for high capacity SDM transmission is that mode crosstalk is maintained low enough within MCFs, not to cause any noticeable signal penalty even after hundreds, or thousands of kilometers transmission. MCF has been used in fiber lasers for a long time. But only in the latest years, MCF has been introduced to optical transmission due to high spatial density with low loss and low crosstalk [77-79]. For each single core of MCFs, single mode condition is still applied. The crosstalk level is determined by the core-to-core distance, the core index and radius, as well as the cladding index profile. The core density is dominated by the core-to-core distance (or called pitch). However, the maximum cladding diameter is restricted by mechanical properties of silica, causing that the number of core

within an MCF is limited to about 20 [80, 81]. To further reduce crosstalk, a lower-index inner-cladding or a trench assisted inner cladding is generally needed shown in Fig. 1-1[81-84].

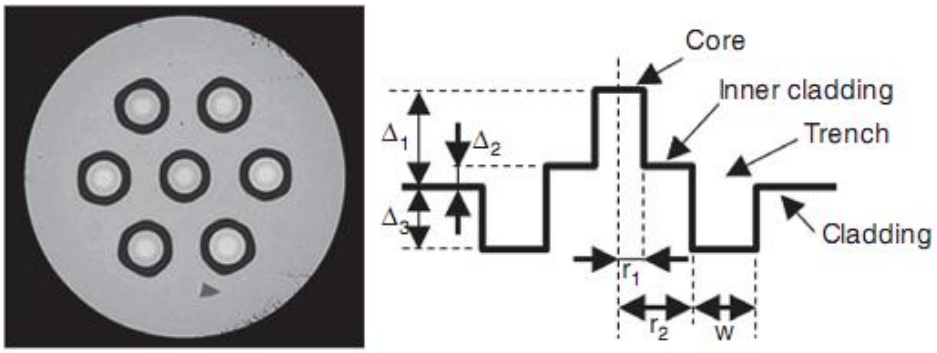

Figure 1-1. Cross-sectional view of a fabricated trench-assisted multi-core fiber and its index profile

Core multiplexing using MCFs is generally easy to implement as mode crosstalk is too low to be addressed. But it requires all the components to maintain a low crosstalk level at the same time, including (de)multiplexers and amplifiers. So far the highest capacity (1.01Pb/s) of core-multiplexed transmission is demonstrated by H. Takara [85] in a 52 km single span of 12-core MCF. In the other experiment by K. Igarashi et.al.[37], the reach is extended to 7326 km and net total capacity is 140.7Tb/s leading to a record capacity-distance product of 1030.8 Pb/s×km.

1.2.2 Mode Division Multiplexing using Few-Mode Fibers

A few-mode fiber is similar to a multi-mode fiber but with reduced number of modes so that each mode can be handled with care. The fiber mode concept is elaborated in the following as preliminary knowledge for the discussion afterwards.

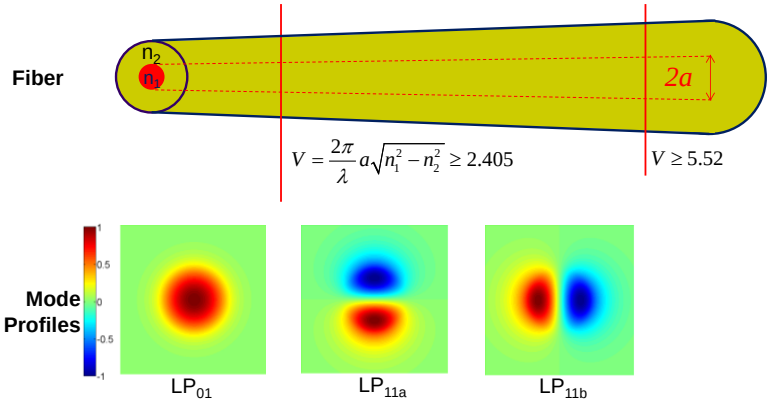

Figure 1-2. Schematic of a step-index circular fiber with an increasing cross-sectional area and profiles of supported modes along the fiber.

In MDM, we explore other modes other than the fundamental mode that can be supported in optical fibers. Figure 1-2 schematically illustrates a step-index circular fiber with an increasing cross-sectional area. This fiber will always support the fundamental mode, the LP_{01} mode, characterized by its propagation constant β_{01} and the normalized mode profile $\psi_{01}(r,\theta)$ such that the power contained in the mode $A_{01}\psi_{01}(r,\theta)\exp\{-i[\omega t-\beta_{01}z]\}$ is $|A_{01}|^2$. When the fiber diameter is increase to a point where the V number, $V=(2\pi/\lambda)a\sqrt{n_1^2-n_2^2}$, of the fiber is greater than 2.405, the fiber can guide light in the next higher order mode, the LP_{11} mode, characterized by its propagation constant β_{11} and the normalized mode profile $\psi_{11}(r,\theta)$. The LP_{11} mode has a two-fold degeneracy, rotated by 90^0 illustrated in Fig. 1-2. Fibers guide light using a high-index core and low-index cladding, which can be intuitively understood as by means of total internal reflection at the core-cladding boundary. In step-index fiber, the refractive index n_1 is uniformly distributed across the core surrounded by a cladding with refractive index

n_2. The propagation constant β of any guide mode is thus bounded by $(n_1 k_0, n_2 k_0)$ where k_0 is the propagation constant of light in vacuum. In typical fiber used for optical communication, the relative index difference defined by $\Delta = (n_1 - n_2)/n_1$ is less than 10^{-2}, therefore, fiber modes are weakly guided. Under the weakly-guided approximation, the vectorial modes of the fiber can be simplified using linearly polarization (LP) modes whose transverse field in the core is of the form

$$E_y(r,\theta) = E_y(a)\frac{J_p(k_r a)}{J_p(k_r r)}\cos(p\theta) \qquad (1\text{-}1)$$

where a is the radius of the core, $k_r = \left(k^2 n_1^2 - \beta^2\right)^{1/2}$ and p is a non-negative integer referred to as the azimuthal mode number. For the same p value, k_r can take on discrete values, labeled by a non-negative integer q corresponding to the number of zero crossings of the field along radial direction. The LP modes can be labeled as LP_{pq}, each having two-fold degeneracies in polarizations in x and y, and for $p \neq 0$ two fold degeneracies in spatial orientations separated by a rotation of π / p. The total number of modes of the step index core fiber is approximately [86]

$$M \approx \frac{1}{2}V^2.$$

By definition, modes supported by the fiberare orthonormal, i.e.,

$$\iint \psi_{rs} \cdot \psi_{pq}^{*} r dr d\theta = \delta_{pr}\delta_{qs} \qquad (1\text{-}2)$$

which is the basis for mode-division multiplexing: transmitting and receiving independent information simultaneously in each fiber mode.

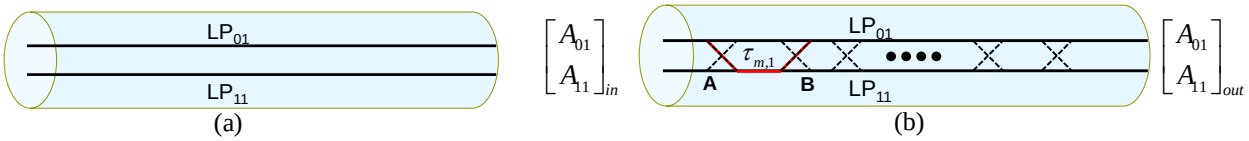

Figure 1-3. Schematic of (a) an ideal two-mode fiber in which the two parallel line represent two orthogonal modes and (b) a real fiber that has distributed cross talk.

The concept of MDM has been around for a very long time [87] but has not been pursued until recently. The reason is that the orthogonality of modes can only be maintained in practical application for a very short distance because of crosstalk among modes due to fiber imperfections, bending and twisting as shown in Fig. 1-3. Here we discuss the origin of the mode coupling first before going to the solutions and applications. Within the degenerate mode group having the same propagation constant, the modes couple to each other when the index distribution of the fiber deviates from the ideal circular-symmetric distribution. For the non-degenerate modes, mode coupling is introduced due to fiber longitudinal variations. Such a variation can be caused by fiber manufacturing process as well as micro- and macro-bending of the fiber. Therefore the coupling is random in both strength and location and thus has to be dealt statistically. Furthermore, because the non-degenerate modes propagate at different velocities, the signal sent into the modes would accumulate a differential modal group delay (DMGD) eventually at the end of fiber as well as the mode coupling, which is a major obstacle for MDM transmission. There are several ways to address the problem. One solution widely used for long-distance high capacity transmission is to adopt MIMO digital signal processing (DSP) to compensate the penalty caused by mode coupling as well as the DMGD, similar to the MIMO technique used in wireless communication. Basically, the compensation is to invert the coupling matrix in the electronic domain since coherent detection is able to get both intensity and phase

information of the signal. But the algorithm complexity and required memory length is always a big concern even though a lot of good efforts have been put in [28, 88-90]. Another way to deal with the mode coupling is to transmit the same data in the mode group where the DMGD within the group is reduced to be much less than the symbol period so that the mode coupling itself would no longer be a problem. The DMGD can be minimized by careful fiber design [91, 92] or compensated by optical fiber with the opposite sign of DMGD [93, 94], both of which has been investigated intensively. Besides, the mode coupling also can be decreased by careful fiber design, for example increasing the propagation constant difference of the modes so that small perturbations would have less impact. Other than the mode coupling problem, MDM transmission also requires high performance (de)multiplexer [95-97], efficient amplification [98, 99], mature splice technique etc [100]. All of them need to be taken care of to give a final integrated high capacity transmission.

1.3 Dissertation Outline

The outline of the proposal report is laid out as follows:

In Chapter 1, Introduction presents the motivation, background and organization of the dissertation.

In the chapter 2, the motivation using FMMCF for high capacity SDM system is explained after a brief introduction of the current dilemma using few-mode fibers (FMFs) and multi-core fibers (MCFs) separately. By applying hole-assisted structure and careful fiber design,

we show that both high mode density and low crosstalk can be achieved in a FMMCF, which is then fabricated, tested and applied for 1km transmission enabling petabits capacity.

Chapter 3 shows our study of using CMCFs as another candidate for high capacity SDM, where mode coupling (sometimes called crosstalk) is taken advantaged instead of being avoided. First, we demonstrate that optical properties can be engineered by proper design of coupled single-mode core structure. We then move on to study the higher-order supermodes in CMCFs with few-mode cores, which can be predicted by the coupled-mode theory with angle-dependent couplings. Analytical description for higher-order supermodes in different array configurations are provided, including linear, square and ring array lattices. We also present an experimental observation of higher-order supermodes in a coupled 3-core fiber.

Chapter 4 focuses on applying SDM in commercial access transmission. In this chapter, we proposed the use of space-division multiplexing (SDM) in a single few-mode fiber (FMF), acting as the feeder fiber in the optical distribution network (ODN), to effectively eliminate the upstream combining loss. Moreover, this concept has been realized by using a commercial GPON system carrying live Ethernet traffic, achieving the first reported few-mode GPON. The principle and alternative schemes are discussed as well as a horizon for future works. In addition, a 5-mode PON experiment is discussed with a record net gain of 4dB as an important extended work.

Chapter 5 is dedicated to summarize the above works.

CHAPTER 2 FEW-MODE MULTI-CORE FIBERS FOR SDM TRANSMISSION

2.1 Introduction

Multi-core fibers (MCF) and few-mode fibers (FMF) are transmission fiber candidates for space-division multiplexing (SDM) [59, 88]. MCFs with lower crosstalk and long-distance transmission in such MCFs have been reported [59, 101]. Transmission in FMFs using up to 5 spatial modes including amplified transmission has also been demonstrated [8]. One of the main goals of SDM is to provide orders of magnitude increase in transmission capacity by increasing the number of space channels. For MCFs demonstrated so far, each core supports only the fundamental mode. The number of cores is limited by the desired low crosstalk at sufficiently large core pitch and the maximum fiber cladding diameter (~225microns) from mechanical considerations. The largest number of cores demonstrated for a MCF so far is 19 [66]. Although it is not difficult to increase the number of spatial modes for FMFs, there are some disadvantages associated with FMF with a large number of spatial modes. First, the confinement factor and consequently the bending loss of the higher-order modes will be larger than the lower-order modes. Second, multiplexing and demultiplexing of a large number of modes are complicated and generally introduce more losses. In order to achieve higher capacity for future SDM, the number of spatial channels per fiber needs to be further increased from MCFs and FMFs demonstrated so far. Therefore, the authors have designed and fabricated a few-mode MCF (FMMCF) [102-104], in which each core supports both the linearly-polarized (LP) LP01 mode and the two fold-degenerate LP11 modes.

2.2 Fiber Design and Fabrication

2.2.1 Fiber Design

The few-mode MCF was primarily designed to demonstrate both high mode density and ultra-low crosstalk. Theoretically, the crosstalk of a few-mode MCF includes inter-core crosstalk $XT_{LP_{01}}$ and $XT_{LP_{11}}$ for LP01 and LP11, and intra-core crosstalk between LP01 and LP11. It is known that an effective index difference (ΔNeff) larger than 10^{-3} would significantly reduce intra-core crosstalk between the two modes. For inter-core crosstalk, LP11-crosstalk is generally more severe than LP01-crosstalk because the LP11 mode is less confined. Therefore the main design goal is to achieve sufficiently low $XT_{LP_{11}}$. It has been demonstrated [101] that the inter-core crosstalk is statistical, obeying the chi-square distribution with mean crosstalk given by

$$XT = 2\frac{\kappa^2}{\beta}\cdot\frac{R}{D}\cdot L \qquad (2\text{-}1)$$

where κ, β, R, D are the coupling coefficient, propagation constant, bend radius and core pitch, respectively. A large core-to-core distance is a straightforward way to reduce inter-core crosstalk but it would decrease the mode density. Therefore, other than keeping a large core-to-core distance, we applied two approaches to reduce $XT_{LP_{11}}$. First, a hole-assisted structure proposed by [105] has been added outside of each core to improve the mode confinement and hence reduce inter-core crosstalk. This structure has large control flexibility as both the air-hole diameter d and the air-hole pitch Λ can be tuned. A simulation has been conducted shown in Fig. 2-1 to compare the $XT_{LP_{11}}$ performance between two adjacent cores of this hole-assisted structure

and a trench-assisted structure at λ=1550nm [101]. Notice that the center core and outer core would experience 7.8dB and 4.8dB higher crosstalk than that shown in Fig. 2-1 when seven cores are simultaneously excited. The coupling coefficient κ of the LP11 mode between two adjacent cores was obtained by calculating the LP11 mode profile for this fiber structure using a full-vector finite-element method and substituting it into the following formula [106]

$$\kappa_{12,LP_{11}} = \frac{\omega\varepsilon_0 \int_{-\infty}^{+\infty}\int_{-\infty}^{+\infty} (N^2 - N_2^2)\vec{E}^*_{1,LP_{11}}\vec{E}_{2,LP_{11}}dxdy}{\int_{-\infty}^{+\infty}\int_{-\infty}^{+\infty} \vec{u}_z(\vec{E}^*_{1,LP_{11}} \times \vec{H}_{2,LP_{11}} + \vec{E}_{1,LP_{11}} \times \vec{H}^*_{2,LP_{11}})dxdy}, \quad (2\text{-}2)$$

where N, N2 are the refractive index distributions of the entire structure and the second waveguide, respectively, $\vec{u}_z$ is the unit vector in z direction. For fair comparison, a typical trench-assisted single-mode multi-core fiber in ref. [101] is linearly scaled to a trench-assisted few-mode multi-core fiber, which has the same core radius of 6.55μm, core index difference 0.36% and core pitch 40μm as the hole-assisted FMMCF in the simulation. The trench index difference, inner cladding radius and the trench width of the scaled trench-assisted FMMCF are -0.55%, 9.8μm and 9.5μm respectively. The air-hole pitch of the hole-assisted FMMCF is 13.3μm. It can be seen in the simulation that as the air hole-to-pitch ratio d/Λ increases to above 0.7, or equivalently the air-hole diameter to above 9.3μm, the hole-assisted FMMCF starts to outperform the trench-assisted one in terms of low $XT_{LP_{11}}$. Secondly, a large V-number close to LP21 / LP02 cut-off condition is selected to better confine LP11 mode and reduce inter-core crosstalk without introducing any higher-order modes. With the above design, this novel FMMCF achieves a mode density 8 times larger than a standard single mode fiber (SSMF).

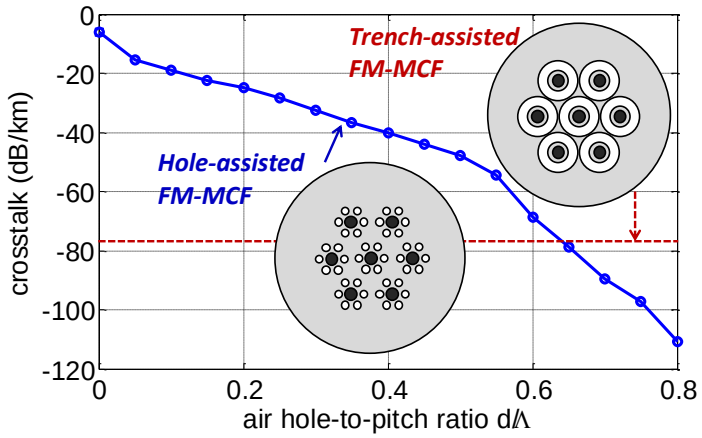

Figure 2-1. Inter-core LP_{11} mode crosstalk between two adjacent cores of a hole-assisted few-mode MCF as a function of the air hole-to-pitch ratio d/Λ as well as that of a trench-assisted few-mode MCF at λ=1550nm.

2.2.2 Fiber Fabrication

A 1 km fiber was successfully fabricated using the stack-and-draw method. Its cross section and geometry parameters are shown in Fig. 2-2 and Table 2-1. Because homogeneous MCFs have shown to exhibit lower crosstalk than heterogeneous MCFs with bend-induced coupling, this fiber design is intended to be homogeneous in spite of a slight fabrication size variation from core to core. It should be pointed out that although the fabricated fiber cladding diameter is relatively large, it could be reduced to around 150μm without affecting its transmission properties.

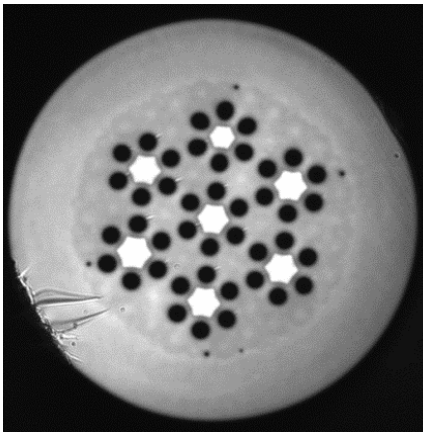

Figure 2-2. Cross section of the fabricated FMMCF

Table 2-1. Parameters of Fabricated FMMCF

Parameters	Value
Core index difference	0.36%
Core diameter	13.1μm
Core pitch	40μm
Air-hole diameter	8.2μm
Air-hole pitch	13.3μm
Air hole-to-pitch ratio	0.62
Cladding diameter	192μm
Coating diameter	375μm

According to the geometric parameters in Table I, the theoretical properties of the MFMCF are listed in Table 2.II. An effective index difference ΔNeff more than 2×10^{-3} is provided between LP01 and LP11, as well as LP11 and cladding to suppress macro-bending loss. The transmission loss of all modes within 1km is negligible. The differential modal group delay (DMGD) is measured to be 4.6ps/m using an interferometric method.

Table 2-2. Simulated and Measured characteristics of Fabricated FMMCF

Fiber characteristics	LP01	LP11
Measured mode field diameter (MFD) [μm]	11.8	/
Simulated effective area (Aeff) [μm2]	113	170
Simulated cut-off wavelengtha (λc) [nm]	/	~2100a
Simulated chromatic dispersion [ps/nm/km]	23	28
Simulated dispersion slope [ps/nm2/km]	0.06	0.07
Simulated effective index difference (ΔNeff)	2.4×10-3	
Measured differential modal group delay (DMGD) [ps/m]	4.6	
Simulated Inter-core crosstalkb [dB/km]	-100	-70

[a]The simulated cut-off wavelength for LP21/LP02 modes is ~1300nm.
[b]Inter-core crosstalk is between two adjacent cores.

2.3 Fiber Characterization

The 1km FMMCF is winded on a fiber drum with a mandrel radius of 15.9cm. The LP01 and LP11 inter-core crosstalk are obtained at λ=1550nm. Given a large effective index difference between LP01 and LP11, intra-core crosstalk is assumed to be very small. This is also confirmed by an offset-launch impulse response measurement which, after 1 km propagation, only displays two pulses corresponding to the LP01 and LP11 modes, respectively.

The LP01 crosstalk measurement is achieved by using a SSMF butt coupled to the FMMCF for both excitation and reception. This method ensures that no LP11 is received even with unintentional offset excitation or intra-core mode coupling. The average measured value of $XT_{LP_{01}}$ is -60dB, which was limited by the dynamic range of our measurement capability.

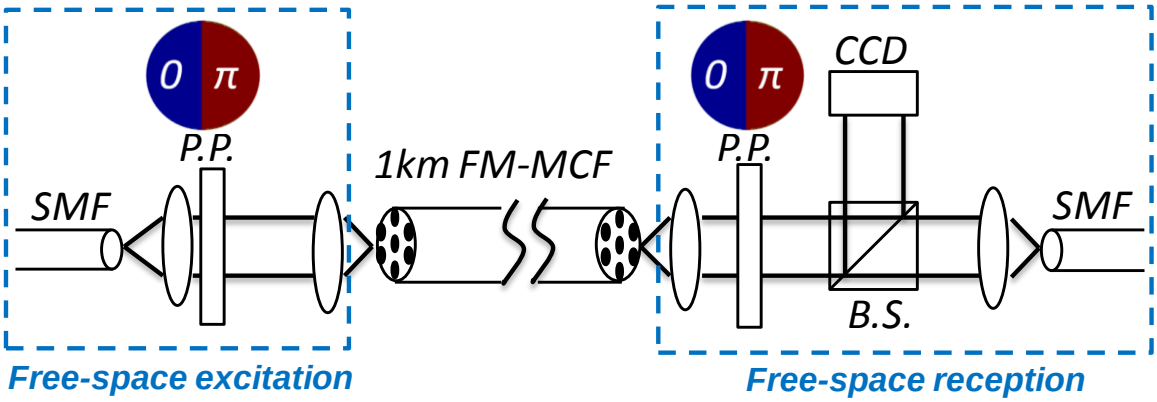

Figure 2-3. The schematic setup for LP11 crosstalk measurement

In order to measure LP11 crosstalk, both excitation and reception were conducted in free-space using phase plates shown in Fig. 2-3. For excitation, light was launched from a SMF into free space and through a phase plate, which has a π phase difference between two semicircles and hence filters out most of the LP01 mode. The extinction ratio of the phase plate is estimated to be about 20dB at 1550nm. For reception, another phase plate was used to convert LP11 mode into LP01 so that it can be captured by the receiving SMF and at the same time reject residual LP01 mode in the FMMCF if there is any. The free-space excitation at the input FMMCF facet is not a perfect LP11 field and thus introduces a discrete crosstalk, which is named excitation-induced crosstalk in this letter. This imperfection is caused by lack of intensity modulation, the simple structure of the phase plate and free-space propagation. To simulate this effect, the real field at the input FMMCF facet is calculated by using the following equation:

$$E_o(x_o, y_o) = FT\{A_2(x_2, y_2) \cdot Fresnel\{P(x_1, y_1) \cdot A_1(x_1, y_1) \cdot FT\{E_i(x_i, y_i)\}\}\} \qquad (2\text{-}3)$$

where $E_i(x_i, y_i)$ represents the field of the fundamental mode output from an SMF, $A_1(x_1, y_1)$ and $A_2(x_2, y_2)$ denote the aperture functions of the first and second 20x microscope objective lens,

respectively, $P(x_1, y_1)$ refers to the phase structure of the phase plate, the symbol FT and $Fresnel$ represent Fourier transform and Fresnel diffraction operation. The inset in Fig. 2-4 shows the calculated intensity pattern at the input FMMCF facet, which contains two tails instead of a clean LP11 mode. The excitation-induced crosstalk value varies with the angle with respect to the axis of the phase plate. The excitation is maximum (minimum) for a neighboring core that is placed perpendicular (parallel) to the line dividing the two phases on the phase plate. The maximum excitation-induced crosstalk can be obtained by evaluating the overlap integral between the field at the FMMCF input facet and LP01 and LP11 mode profiles of the FMMCF. Figure 2-4 shows that the induced crosstalk also depends on the propagation distance from the phase plate to the FMMCF. Experimental results agree with this trend when the distance between the phase plate and the input FMMCF facet is shorter than 0.5 m, when the crosstalk reaches a floor of about -40dB for 1km fiber. The reason might be the simulation does not take account of leaky LP21 / LP02 modes and cladding modes within the FMMCF. Initially, the measured $XT_{LP_{11}}$ only after a short piece of 2m fiber and of 1 km fiber were observed to be the same at around -40dB [103]. As a result, it was concluded that crosstalk floor was due to the measurement setup.

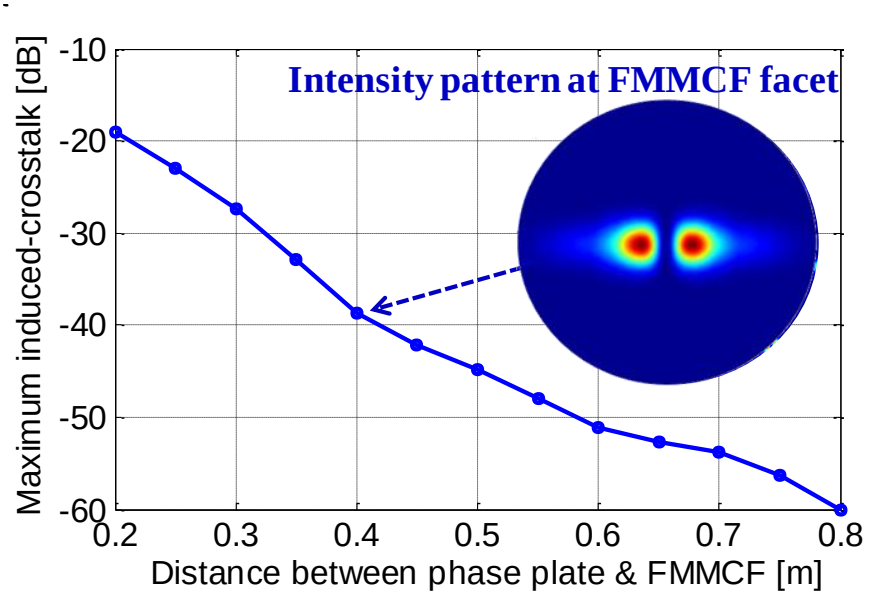

Figure 2-4. Simulated LP_{11} free-space excitation-induced crosstalk value as a function of the propagation distance from phase plate to the FMMCF as well as the intensity pattern at FMMCF facet

However, we have confirmed recently that the value of -40dB/km is the actual LP11 crosstalk due to the FMMCF itself. This is made possible by adding another step in the $XT_{LP_{11}}$ crosstalk measurement in which one turn of tight bend was introduced near the excitation end of the fiber. The mandrel diameter of the bend is 50mm. This small amount of tight bend effectively eliminates the leaky LP21 mode and cladding modes caused by imperfect excitation. The measured $XT_{LP_{11}}$ after 1km FMMCF with tight bend is still around -40dB while that after 2m fiber is less than -47dB. These results infer that the detected -40dB $XT_{LP_{11}}$ is from 1km of propagation along the fiber. The large discrepancy of $XT_{LP_{11}}$ between experimental measurement and simulation is under investigation. It could be contributed by fiber imperfections, such as the longitudinal variance along the fiber or the hexagonal core shape, which result from the fiber drawing process. Another possible reason is that the leaky LP21 / LP02 mode can act as an

intermediary and mediate $XT_{LP_{11}}$ through a considerable intra-core crosstalk with LP11 mode. For example, during propagation, a fraction of the launched LP11mode may couple into LP21 / LP02 mode within the same core, and then the LP21 / LP02 mode would leak into the modes of the other cores, including LP11 modes and be detected as $XT_{LP_{11}}$.

2.4 Initial Transmission Experiment

The 1km few-mode MCF has been tested in a single channel transmission experiment for both LP_{01} and LP_{11} respectively. The experimental setup is shown in Fig. 2-5(a) and the fiber was wound on a fiber drum whose mandrel radius is15.9cm. Light from an external cavity laser at 1550nm is modulated to produce a 10Gsym/s BPSK signal using a pattern generator. Then the signal is coupled into either the LP01 or LP11 mode of an arbitrary core of the 1km FMMCF. Each mode is excited and received in free space with objective lenses for better comparison. The insets in Fig. 2-5(a) show the LP01 and LP11 mode profiles at the transmitter and receiver. It is observed that both mode profiles are highly preserved through transmission over the 1 km FMMCF. When LP11 is transmitted, one phase plate is added at the input to excite an almost pure LP11 mode and another one is inserted at the output to convert the LP11 mode back to the LP01 mode. The received signal is then sent to a 90 degree hybrid followed by four photo detectors. The variable attenuator and the following amplifier before the hybrid are used for noise loading. The received waveforms were recorded using a real-time oscilloscope and analyzed offline. Fig. 2-5(b) shows the Q2-factors as a function of the optical signal-to-noise ratio (OSNR) for the LP01 and LP11 modes after transmission as well as for back-to-back

measurement. The transmission penalties for the LP01 and LP11 modes are less than 1dB and 2dB, compared to back-to-back, respectively. These penalties could be due to discrete mode coupling induced by the imperfect excitation. For example, LP11 free-space excitation using a phase plate cannot completely filter out the LP01 mode. The residual LP01 would transmit together with LP11 and produce a small amount of modal dispersion-induced penalty in the LP11 transmission experiment.

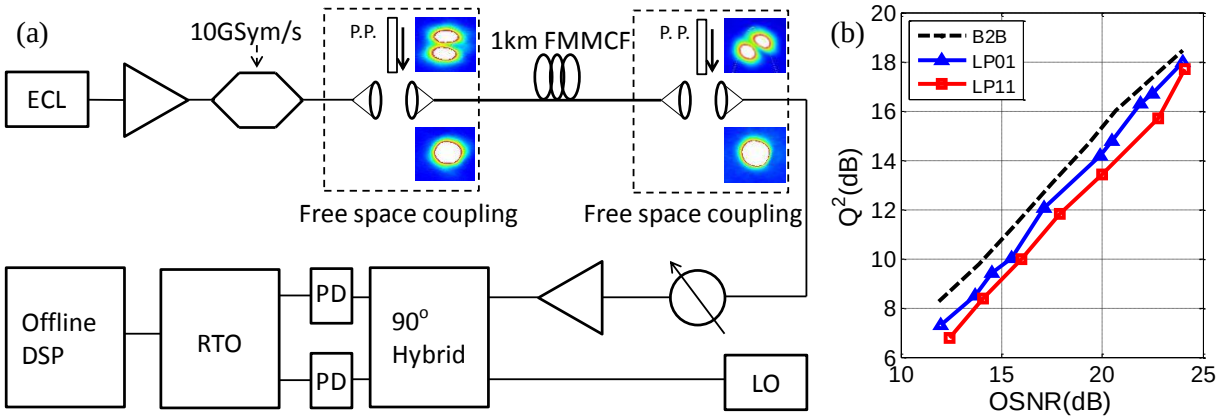

Figure 2-5. (a) The setup for LP01 and LP11 transmission over 1km FMMCF (b) Q2 factor v.s. OSNR for back-to-back, LP01 and LP11 transmission.

2.5 Collaborated 200Tb/s Transmission Experiment

A few-mode multi-core fiber consisting of 7 cores each supporting 3 spatial modes per polarization has been designed and fabricated. Low core-to-core crosstalk levels have been achieved for both LP01 and LP11 modes. Data transmission in LP01 / LP11 mode over 1km of FMMCF has been demonstrated. The fiber is able to support petabits transmission for next generation high capacity communication.

A robust transmission of 42 spatial channels has been achieved by using this novel hole-assisted FM-MCF as shown in Fig. 2-6 [107]. The signal is coupled into and out of the FMMCF employing custom designed low loss (<1.5dB) 3D waveguide (de)multiplexers, indicating the high integration potential into emerging core network transponders. Furthermore, low computational complexity MIMO digital signal processing was employed to enable an aggregate transmission capacity of 255 Tbit/s (200 Tbit/s net), consisting of 50 spatial super channels transmitting 5.103 Tbit/s per carrier (4 Tbit/s per carrier net) on a dense 50 GHz wavelength ITU grid with a spectral efficiency of 102 bits s-1 Hz-1 for fully mixed MIMO transmission per core. To the best of our knowledge, to date, this is a record for single-carrier transmission. Whilst readily enabling beyond next generation capacity per wavelength, the demonstrated transmission system has the potential to combine 21 legacy SMFs operating on an ITU standardized 50 GHz spaced wavelength grid into a single fibre. Considering the emerging amplifier multimode and multicore technologies, this work proves that a new class of fibres combining few-modes and multi-core paves the way to potential future long-haul transmission systems.

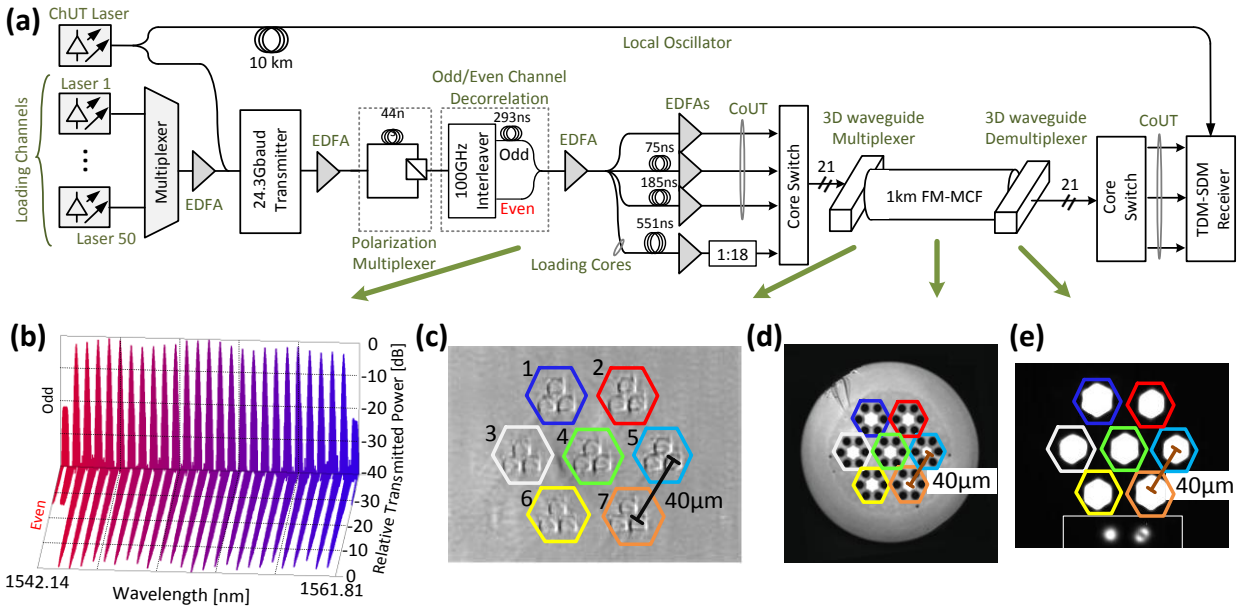

Figure 2-6. FMMCF PDM/WDM/SDM transmission experimental setup. (a) the entire experimental setup; (b) the decorrelated wavelength spectrum after being interleaved by a wavelength selective switch; (c) 3D waveguide facet; (d) FM-MCF facet which butt-coupled to the 3D waveguide; (e) saturated camera image taken at the FM-MCF receiver side.

CHAPTER 3 COUPLED MULTI-CORE FIBERS FOR SDM TRANSMISSION

3.1 Introduction

Supermodes are eigenmodes of composite structures involving coupled constituent elements, each of which also supporting guided modes in isolation [108, 109]. As indicated in a number of studies, such multi-core systems can be effectively analyzed using coupled-mode theory (CMT) - which is particularly effective when the coupling between neighboring elements is relatively weak. Over the years, the properties of supermodes in either linear [110] or ring arrays of coupled waveguides have been analyzed using CMT methods [111-113]. Even in the simplest possible configuration of two coupled channels, supermodes play an important role given that their interference is the one responsible for the energy exchange behavior in a directional coupler.

Quite recently, supermodes have received renewed interest within the context of mode-division multiplexing (MDM), a new transmission method aimed at overcoming the capacity limit of single-mode fiber communication systems. Since modes tend to couple during long-distance fiber transmission, unravelling mode crosstalk using multiple-input-multiple-output (MIMO) digital signal processing (DSP) is necessary for demultiplexing MDM channels [18]. In the presence of modal group dispersion, the computational load for MIMO DSP is proportional to the modal group delay [114, 115]. Interestingly, coupled multi-core fibers can be designed to have reduced modal group delays and/or larger effective areas in comparison with few-mode fibers (FMF) [116]. In a recent experiment, the modal delay was also found to depend

sublinearly on transmission distance in the presence of strong supermode coupling [117]. It is thus imperative to study the properties of optical supermodes in a systematic manner.

In this chapter, we introduce the coupled multi-core fiber (CMCF) structure with strong core-to-core coupling [118]. Coupling between cores can be manipulated to achieve better transmission properties for coupled modes. Field distribution of a coupled mode can be seen as a superposition of isolated modes, which is the reason why the coupled modes are also called supermodes. For this reason, supermodes generally have much larger effective area. Due to the unique properties of supermodes, CMCFs can support larger mode effective areas and higher mode densities than the conventional multi-core fiber. In addition, these CMCFs can also have lower modal dependent loss, mode coupling and differential modal group delay than the few-mode fiber. These advantages enable this new type of fiber as a potential candidate for applications of both spatial division multiplexing and single-mode operation.

The content is organized as follows. Section 3.2 focuses on the supermodes in CMCFs with single-mode cores. Section 3.2.1 introduces the basic properties of supermodes by analyzing a four-core CMCF structure using the coupled-mode theory. Section 3.2.3 demonstrates CMCF designs for short-distance SDM applications with the primary goal of achieving low crosstalk between the supermodes. Section 3.2.4 gives CMCF designs for the long-distance SDM applications where the DMGD has to minimized over the transmission band. In addition, supermode structures with multimode constituent elements were first introduced in [119].In section 3.3.1-4, we provide analytical description for higher-order supermodes in different array configurations, including linear, ring and square array lattices. Finally in section 3.3.5, we present an experimental observation of higher-order supermodes in a 3-core fiber array.

3.2 Supermodes in Coupled Single-Mode Core Fibers

3.2.1 Coupled-Mode Theory for Supermodes

In this section, we present the basic supermode analysis of CMCFs. A four-core CMCF structure, shown in Fig. 3-1, is selected as an example. Fiber cores are assumed to be identical and each of them supports only one mode. The radius of the cores is r, and the distances between adjacent cores and non-adjacent cores are d_1 and d_2, respectively. The cores and the cladding have refractive indices of n_1 and n_2, respectively. The mode of each isolated core has the same normalized frequency (V-number) $V = \frac{2\pi}{\lambda_0} r\sqrt{n_1^2 - n_2^2}$.

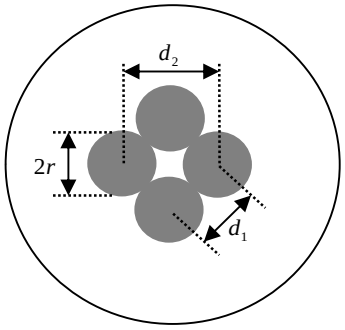

Figure 3-1. Schematic of a coupled four-core fiber structure.

According to the coupled-mode analysis [120], the interaction between the modes of the four individual cores can be described by the following coupled-mode equation

$$\frac{d}{dz}\boldsymbol{A} = -j\overline{\boldsymbol{M}}\boldsymbol{A}, \qquad (3\text{-}1)$$

where $\boldsymbol{A} = [A_1 \quad A_2 \quad A_3 \quad A_4]^T$, $\overline{\boldsymbol{M}} = \begin{pmatrix} \beta_0 & c_1 & c_2 & c_1 \\ c_1 & \beta_0 & c_1 & c_2 \\ c_2 & c_1 & \beta_0 & c_1 \\ c_1 & c_2 & c_1 & \beta_0 \end{pmatrix}$, A_i $(i = 1,2,3,4)$ refers to the complex amplitude of the electrical field of the ith core, β_0 is the propagation constant of the single mode, c_1 and c_2 are the coupling coefficients between adjacent and non-adjacent cores, respectively. Since $\overline{\boldsymbol{M}}$ is Hermitian for a lossless system, it can be diagonalized by a unitary matrix such that

$$\boldsymbol{Q}^{-1}\overline{\boldsymbol{M}}\boldsymbol{Q} = \boldsymbol{\Lambda}, \qquad (3\text{-}2)$$

where $\boldsymbol{\Lambda}$ is a diagonal matrix,

$$\boldsymbol{\Lambda} = \begin{pmatrix} \beta_1 & 0 & 0 & 0 \\ 0 & \beta_2 & 0 & 0 \\ 0 & 0 & \beta_3 & 0 \\ 0 & 0 & 0 & \beta_4 \end{pmatrix}, \qquad (3\text{-}3)$$

in which β_m $(m = 1,2,3,4)$ is the propagation constant of the mth supermode supported by the CMCF. The amplitude matrix for the supermodes is represented as

$$\boldsymbol{B} = \boldsymbol{Q}^{-1}\boldsymbol{A}, \qquad (3\text{-}4)$$

under which the coupled-mode equation (1) reduces to

$$\frac{d}{dz}\boldsymbol{B} = -j\boldsymbol{\Lambda}\boldsymbol{B}. \qquad (3\text{-}5)$$

Under the weakly guiding approximation, a general expression of the coupling coefficient c_j $(j = 1,2)$ is given as [121]

$$c_j = \sqrt{\frac{n_1^2 - n_2^2}{n_1^2}} \cdot \frac{1}{r} \cdot \frac{U^2}{V^3} \cdot \frac{K_0(Wd_j / r)}{K_1^2(W)}. \qquad (3\text{-}6)$$

Where U and W can be found by solving equation $U \cdot K_0(W) \cdot J_1(U) = W \cdot K_1(W) \cdot J_0(U)$ and $U^2 + W^2 = V^2$. The J's and the K's are Bessel functions of the first kind and modified Bessel functions of the second kind. After obtaining the coupling coefficients c_1 and c_2, the supermodes can be solved as eigen-modes. The propagation constant of the supermodes are the eigenvalues, given by:

$$\beta_1 = \beta_0 + 2c_1 + c_2; \beta_2 = \beta_0 - c_2; \beta_3 = \beta_0 - c_2; \beta_4 = \beta_0 - 2c_1 + c_2. \qquad (3\text{-}7)$$

The second and third supermodes are degenerate, having the same propagation constants. Using $n_1 = 1.47,\ n_2 = 1.468,\ r = 7\ \mu m,\ d = 14\ \mu m$ and $\lambda = 1.55\ \mu m$, the field distributions of each supermode is calculated and shown in Fig. 3-2.

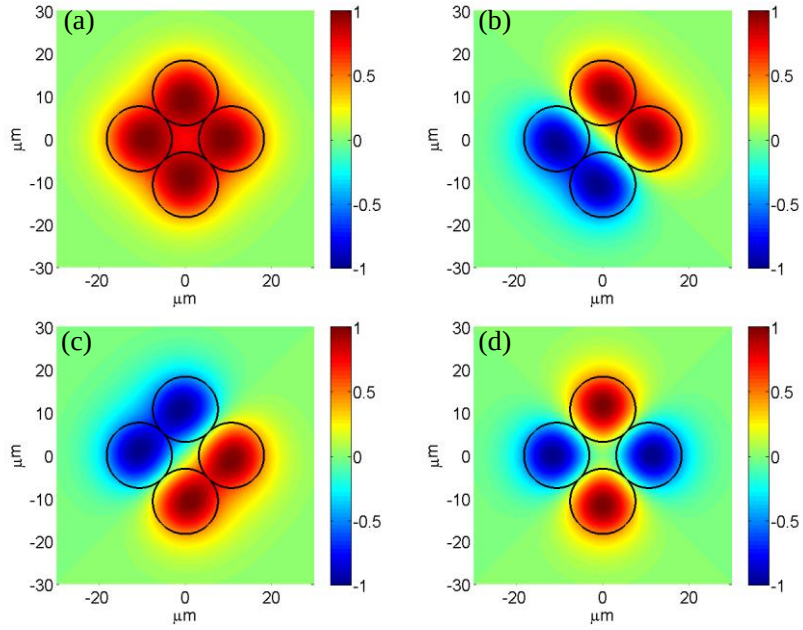

Figure 3-2. Field distributions of the 1st (a), 2nd (b), 3rd (c) and 4th (d) supermodes for four-core CMCFs. (Black lines indicate the boundaries of the cores)

One important characteristic of supermodes in four-core CMCFs is that they are superpositions of isolated modes with equal amplitude but not always the same phase. As shown in Fig. 3-2 (a), the fundamental supermode is the in-phase mode with the largest propagation constant. The higher-order supermodes have the field reversals between adjacent or non-adjacent core regions, shown in Fig. 3-2(b)-(d). This equal-amplitude characteristic gives similar confinement factors for the supermodes, leading to very small modal dependent loss. It is clear from this example that the properties of supermodes are determined not only by the parameters of each cores but the pitch between cores. In other words, CMCFs have more degrees of freedom or large design space than MCFs and FMFs.

For mode-division-multiplexing, two concepts can be simultaneously applied in CMCFs. One is to utilize zero DMGD between the two degenerate supermodes and the other is to

eliminate mode coupling between the non-degenerate supermodes. Demultiplexing can be realized by first detecting the non-degenerate ones separately and then recover signals mixed in the degenerate supermodes by MIMO DSP techniques. Compared to FMF modes, the supermodes can maintain less mode coupling, nonlinearity and similar loss. Considering the accumulated mode coupling level after long distance can be big, this scheme is best for short-distance applications which is discussed in the section 3.2.2. The other possibility is to design CMCFs with zero DMGD (or DMGD much less than the symbol period), between all the supermodes and a DMGD slope small enough for WDM system. This scheme can be applied to long-distance applications which we would talk in the section 3.2.3. In that section, a 60 ps/km DMGD between any two supermodes across the C-band has been demonstrated in a step-index three-core CMCF. This DMGD value can be further reduced by reducing the index difference between the core and cladding. It has been reported that graded-index profiles can decrease DMGD in FMFs [122]. It is likely that a more sophisticated index profile including the graded-index profile for CMCFs may further reduce the DMGD.

3.2.2 Design for Short-Distance Applications

It is expected that space-division-multiplexed (SDM) optical transmission can operate successfully either without mode coupling [21] or with mode coupling but with negligible or small differential modal group delay (DMGD) [18]. For the case that there is no mode coupling, modes propagate independently and therefore can be separately detected. For the case with mode coupling but small DMGD , modes may couple to each other, but they can be detected together

and then separated by using multiple-input-multiple-output (MIMO) based digital signal processing (DSP) technique [18]. These two methods can be combined in supermode multiplexing as will be explained below.

In this simulation, the number of mode is selected to be 6 again. However, the core arrangement is without a center core so higher-order supermodes and the fundamental supermode are more symmetrical. The field distributions of the supermodes are shown in Fig. 3-3. Again, both six-core CMCFs and six-mode fibers support six modes including two pair of degenerate modes and two other non-degenerate modes. For six-mode fibers, the two pairs of degenerate modes are the degenerate LP11 and LP21 modes. For CMCFs, the two pairs of degenerate modes are the 2rd and 3rd, 4th and 5th supermodes. The degenerate supermodes have identical effective indexes and thus there is no DMGD between them. The non-degenerate supermodes have different effective indexes. Fortunately, these non-degenerate supermodes/supermode groups can be designed to have low crosstalk by maintaining a large ΔN_{eff} between them. Therefore demultiplexing in SDM using CMCFs can be successfully performed in two steps: i) the non-degenerate supermodes/supermode groups are separately detected while the degenerate supermodes are still mixed together; ii) mixed signals in the degenerate supermodes are recovered by the MIMO-based DSP techniques [18].

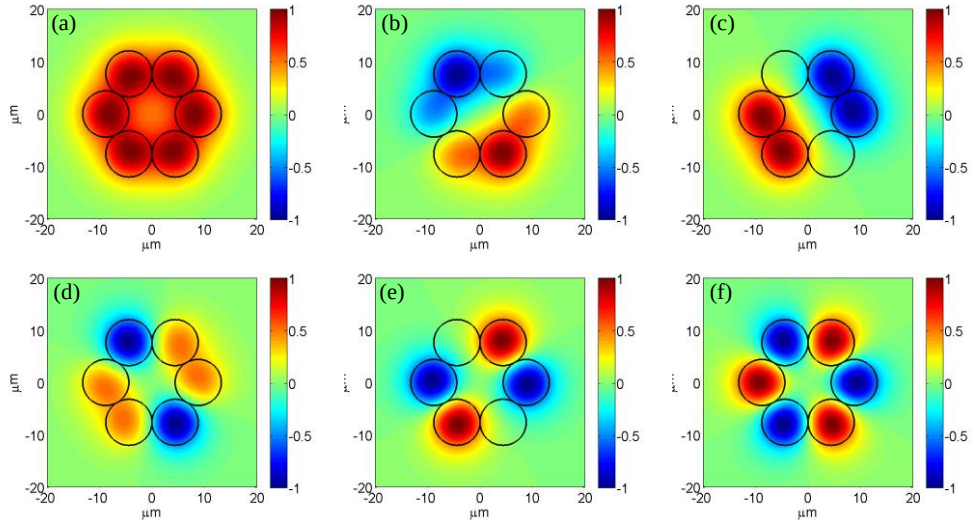

Figure 3-3. Field distributions of the 1st (a), 2nd (b), 3rd (c), 4th (d), 5th (e) and 6th (f) supermodes for the six-core CMCF. (Black lines indicate the boundaries of the cores)

There are three design goals to optimize the performance for SDM: (1) ΔN_{eff} between any two modes should be sufficiently large to avoid mode coupling; (2) mode losses need to be similar to each other and as low as possible; (3) large effective areas are always required for reducing nonlinearity. Based on these goals, 6-core CMCFs and 6-mode fibers are designed respectively and their performances are shown in Fig. 3-4(a) and (b). The macro-bending losses of the fundamental modes for both fibers are fixed at 0.0308 dB/m at a mandrel radius of 20mm. Confinement factor is used here to characterize the mode loss. Higher confinement factor implies lower loss as it indicates less bending loss. From Fig. 3-4(a) and (b), one can see that CMCFs show a significant advantage of attaining large and similar ΔN_{eff}, confinement and A_{eff} for all supermodes. In other words, the supermodes tend to preserve less mode coupling, lower loss and lower nonlinearity than regular modes. All supermodes have similar properties (including mode coupling, loss and nonlinearity), which is crucial for long-distance mode-division-multiplexing.

Higher-order modes in FMF seem to have larger effective areas in Fig. 3-4(a), but these large effective areas actually result from low confinement (as indicated in Fig. 3-4(b)) and hence has no practical benefit.

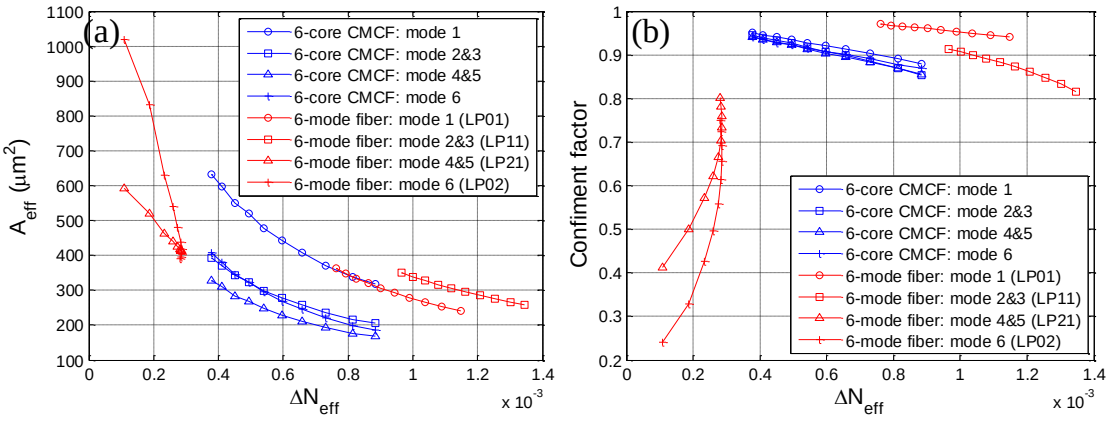

Figure 3-4. A_{eff} vs. ΔN_{eff} for CMCFs and FMFs (ΔN_{eff} refers to the minimum ΔN_{eff} for one mode to any other mode); (b) Confinement factor vs. ΔN_{eff} for CMCFs and FMFs.

3.2.3 Design for long-distance applications

A CMCF design with zero or small DMGD between supermodes has also been considered. In this case, even though supermode coupling may still exist, they travel at the same/similar group velocities. Therefore the supermodes could be detected together and demultiplexing can be performed using MIMO DSP techniques as we mentioned above. According to Eq. (3.6), DMGD between the ith and jth supermodes, can be represented as

$$\mathrm{DMGD(i,j)} = \frac{d\beta_i}{d\omega} - \frac{d\beta_j}{d\omega} = \sum_{n=1}^{2} (a_n^i - a_n^j) \cdot \frac{dc_n}{d\omega} \qquad (3\text{-}8)$$

where a_n^i and a_n^j relate the supermode propagation constant β for the ith and jth supermode, respectively, to the coupling coefficients c_n as given in Eq. (3.7). Using Eq. (3.6), $\frac{dc_n}{d\omega}(n = 1, 2)$ is obtained as,

$$\frac{dc_n}{d\omega} = \frac{1}{r} \cdot \left\{ \begin{array}{l} \frac{\partial}{\partial\omega}\sqrt{1 - \frac{n_2^2(\omega)}{n_1^2(\omega)}} \cdot \left[\frac{U^2}{V^3} \cdot \frac{K_0(Wd_n / r)}{K_1^2(W)} \right] + \ldots \\ \sqrt{1 - \frac{n_2^2}{n_1^2}} \cdot \frac{\partial}{\partial\omega} \left[\frac{U(\omega)^2}{V(\omega)^3} \cdot \frac{K_0(W(\omega) \cdot d_n / r)}{K_1^2(W(\omega))} \right] \end{array} \right\} \qquad (3\text{-}9)$$

It should be noted that Eq. (3.8) is presented for four-core CMCFs, in which DMGD is a linear combination of $\frac{dc_1}{d\omega}$ and $\frac{dc_2}{d\omega}$ with different weighting coefficients for different supermodes. It is clear that in order to achieve zero DMGD among all the supermodes, both $\frac{dc_1}{d\omega}$ and $\frac{dc_2}{d\omega}$ should vanish, which is unlikely if not impossible to realize in a simple step-index profile CMCF. This problem also exists for other CMCF structures where the number of cores is more than three. Therefore three-core CMCFs are chosen here for zero DMGD design as they only contain adjacent core coupling, i.e., only one value of c exists. As a result, total DMGD scales with $\frac{dc_1}{d\omega}$, and it is equivalent to attain zero for $\frac{dc_1}{d\omega}$ in order to achieve zero DMGD in this structure. The mode fields of three-core CMCFs are given in Fig. 3-6, (b), (c) and (d). As shown in Eq. (3.9), $\frac{dc}{d\omega}$ consists of two parts: a frequency dependent index (n_1, n_2) component and a frequency dependent waveguide parameters (V, U, W) component, i.e., the material and

waveguide DMGD. At the first glance, one might think that material DMGD is larger than waveguide DMGD (material dispersion is dominant in chromatic dispersion of standard SMFs). However, it is incorrect to draw an analogy between DMGD and chromatic dispersion because the nature of DMGD is differential modal group delay (DMGD) between modes instead of dispersion within one mode. In fact, all supermodes propagate in the same material but with different propagation constants, implies that the material DMGD should be negligible compared to waveguide DMGD. This conclusion is verified by simulation. Since material DMGD is significantly smaller than waveguide DMGD, they will be neglected in the following discussion to simplify the analysis.

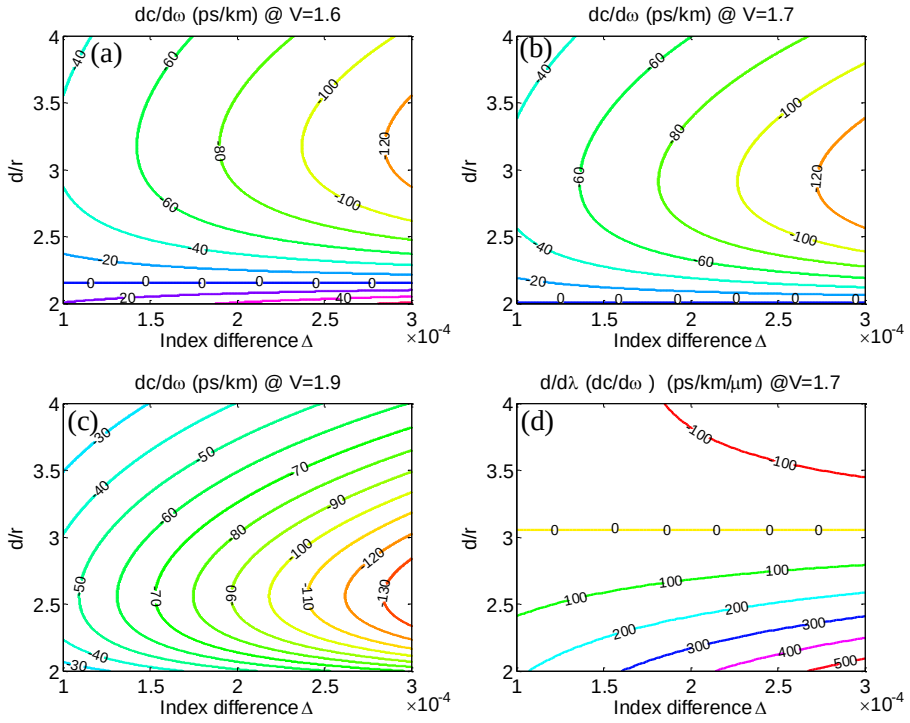

Figure 3-5. (a) (b) (c) $\frac{dc}{d\omega}$ at V=1.6, 1.7 and 1.9. (d) $\frac{d}{d\lambda}\left(\frac{dc}{d\omega}\right)$ at V=1.7.

As indicated in Eq. (3.9), $\frac{dc}{d\omega}$ is determined by the pitch-to-core ratio (d/r), V number and core radius r (or equivalently, V number and index difference Δ since $V = \frac{2\pi}{\lambda_0} r\sqrt{n_1^2 - n_2^2}$). Their relationship is shown in Fig. 3-5(a), (b) and (c). It is confirmed by both analysis and simulation that when the V-number is fixed, zero DMGD is attained if and only if d/r reaches a certain value. As the V-number increases, zero DMGD is realized for a smaller value of d/r, as indicated in Fig. 3-5(a), (b) and (c). So in order to attain zero DMGD, V-number is limited to below 1.71 because d/r cannot less than 2. This is demonstrated by the zero DMGD horizontal lines and their locations with different V-numbers in Fig. 3-5(a), (b) and (c) [in Fig. 3-5(c), with V-number >1.71, the zero DMGD line does not exist]. Apart from zero DMGD, a sufficiently small DMGD is enough for practical use as well. This can be obtained by reducing index difference Δ.

To meet the practical application requirements in a WDM system, CMCFs further require small DMGD variation within a certain range of wavelength, i.e., a small differential modal group delay slope (DMGDS). (DMGDS can be regarded as linear within a narrow range of wavelength). Similar to DMGD, DMGDS between the ith and jth supermodes in a three-core structure can be represented as

$$DMGDS(\mathrm{i,j}) = \frac{d}{d\lambda}\left(\frac{d\beta_i}{d\omega} - \frac{d\beta_j}{d\omega}\right) = (a_{1i} - a_{1j}) \cdot \frac{d}{d\lambda}\left(\frac{dc_1}{d\omega}\right) \qquad (3\text{-}10)$$

Given that material DMGD is negligible, the $\frac{d}{d\lambda}\left(\frac{dc}{d\omega}\right)$ term can be further expressed as

$$\frac{d}{d\lambda}\left(\frac{dC}{d\omega}\right)=\frac{1}{r}\cdot\sqrt{1-\frac{n_2^2}{n_1^2}}\cdot\frac{\partial^2}{\partial\lambda\cdot\partial\omega}\left[\frac{U(\omega)^2}{V(\omega)^3}\cdot\frac{K_0(W(\omega)\cdot d/r)}{K_1^2(W(\omega))}\right] \qquad (3\text{-}11)$$

In Fig. 3-5(d), DMGDS is plotted vs. (d/r) and Δ. Even though zero DMGDS can be realized, they occur at a larger value of d/r with respect to zero DMGD. Therefore, it will be difficult to achieve zero DMGD and DMGDS simultaneously. Even so, DMGDS can still be reduced by decreasing index difference Δ. Wavelength-dependent DMGD as well as mode fields of a specific three-core CMCF design is given in Fig. 3-6 (a) and (b). The DMGD is below 60 ps/km over the entire C band, which is the same value achieved by three-mode fiber using a depressed cladding index profile [18].

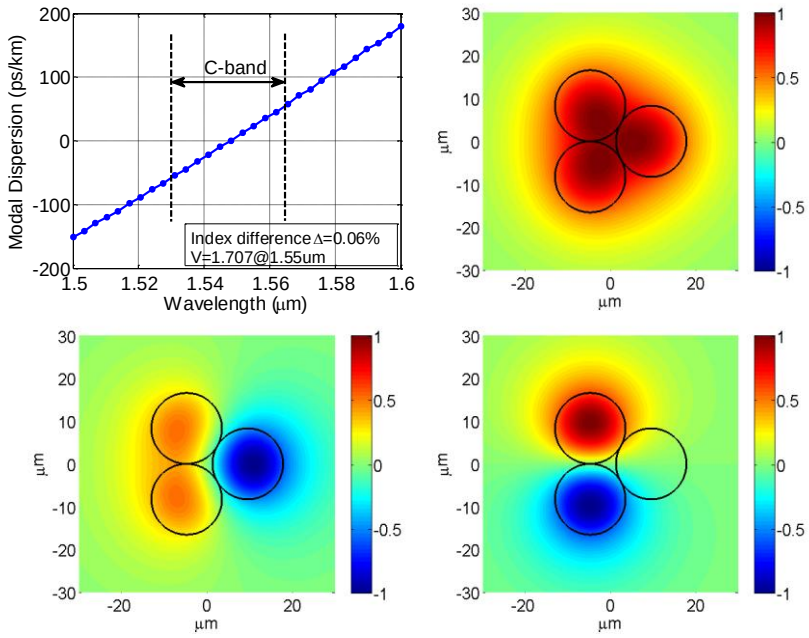

Figure 3-6. (a) maximum DMGD vs. wavelength at V=1.707 @1.55μm and Δ=0.06%, (b) (c) (d) field distribution of the 1st, 2nd and 3rd supermode of a three-core CMCF

3.3 Higher-Order Supermodes in Coupled Few-Mode Core Fibers

When the guiding power is increased for an isolated core, it can guide high-order modes. For optical fibers with low refractive index contrast, the vector modes are weakly guided and therefore can be treated as linear polarization (LP) modes. In essence, the LP modes are scalar approximations of the vector mode fields and contain only one transverse field component given by,

$$E_{pq}(r,\theta)=\begin{cases} U\dfrac{J_p(\kappa_{pq}\cdot r)}{J_p(\kappa_{pq}\cdot a)}\cos(p\theta+\varphi), & \text{for } r\le a \\ U\dfrac{K_p(\gamma_{pq}\cdot r)}{K_p(\gamma_{pq}\cdot a)}\cos(p\theta+\varphi), & \text{for } r>a \end{cases} \qquad (3\text{-}12)$$

where U is the complex amplitude, J and K are Bessel functions of the first and second kind, a is the core radius, φ is an arbitrary start angle, and p is a non-negative integer referred to as the azimuthal mode order. For the same p value, κ_{pq} and γ_{pq} can take on multiple discrete values determined from the dispersion relation. Therefore it is appropriate to label each of the aforementioned terms with another non-negative integer corresponding to the number of times the field crosses zero along the radial direction. Thus, the *LP* modes can be labeled as LP_{pq}. The orthogonal field component is the same as Eq. (3-12) therefore the results presented here applies to either polarization. According to Eq. (3-12), when $p>0$, the modal field has an additional degree of freedom in the azimuthal direction because the start angle φ is arbitrary, which generates spatially orthogonal modes even if both p and q are the same. For example the LP_{11x} and LP_{11y} modes correspond to the cases of $\varphi=0$ and respectively, shown

in Fig. 3-7. This is very different from the case of $p = 0$ where the LP_{0q} modal field is azimuthally uniform and has no spatial degeneracy.

To the best of our knowledge, until now the study of supermodes has been limited to the supermodes composed of these azimuthally uniform LP_{pq} (p =0) "core modes", particularly LP_{01} supermodes. However, the higher-order LP_{pq} (p >0) "core modes" can also form supermodes. Moreover, these supermodes are strongly affected by the geometrical distribution of the cores within the MCF, because the coupling of LP_{pq} (p >0) modes between two cores varies significantly with initial angles of the modes. We name these angle-dependent supermodes as "higher-order supermodes." Unlike the higher-order core modes (p or q >0), higher-order supermodes specifically refer to the supermodes formed because of coupling among "core modes" with p >0. In this section, we begin the study of higher-order supermodes from the simplest two-core structure by demonstrating how angle-dependent coupling influences the eigenmode formation. Then, we extend the theory to more complex geometrical structures, using symmetries to produce analytical formulas for higher-order supermodes. More specifically, we derive formulas for commonly used formations, including linear-array, grid-array and ring-array structures.

3.3.1 Higher-Order Supermodes in a Two-Core Structure

As described above, the coupling between two LP_{pq} (p >0) modes strongly depends on the initial angles of both modes. In order to focus on this angular dependence, the LP_{pq} (p >0) modal field of Eq. (3-12) is written as a function of the initial angle φ

$$\begin{aligned} E(\varphi) &= F_r \cdot \cos(p\theta - \varphi) \\ &= E_x \cdot \cos\varphi + E_y \cdot \sin\varphi \end{aligned} \qquad (3\text{-}13)$$

where F_r represents the radial component of the modal field, $E_x = E(\varphi = 0)$ and $E_y = E(\varphi = \frac{\pi}{2})$ correspond to the modal fields aligned with the horizontal axis x and vertical axis y. A coordinate system is selected where the azimuthal reference axis is parallel to the edge of the graph formed by vertices at the center of the isolated cores as shown in the inset of Fig. 3-7. The coupling coefficient between two LP_{pq} (p >0) modal fields with initial angles of φ_1 and φ_2, respectively, in the two identical cores 1 and 2 is given by

$$\begin{aligned} \kappa(E_1(\varphi_1), E_2(\varphi_2)) &= \frac{\omega}{2} \iint_{Core2} \varepsilon_0 (n_{CoreB}^2 - n_{Clad}^2) \cdot E_1^*(\varphi_1) \cdot E_2(\varphi_2) dxdy \\ &= \kappa_x \cdot \cos\varphi_1 \cos\varphi_2 + \kappa_y \cdot \sin\varphi_1 \sin\varphi_2 + \kappa_{xy} \cdot \cos\varphi_1 \sin\varphi_2 + \kappa_{yx} \cdot \sin\varphi_1 \cos\varphi_2 \end{aligned} \qquad (3\text{-}14)$$

where $\kappa_x = \kappa(E_{1,x}, E_{2,x})$, $\kappa_y = \kappa(E_{1,y}, E_{2,y})$, $\kappa_{xy} = \kappa(E_{1,x}, E_{2,y})$, $\kappa_{yx} = \kappa(E_{1,y}, E_{2,x})$. The modal fields are normalized, ε_0 and ω are vacuum permittivity and angular frequency, n_{Core2} and n_{Clad} are the refractive indices of core 2 and the cladding, respectively. Fig. 3-7 represents the typical behavior of the coupling coefficient as the initial angles of two LP_{11} modes change, according to Eq. (3-14). $\kappa_x > \kappa_y > 0$ is observed as a result of the specific geometrical distribution of modal fields with respect to the cores. More importantly, coupling vanished for two specific initial

angles, i.e., $\kappa_{xy} = \kappa_{yx} = 0$, as illustrated in by the arrow in Fig. 3-7. This phenomenon occurs because the mirror-reversal of two modal fields across an axis parallel to the reference axis should have the same coupling coefficient, which can be mathematically elaborated as

$$\begin{aligned}\kappa_{xy} &= \frac{\omega}{2}\iint_{Core2} \varepsilon_0(n_{CoreB}^2 - n_{Clad}^2)\cdot F_{1,r}^{*}\cos(\theta_1)\cdot F_{2,r}\sin(\theta_2)dxdy \\ &= \frac{\omega}{2}\iint_{Core2} \varepsilon_0(n_{CoreB}^2 - n_{Clad}^2)\cdot F_{1,r}^{*}\cos(-\theta_1)\cdot F_{2,r}\sin(-\theta_2)dxdy \\ &= -\kappa_{yx} = 0\end{aligned} \qquad (3\text{-}15)$$

With this result, Eq. (3-14) can be immediately simplified as

$$\kappa(E_1(\varphi_1), E_2(\varphi_2)) = \kappa_x \cdot \cos\varphi_1 \cos\varphi_2 + \kappa_y \cdot \sin\varphi_1 \sin\varphi_2. \qquad (3\text{-}16)$$

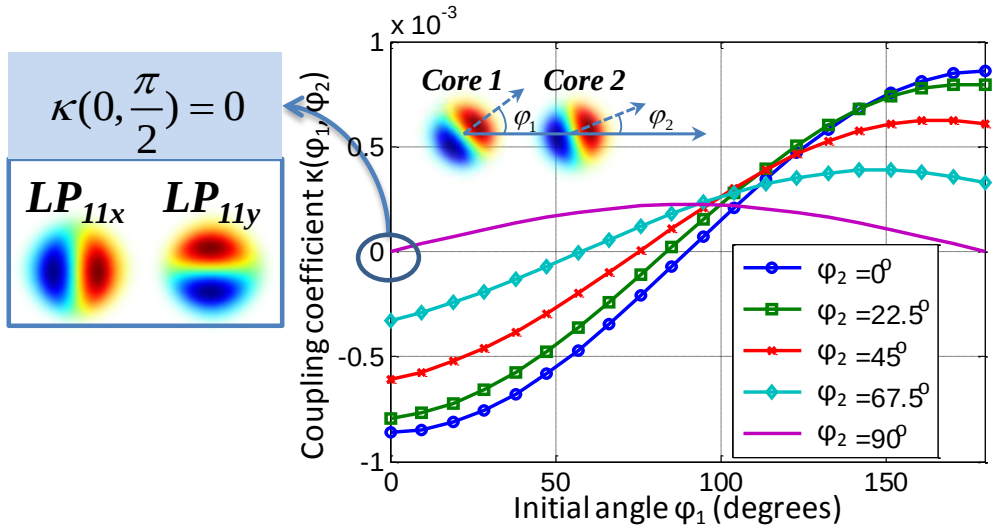

Figure 3-7. Coupling between two arbitrarily oriented LP_{11} degenerate modes as a function of their initial angles φ_1 and φ_2. The arrow points to the position of zero coupling $\kappa(\varphi_1 = 0, \varphi_2 = \pi/2) = 0$ between the LP_{11x} and LP_{11y} modes; the inset shows the coordinate system of the two cores including reference axes and two initial angles.

Similar to the LP_{01} supermodes, higher-order supermodes can be investigated using coupled-mode theory under the assumption of weak coupling. For the simplest case of the two-

core structure, the basis set for each core is strategically chosen as the E_x and E_y pair, even though it could have been any orthogonal set with an arbitrary initial angle. Then the interactions between the "core modes" can be described by the following coupled-mode equation in a matrix form

$$i\frac{d}{dz}\boldsymbol{U} + \bar{\boldsymbol{M}}\boldsymbol{U} = 0, \qquad (3\text{-}17)$$

where $\boldsymbol{U} = [u_{1,x} \quad u_{2,x} \quad u_{1,y} \quad u_{2,y}]^T$; $u_{m,x}$ or $u_{m,y}$ are the complex amplitude of the horizontally or vertically aligned modal field of the mth core after adopting the gauge transformation $u_{m,x/y} = U_{m,x/y} \cdot e^{i\beta_0 z}$ in which β_0 is the propagation constant of any isolated core mode LP_{pq}; and hence is a 4-by-4 coupled matrix

$$\bar{\boldsymbol{M}} = \begin{bmatrix} 0 & \kappa_x & 0 & \kappa_{xy} \\ \kappa_x & 0 & \kappa_{xy} & 0 \\ 0 & \kappa_{yx} & 0 & \kappa_y \\ \kappa_{yx} & 0 & \kappa_y & 0 \end{bmatrix}. \qquad (3\text{-}18)$$

The standard procedure of solving the coupled-mode equation is to diagonalize the coupled matrix $\boldsymbol{Q}^{-1}\bar{\boldsymbol{M}}\boldsymbol{Q} = \boldsymbol{\Lambda}$ where the eigenvalues λ give the normalized propagation constants of the supermodes. The corresponding eigenvectors $\boldsymbol{U'} = \boldsymbol{Q}^{-1}\boldsymbol{U}$ describes the supermode field amplitudes and the row vectors of $\boldsymbol{A} = \boldsymbol{Q}^{-1}$ represents the amplitude coefficients of superposition of core modes in forming the supermodes. In the supermode basis, the coupled-mode equation reduces to

$$i\frac{d}{dz}\boldsymbol{U'} + \boldsymbol{\Lambda}\boldsymbol{U'} = 0. \qquad (3\text{-}19)$$

For this particular coupled-mode equation, one can apply $\kappa_{xy} = \kappa_{yx} = 0$ first and then divide the equation into two reduced ones as follows,

$$i\frac{d}{dz}\begin{bmatrix} u_{1,x} \\ u_{2,x} \end{bmatrix} + \begin{bmatrix} 0 & \kappa_x \\ \kappa_x & 0 \end{bmatrix}\begin{bmatrix} u_{1,x} \\ u_{2,x} \end{bmatrix} = 0 \qquad (3\text{-}20a)$$

$$i\frac{d}{dz}\begin{bmatrix} u_{1,y} \\ u_{2,y} \end{bmatrix} + \begin{bmatrix} 0 & \kappa_y \\ \kappa_y & 0 \end{bmatrix}\begin{bmatrix} u_{1,y} \\ u_{2,y} \end{bmatrix} = 0. \qquad (3\text{-}20b)$$

The above equations mean that E_x and E_y, the horizontally and vertically aligned "core modes" do not "talk to" each other and their formation of higher-order supermodes can be solved separately. Eqs. (3-20a) and (3-20b) turn out to be very similar to those for the case of LP_{01} supermodes. The amplitude coefficients of the higher-order supermode corresponding to the row vectors of $\boldsymbol{A} = \boldsymbol{Q}^{-1} = \frac{1}{\sqrt{2}}[1,1;1,-1]$ are the same as those for the LP_{01} supermodes. For higher-order supermodes composed of E_x and E_y respectively, as shown in Fig. 3-8, the propagation constants of the four higher-order supermodes $\beta = \beta_0 + \lambda$ are calculated to be $\beta_0 \pm 2\kappa_x$ and $\beta_0 \pm 2\kappa_y$, respectively.

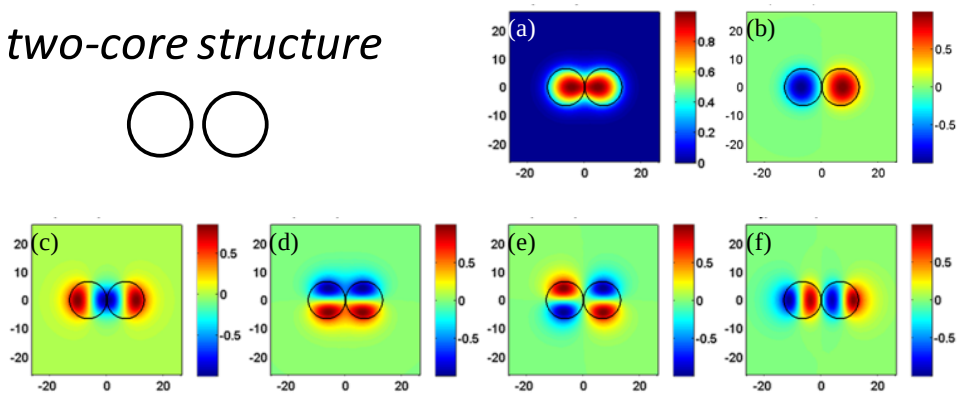

Figure 3-8. Modal fields of LP_{01} supermodes (a & b) and LP_{11} supermodes (c-f) of a basic two-core structure. In-phase supermodes are shown in (a), (c) and (d) while out-of phase supermodes are shown in (b), (e) and (f).

3.3.2 Higher-Order Supermodes in Linear-Array Structures

A slightly more complex structure is the linear array where the cores are linearly aligned with each other with equal core-to-core distances as shown in Fig. 3-9. In this case, couplings between non-adjacent cores are expected to be negligible. Let us start with the LP_{01} supermodes, which do not have angular dependence. One could solve the eigen-problem of the coupled-mode equation as described in the last section and obtain the supermodes. The alternative method is to find the solutions that satisfy the boundary conditions $u_0 = u_{N+1} = 0$ [123]. As a result, the amplitude of the mth core within any LP_{01} supermode can be described as

$$A_m = a \cdot e^{imQ} + b \cdot e^{-imQ},\ m = 1, 2, \cdots N \qquad (3\text{-}21)$$

where a and b are coefficients; Q is the common phase acquired by shifting any one lattice due to the translational symmetry. The boundary conditions applied to both sides of the linear structure ($m = 0$ and $m = N + 1$)

$$\begin{aligned} A_{N+1} &= a \cdot e^{i(N+1)Q} + b \cdot e^{-i(N+1)Q} \\ &= A_0 = a \cdot e^{i0} + b \cdot e^{-i0} = 0, \end{aligned} \quad (3\text{-}22)$$

yield $a + b = 0$ and $Q = \frac{\pi l}{N+1}$, $l = 1, 2, \cdots N$. Therefore the LP_{01} supermode can be written as

$$u'_{l,m} = A_{l,m} \cdot u_{l,m} = \sin\left(\frac{\pi l m}{N+1}\right) \cdot u_{l,m}, \; m, l = 1, 2, \cdots N \quad (3\text{-}23)$$

where l corresponds to the order of different supermodes and u_m represents the complex amplitude of the m^{th} "core mode". For the l^{th} LP_{01} supermode, comparing the coupled-mode equation

$$i\frac{d}{dz}u_m + \kappa(u_{m-1} + u_{m+1}) = 0, \quad (3\text{-}24)$$

with the supermode equation

$$i\frac{d}{dz}u'_m + \lambda_l u'_m = 0 \quad (3\text{-}25)$$

where κ is the coupling coefficient between two adjacent LP_{01} "core modes", the propagation constant of the l^{th} LP_{01} supermode $\beta_l = \beta_0 + \lambda_l$ can be obtained as

$$\beta_l = \beta_0 + 2\kappa \cdot \cos\left(\frac{\pi l}{N+1}\right), \; l = 1, 2 \cdots N. \quad (3\text{-}26)$$

For higher-order supermodes, because only coupling between adjacent cores is considered, E_x modes would only couple to themselves as would E_y modes, according to $\kappa_{xy} = \kappa_{yx} = 0$. Therefore the higher-order supermodes of the linear-array structure can be divided

into the E_x - and E_y -families; each of them can be solved independently using the same relations as used for the LP_{01} supermode. The propagation constants are attained as

$$\beta_{l,x} = \beta_0 + 2\kappa_x \cdot \cos\left(\frac{\pi l}{N+1}\right),\ l = 1, 2 \cdots N \qquad (3\text{-}27a)$$

$$\beta_{l,y} = \beta_0 + 2\kappa_y \cdot \cos\left(\frac{\pi l}{N+1}\right),\ l = 1, 2 \cdots N \qquad (3\text{-}27b)$$

respectively. An example of the LP_{11} supermodes as well as the LP_{01} supermodes of a 4-core linear-array structure is shown in Fig. 3-9.

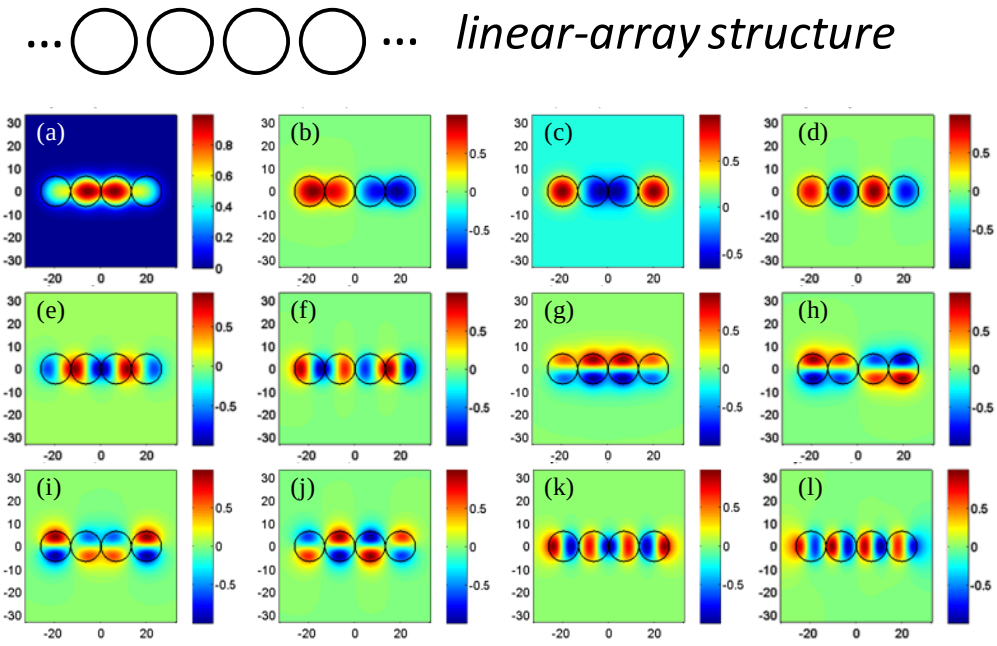

Figure 3-9. Modal fields of LP_{01} supermodes (a-d) and LP_{11} supermodes (e-l) of a 4-core linear-array structure.

3.3.3 Higher-Order Supermodes in 2D Rectangular-Array Structures

We then analyze the supermodes in two dimensional (2D) discrete waveguide arrays. These are composed of $M \times N$ identical optical waveguides arranged in a rectangular geometry. The distance between cores is taken here to be D. For generality, we also include in our analysis not only nearest neighbor interactions κ (occurring along the horizontal and vertical directions) but also higher-order couplings κ_c taking place along the two diagonals as shown in Fig. 3-10(a). For weakly guiding structures, the coupling strengths can be obtained from $\kappa = \frac{\sqrt{2\Delta}}{a}\frac{U^2}{V^3}\frac{K_0(WD/a)}{K_1^2(W)}$. We first consider supermodes derived from the LP_{01} mode supported by each waveguide channel in a square lattice (see Fig. 3-10(a)). In such an arrangement, the modal fields evolve according to :

$$\begin{aligned} & i\frac{dU_{m,n}}{dz} + \beta_0 U_{m,n} + \kappa\left(U_{m+1,n} + U_{m-1,n} + U_{m,n+1} + U_{m,n-1}\right) + \\ & \kappa_c\left(U_{m+1,n+1} + U_{m+1,n-1} + U_{m-1,n+1} + U_{m-1,n-1}\right) = 0 \end{aligned} \qquad (3\text{-}28)$$

where $U_{n,m}$ represents the modal field amplitude at site n, m in this rectangular array and the discrete site indices take values from the sets $n = 1,2,\ldots,N$ and $m = 1,2,\ldots,M$. To identify the eigenmodes of this system, we look for solutions of the type $U_{m,n} = e^{i\beta_0 z}u_{m,n}$ that also satisfy the boundary conditions $u_{m,0} = u_{m,N+1} = u_{0,n} = u_{M+1,n} = 0$ [124]. Based on these requirements, one can directly show that the $U^{k,l}$ supermodes of this structure are $U_{m,n}^{k,l} = A_{m,n}^{k,l}e^{i\beta_0 z}e^{i\lambda_{k,l}z}$ with the amplitudes given by

$$A_{m,n}^{k,l} = \sin\left(m\frac{k\pi}{M+1}\right)\sin\left(n\frac{l\pi}{N+1}\right) \qquad (3\text{-}29)$$

where $k = 1,2,\ldots,M$ and $l = 1,\ldots,N$. In addition, the eigenvalue associated with $U^{k,l}$ supermode is given by

$$\lambda_{k,l} = 2\kappa\left[\cos\left(\frac{k\pi}{M+1}\right)+\cos\left(\frac{l\pi}{N+1}\right)\right]+4\kappa_c\cos\left(\frac{k\pi}{M+1}\right)\cos\left(\frac{l\pi}{N+1}\right) \qquad (3\text{-}30)$$

Evidently, altogether this array supports $M \times N$ supermodes.

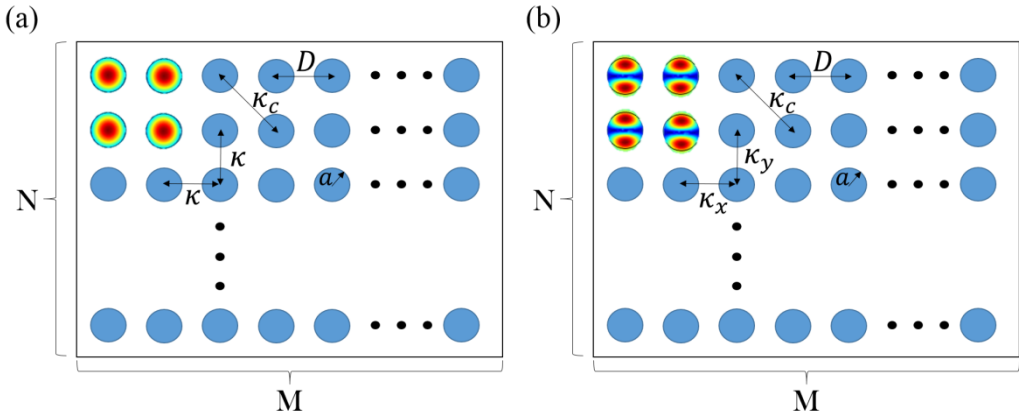

Figure 3-10. (a) A rectangular array of waveguides. The LP_{01} mode in each waveguide cross-talks with nearest neighbors along the horizontal and vertical directions as well as with diagonal elements. (b) Coupling interactions in this same array when each element involves instead the LP_{11} mode.

Similarly, one can investigate the eigenmodes of this same array arising from the LP_{11} mode of each waveguide (Fig. 3-10(b)). In a weakly coupled array, the LP_{11} mode tends to orient itself either along the x or y direction (LP_{11x}, LP_{11y}). As a result the coupling strengths κ_x and κ_y are different because of their respective overlap integrals. Hence, the field evolution is described by

$$i\frac{dU_{m,n}}{dz}+\beta_0 U_{m,n}+\kappa_x\left(U_{m+1,n}+U_{m-1,n}\right)+\kappa_y\left(U_{m,n+1}+U_{m,n-1}\right)+$$
$$\kappa_c\left(U_{m+1,n+1}+U_{m+1,n-1}+U_{m-1,n+1}+U_{m-1,n-1}\right)=0 \qquad (3\text{-}31)$$

The supermodes $U^{k,l}$ of this latter equation are exactly identical in form with those provided by Eq. (3-29). In this case however, the corresponding eigenvalues are given by

$$\lambda_{k,l}=2\kappa_x\cos\left(\frac{k\pi}{M+1}\right)+2\kappa_y\cos\left(\frac{l\pi}{N+1}\right)+4\kappa_c\cos\left(\frac{k\pi}{M+1}\right)\cos\left(\frac{l\pi}{N+1}\right) \qquad (3\text{-}32)$$

In all cases our results (based on coupled-mode theory) are in excellent agreement with finite element simulations using COMSOL as shown in Fig. 3-11.

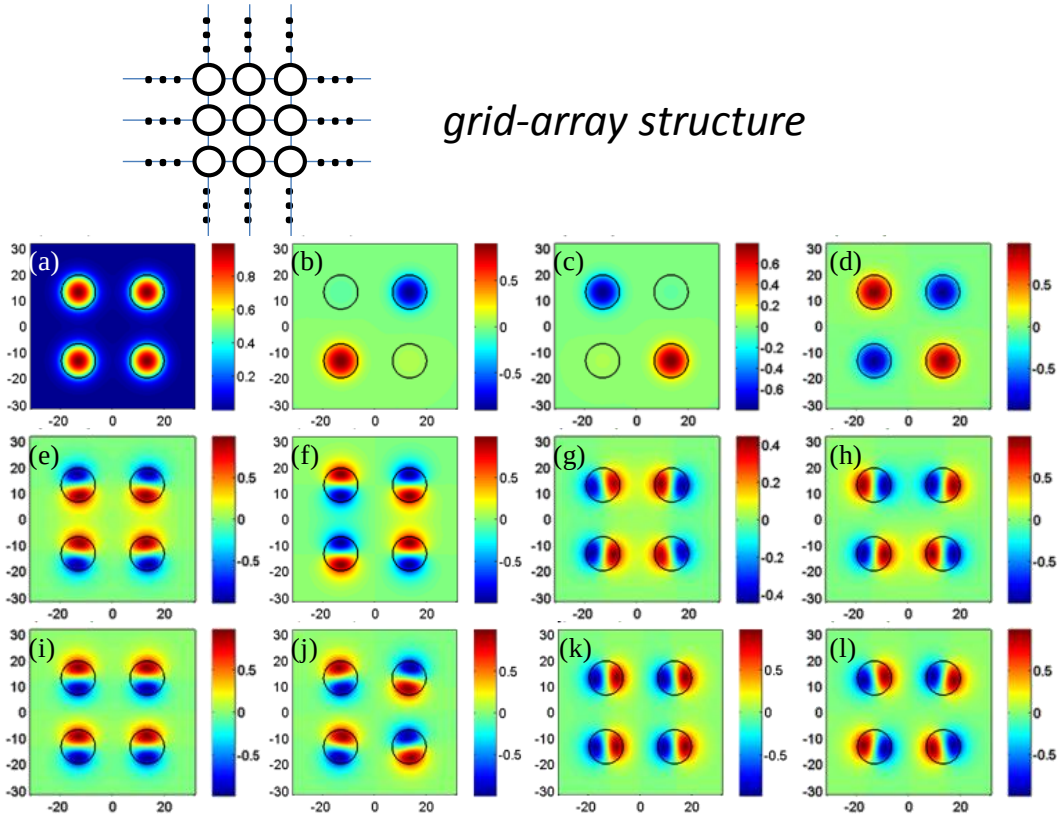

Figure 3-11. (a) Scheme of mode basis selection for LP_{11} supermode analysis of a 4-core grid-array structure; modal fields of LP_{01} supermodes (a-d) and LP_{11} supermodes (e-l) of a 4-core grid-array structure computed using COMSOL

3.3.4 Higher-Order Supermodes in Ring-Array Structures

Ring-array structure is another interesting geometry for higher-order supermodes as it possesses rotational symmetry. Here also, we only consider coupling between adjacent cores. We start from LP_{01} supermodes of N-core ring-array structure. In this case, the coupled matrix $\bar{\boldsymbol{M}}$ is a symmetric circulant matrix. If β_0 and κ are defined as the propagation constant of the "core mode" and the coupling coefficient between two adjacent LP_{01} "core modes" respectively, the elements of the N-by-N coupled matrix are given as

$$(\bar{\boldsymbol{M}})_{lm} = \beta_0 \delta_{lm} + \kappa\left(\delta_{l+1,m} + \delta_{l,m+1}\right) \qquad (3\text{-}33)$$

where δ_{lm}, $\delta_{l+1,m}$ and $\delta_{l,m+1}$ are Kronecker deltas; l and m are integer numbers mod N. This matrix can be diagonalized by a lattice Fourier transform as $\boldsymbol{\Lambda} = \boldsymbol{Q}^{-1}\bar{\boldsymbol{M}}\boldsymbol{Q}$ [112]. $\boldsymbol{Q}^{-1}$ is a unitary matrix with elements given as

$$(\boldsymbol{Q}^{-1})_{lm} = \frac{1}{\sqrt{N}} e^{i\frac{2\pi l}{N}\cdot m} \qquad (3\text{-}34)$$

which represents the amplitude of m^{th} core for the l^{th} LP_{01} supermode. These discrete helical phases give supermodes an appearance similar to optical vortices but in a discrete form and thus carry orbital angular momentum [111]. The propagation constant of the l^{th} LP_{01} supermode equals the corresponding eigenvalue and can be calculated as

$$\beta_l = \beta_0 + 2\kappa \cdot \cos\left(\frac{2\pi l}{N}\right),\ l = 1, 2 \cdots N. \qquad (3\text{-}35)$$

According to Eq. (3.24), it is obvious that the l^{th} and $(N-l)^{th}$ supermodes are degenerate modes. This has a physical explanation from the equivalence between clockwise and counter-

clockwise mode orders. A unitary transformation can project the vortex-like basis of the l^{th} and $(N-l)^{th}$ supermodes into another orthogonal basis. In particular, the degenerate supermodes can be transformed into a basis in real fields with amplitude transformation as below

$$\begin{bmatrix} B_{l,m} \\ B_{N-l,m} \end{bmatrix} = \frac{1}{\sqrt{2}} \begin{bmatrix} 1 & 1 \\ 1 & -1 \end{bmatrix} \begin{bmatrix} A_{l,m} \\ A_{N-l,m} \end{bmatrix} \quad (3\text{-}36)$$

where $B_{l,m} = \sqrt{\frac{2}{N}} \cos\left(\frac{2\pi l}{N} \cdot m \right)$ and $B_{N-l,m} = \sqrt{\frac{2}{N}} \sin\left(\frac{2\pi l}{N} \cdot m \right)$.

The higher-order supermodes of ring-array structure are particularly interesting because they can no longer be divided into E_x - and E_y -basis for independent analysis. Instead, the tangential and normal mode basis E_{t_m} and E_{n_m} (m refers to the core number) are selected, which correspond to "core modes" aligned horizontally or vertically with respect to the reference axis pointing from the ring center to the m^{th} core. Figure 3-12(a) shows such a mode basis for a 3-core ring-array structure. In that case, $\kappa_{1,2} = \kappa_{2,3} = \kappa_{3,1}$ is obtained because of the rotational symmetry. In addition, the coupling coefficients between the LP_{pq} modes are real so that $\kappa_{i,j} = \kappa_{j,i}$. Therefore the number of coupling coefficients for the N-core ring-array structure is reduced from 2N to 4 given by

$$\kappa_{t_1,t_2} = -\kappa_x \sin^2\left(\frac{\pi}{N} \right) + \kappa_y \cos^2\left(\frac{\pi}{N} \right), \quad (3\text{-}37a)$$

$$\kappa_{t_1,n_2} = -\kappa_x \sin\left(\frac{\pi}{N} \right) \cos\left(\frac{\pi}{N} \right) - \kappa_y \sin\left(\frac{\pi}{N} \right) \cos\left(\frac{\pi}{N} \right), \quad (3\text{-}37b)$$

$$\kappa_{n_1,t_2} = \kappa_x \sin\left(\frac{\pi}{N} \right) \cos\left(\frac{\pi}{N} \right) + \kappa_y \sin\left(\frac{\pi}{N} \right) \cos\left(\frac{\pi}{N} \right), \quad (3\text{-}37c)$$

$$\kappa_{n_1,n_2} = \kappa_x \cos^2\left(\frac{\pi}{N}\right) - \kappa_y \sin^2\left(\frac{\pi}{N}\right). \qquad (3\text{-}37d)$$

Then the coupled-mode equation for the N-core ring-array can be written as

$$i\frac{d}{dz}\begin{bmatrix}\boldsymbol{U}_t\\ \boldsymbol{U}_n\end{bmatrix} + \bar{\boldsymbol{M}}\begin{bmatrix}\boldsymbol{U}_t\\ \boldsymbol{U}_n\end{bmatrix} = 0, \qquad (3\text{-}38)$$

where $\boldsymbol{U}_t$ and $\boldsymbol{U}_n$ are column vectors of dimension N. the coupled matrix $\bar{\boldsymbol{M}} = \begin{bmatrix}\boldsymbol{M}_{tt} & \boldsymbol{M}_{tn}\\ \boldsymbol{M}_{nt} & \boldsymbol{M}_{nn}\end{bmatrix}$ is a rank-2N Hermitian matrix and each sub-matrix is a circulant matrix with elements described as

$$\left(\boldsymbol{M}_{tt}\right)_{lm} = \kappa_{t_1,t_2}\left(\delta_{l+1,m} + \delta_{l,m+1}\right), \qquad (3\text{-}39a)$$

$$\left(\boldsymbol{M}_{tn}\right)_{lm} = \kappa_{t_1,n_2}\delta_{l+1,m} + \kappa_{n_1,t_2}\delta_{l,m+1}, \qquad (3\text{-}39b)$$

$$\left(\boldsymbol{M}_{nt}\right)_{lm} = \kappa_{n_1,t_2}\delta_{l+1,m} + \kappa_{t_1,n_2}\delta_{l,m+1}, \qquad (3\text{-}39c)$$

$$\left(\boldsymbol{M}_{nn}\right)_{lm} = \kappa_{n_1,n_2}\cdot\left(\delta_{l,m+1} + \delta_{l+1,m}\right). \qquad (3\text{-}39d)$$

where δ_{lm}, $\delta_{l+1,m}$ and $\delta_{l,m+1}$ are the Kronecker deltas; l and m are integer numbers mod N. Diagonalization of the coupled matrix $\boldsymbol{M}$ is the key to solving the higher-order supermodes. It takes two steps as follows as described in appendix A.

Both the eigenvalues and eigenvectors can be obtained after successful diagonalization of the coupled matrix. After plugging the coupling coefficients into the eigenvalues and eigenvectors using Eq. (3.22), the higher-order supermodes can be divided into $(\pm)$ groups and solved as

$$E_l^{(\pm)} = \begin{cases} \sum_{m=1}^{N}\left(e^{i\frac{2\pi l}{N}\cdot m}E_{t_m}\right) + \gamma_l^{(\pm)}\cdot\sum_{m=1}^{N}\left(e^{i\frac{2\pi l}{N}\cdot m}E_{n_m}\right), & \text{if } \sin\left(\frac{2\pi l}{N}\right)\neq 0 \\ \sum_{m=1}^{N}\left(e^{i\frac{2\pi l}{N}\cdot m}E_{t_m}\right) \text{ or } \sum_{m=1}^{N}\left(e^{i\frac{2\pi l}{N}\cdot m}E_{n_m}\right), & \text{if } \sin\left(\frac{2\pi l}{N}\right)= 0 \end{cases} \qquad (3\text{-}40)$$

where $\gamma_l^{(\pm)} = -i\left(\eta \pm \sqrt{1+\eta^2}\right)$ and $\eta = \dfrac{(\kappa_x - \kappa_y)\cot\left(\dfrac{2\pi l}{N}\right)}{(\kappa_x + \kappa_y)\sin\left(\dfrac{2\pi l}{N}\right)}$. The propagation constants of the higher-order supermodes are the eigenvalues

$$\beta_l^{(\pm)} = \beta_0 + (\kappa_x + \kappa_y)\cdot\cos\left(\frac{2\pi}{N}\right)\cdot\cos\left(\frac{2\pi l}{N}\right) \pm \ldots \sqrt{(\kappa_x - \kappa_y)^2\cdot\cos^2\left(\frac{2\pi l}{N}\right) + (\kappa_x + \kappa_y)^2\cdot\sin^2\left(\frac{2\pi}{N}\right)\cdot\sin^2\left(\frac{2\pi l}{N}\right)}, \quad \text{(3-41)}$$

where $l = 1, 2\cdots N$. Same as the LP_{01} supermodes, the l^{th} and $(N-l)^{th}$ higher-order supermodes for both $(\pm)$ groups are degenerate. Real-field basis can be obtained by applying a unitary transformation on the current basis. An example of the LP_{11} supermodes as well as the LP_{01}-supermodes of a 3-core ring-array structure is shown in Fig. 3-12(b-j).

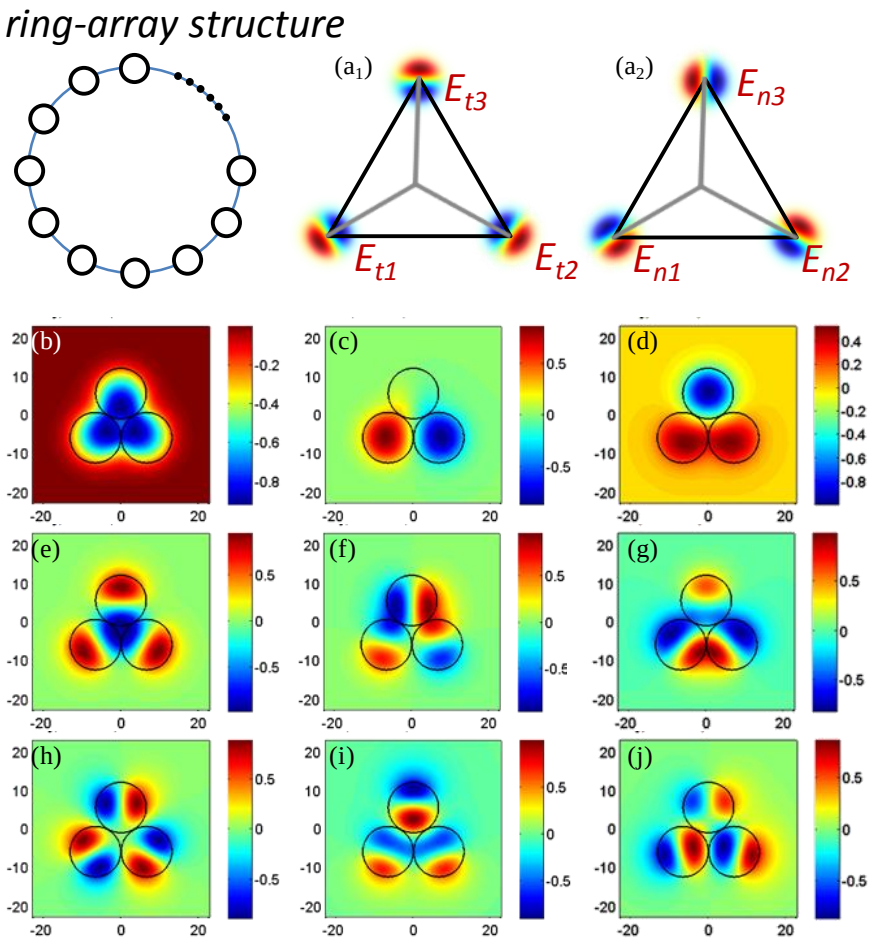

Figure 3-12. (a) Scheme of mode basis selection for LP_{11} supermode analysis of a 3-core ring-array structure; modal fields of LP_{01} supermodes (b-d) and LP_{11} supermodes (e-j) of a 3-core ring-array structure computed using COMSOL.

3.3.5 Observation of Higher-Order Supermodes

A coupled few-mode 3-core fiber was fabricated in order to observe higher-order supermodes. The cross-section of the fiber is shown in Fig. 3-14(a), where the Ge-doped cores are hexagonally-shaped as a result of the stack-and-draw fabrication process. The cladding

diameter is ~120μm, and the index difference between the core and cladding is ~0.6%. The core diameter was selected to be ~9μm to ensure that the cut-off wavelength of the fundamental modes is well above 1.5μm. In addition, the core pitch was chosen to be ~11.5μm, a small enough distance to allow for strong coupling. Therefore the fiber supports both LP_{01} and LP_{11} supermodes around 1.5μm.

A spectrally-and-spatially resolved imaging (S^2 imaging) setup was built to acquire the modal fields from the fiber. The S^2 imaging procedure, first developed by J. W. Nicholson et al. [125], is a technique specially designed for quantifying mode content in fibers. The principle is to spatially resolve, in a point-by-point fashion, the spectral multi-path interference patterns produced by mode beatings. The imaging setup can either involve a broadband source accompanied by a spatial-scanning system or a tunable laser source accompanied by a CCD camera. For the purposes of this experiment, we chose the latter setup as shown in Fig. 3-13(a) due to its fast scanning speed and high frequency resolution. Both the tunable laser and the camera scan in sub-seconds and can be easily synchronized by computer control. In addition, the tunable laser supports a fine resolution of 0.0001nm with a tuning range of 1510nm-1640nm. Light coupled from the tunable laser source was launched into approximately 7m of the fabricated 3-core fiber through free space. The output of the 3-core fiber is imaged onto the camera through a 4-f optical system. A polarizer was added in front of the camera to guarantee a single polarization. During the scanning operation, the laser wavelength was incremented in discrete steps and a mode-interference image was captured by the camera at each step. The measured S^2 results can be expressed as wavelength-interference patterns for every image pixel. Because modes travel at different group velocities, if three modes are assumed to be excited with

amplitudes A, B, C and phase ϕ_a, ϕ_b, ϕ_c, the measured intensity at each pixel location (x, y) would be

$$\begin{aligned} I(\omega)\Big|_{(x,y)} &= | A(x,y)\cdot e^{i\phi_a(x,y)}\cdot e^{-i\omega\cdot 0} + B(x,y)\cdot e^{i\phi_b(x,y)}\cdot e^{-i\omega\cdot\tau_{ab}} + C(x,y)\cdot e^{i\phi_c(x,y)}\cdot e^{-i\omega\cdot\tau_{ac}} | \\ &= (A^2+B^2+C^2) + 2AB\cdot\cos(\Delta\phi_{ab}-\omega\cdot\tau_{ab}) + ... \\ &\quad 2AC\cdot\cos(\Delta\phi_{ac}-\omega\cdot\tau_{ac}) + 2BC\cdot\cos(\Delta\phi_{bc}-\omega\cdot\tau_{bc}), \end{aligned} \quad (3\text{-}42)$$

where ω is the angular frequency and τ_{ij} represents the differential group delay between mode i and mode j. An example of a measurement at a particular pixel location is plotted as shown in Fig. 3-13(b). Using that data, one can extract all the mode information by simply applying a Fourier transform as follows

$$\begin{aligned} \hat{I}(\tau)\Big|_{(x,y)} &= (A^2+B^2+C^2)\cdot\delta(\tau) + AB\cdot\left[e^{i\Delta\phi_{ab}}\cdot\delta(\tau+\tau_{ab}) + e^{-i\Delta\phi_{ab}}\cdot\delta(\tau-\tau_{ab})\right] + ... \\ &\quad AC\cdot\left[e^{i\Delta\phi_{ac}}\cdot\delta(\tau+\tau_{ac}) + e^{-i\Delta\phi_{ac}}\cdot\delta(\tau-\tau_{ac})\right] + BC\cdot\left[e^{i\Delta\phi_{bc}}\cdot\delta(\tau+\tau_{bc}) + e^{-i\Delta\phi_{bc}}\cdot\delta(\tau-\tau_{bc})\right], \end{aligned} \quad (3\text{-}43)$$

Fig. 3-13(c) represents the same pixel location after Fourier transform, where every peak corresponds to each mode beating. Therefore, the amplitude, phase, and group delay of the modes can be resolved from the peak strength, phase and locations. Using this method, each mode profile can be extracted from the series of images by performing the Fourier transform on each pixel as shown in the inset of Fig. 3-13(c).

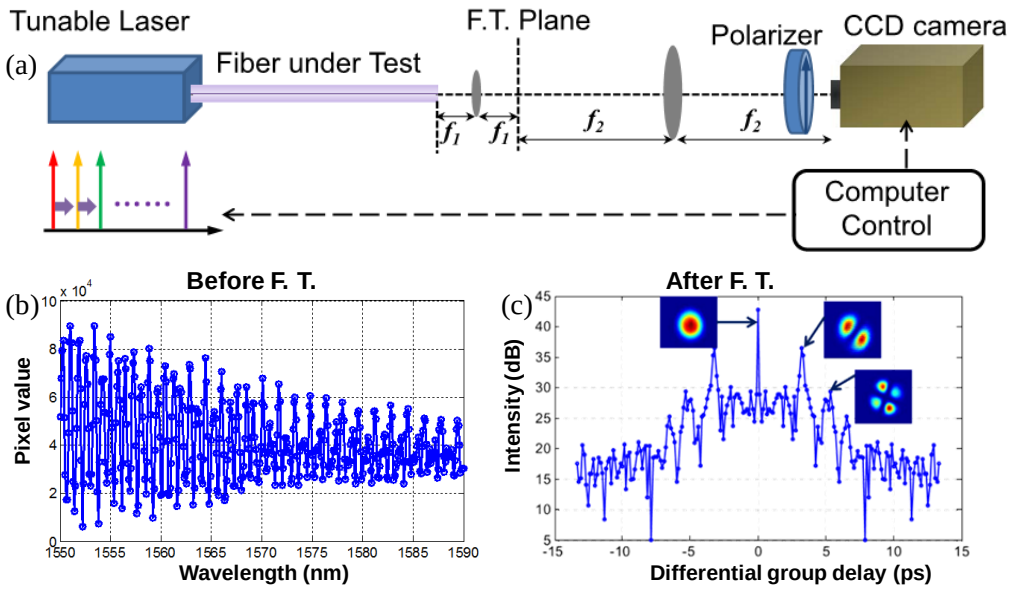

Figure 3-13. (a) Schematic of S^2 imaging setup using a tunable laser and a CCD camera; (b) wavelength-scanning results of the multi-path interference pattern for one pixel of the CCD camera and (c) the result of intensity vs. differential group delay (DGD) after taking Fourier transform of (b). Inset of (c) shows the resolved LP modes after picking the information for every pixel at the corresponding DGDs of different modes and mapping them together.

All the supermodes of the 3-core fiber were obtained using the S^2 imaging method. One difficulty of the experiment is that the mode identification became very complicated due to the large number of fiber modes. Since every peak is the result of the beating of any two modes, the number of the mode-beating peaks scales quadratically with the number of modes. In this experiment, the problem was solved by using intentional offset launching to excite only one dominant mode with a few other modes for each wavelength sweep. Then, multiple excitations were required in order to resolve different modes. S^2 imaging also suffers from the inherent inability to separate degenerate modes, which share same group delays. However, due to the hexagonal shape of the cores in this 3-core fiber, the degenerate modes actually have a subtle

difference in group delay, making it possible to reconstruct each of them separately. Therefore, a total of 9 modes supported by the 3-core fiber were successfully reconstructed in both amplitude and phase, as shown in Fig. 3-14. The first three images are of LP_{01} supermodes, in which the field is slightly better resolved than in those of the LP_{11} supermodes. This is because significantly less power is coupled into the higher-order modes during center or offset excitation. The degenerate higher-order mode images are slightly blurry because their group delay difference is too small to allow them to be clearly differentiated. Nevertheless, the resolved fiber modes are in good agreement with the simulations shown in Fig. 3-14.

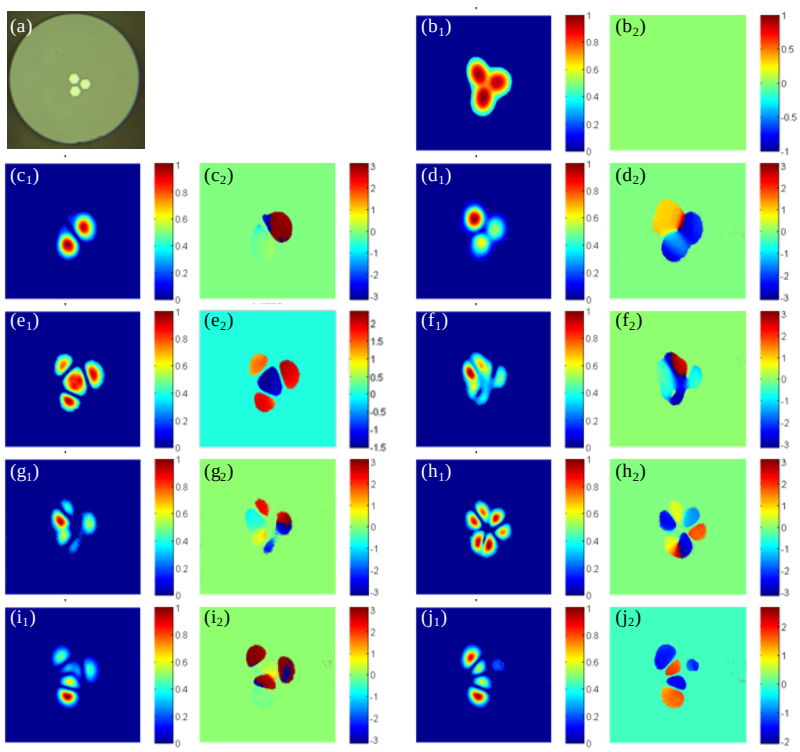

Figure 3-14. (a) Cross-sectional view of the fabricated coupled-3-core fiber and (b-j) resolved supermodes of the fabricated coupled-3-core fiber shown in amplitude (x1) and phase (x2): (b) the fundamental LP_{01} supermode; (c, d) the degenerate pair of LP_{01} supermodes; (d) the fundamental LP_{11} supermode; (e, f) the first degenerate pair of LP_{11} supermodes; (g) the fourth LP_{11} supermode; (h, i) the second degenerate pair of LP_{11} supermodes.

CHAPTER 4 FEW-MODE PASSIVE OPTICAL NETWORKS

4.1 Introduction and Background

Time-division multiplexed (TDM) passive optical networks (PON) (e.g. GPON and EPON) are currently being widely deployed worldwide to satisfy the traffic demand in access networks. There is an increasing interest in PONs towards longer reach and larger splitting ratios to increase coverage and reduce overall cost. To do so, the power budget needs to be improved using innovative solutions. In most practical systems, a large power loss is incurred at collector locations by optical splitters that combine/split signals from/to the optical network units (ONUs). The downstream power splitting enables the essential one-to-many function from the optical line terminal (OLT) to ONUs and thus the splitting losses are unavoidable, but the excess upstream combining loss incurred in one-to-one communication from an ONU to the OLT is neither necessary nor fundamental and can be reduced in a variety of ways. There has been much effort aiming to eliminate the upstream combining loss, such as the use of a multi-mode combiner (MC) [126, 127]. The MC solution, however, requires multiple feeder fibers as shown in Fig. 4-1(a), which defeats one of the main purposes of fan-out improvement using splitters, that is, the reduction of the total amount of fibers needed in the network.

Recently, we proposed the use of space-division multiplexing (SDM) in a single few-mode fiber (FMF), acting as the feeder fiber in the optical distribution network (ODN), to effectively eliminate the upstream combining loss [128]. Moreover, this concept has been realized by using a commercial GPON system carrying live Ethernet traffic, achieving the first reported few-mode GPON [129, 130]. In this paper, we discuss different approaches to achieve

TDM few-mode PON, including the previously demonstrated low-crosstalk method and the low modal group delay (DMGD) method. The experimental setup and results of the few-mode GPON system are presented in more depth and details. Future work in this area such as mode-division multiplexing for PON is also discussed.

It should be noted that the application of FMF to access is not simply the transplantation of a long distance optical transport technique to access. Instead, it focuses on the unique requirements of optical access. While in optical transport the usual goal is to maximize spectral efficiency and total information throughput, in access it is most important to maximize the loss budget and split ratio, and reduce cost per subscriber. While throughput is important, it must be balanced against other factors. This brings us to different design strategies which leverage better fiber designs to enable simple direct detection schemes.

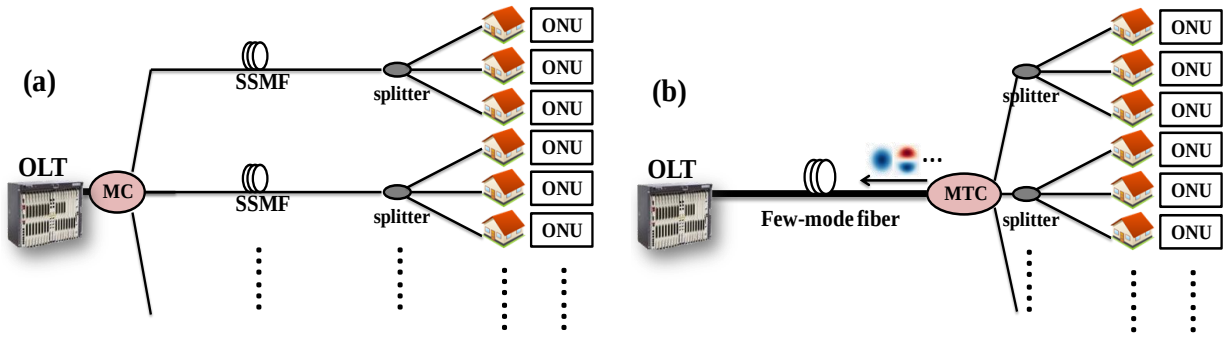

Figure 4-1. PON architectures with low upstream loss using (a) multiple feeder fibers and a multimode combiner (MC); and (b) a single FMF with a mode transforming coupler (MTC).

4.2 Principle of Few-Mode PON

Figure 4-1(b) shows the proposed few-mode PON architecture which consists of a FMF and a mode-transforming coupler (MTC) in place of a traditional single-mode combiner/splitter

in standard PON systems. The MTC couples multiple single-mode fibers (SMFs) into the FMF. The MTC can combine signals from feeder fibers with negligible losses [95-97, 131] and thus is able to increase the fan-out number by a factor equal to the number of the spatial modes, including the degenerate modes. The critical challenge is from inter-mode crosstalk generated in the MTC as well as along the FMF, and the modal group delay (DMGD). In long-haul SDM transmission, inter-mode crosstalk and DMGD are equalized by using sophisticated joint coherent detection of all the modes, followed by multiple-input-multiple-output (MIMO) signal processing [88, 132]. For PON applications, coherent detection and MIMO are undesirable due to their high complexity and cost. Fortunately, one can utilize the unique feature of TDM-PON that only one ONU is active upstream at any given time and preserve direct detection in the PON architecture. Given $I_s(t)$ is the only signal transmitted at a time, the detected signal hence can be written as below

$$I_{\text{det}}(t) = a \cdot I_s(t) + \sum_i b_i \cdot I_s(t-\tau_i) + \sum_j c_j \cdot I_s(t-\tau_j) + \cdots, \quad \tau_{i,j} \le \tau_{MGD} \qquad (4\text{-}1)$$

where the first term is the signal carried by the desired mode while the other terms represents crosstalk from the other modes generated at different locations. Eq. (4-1) reveals two different approaches for successful TDM-PON operation. One is to reduce DMGD to be much less than a symbol period and thus the crosstalk becomes part of the signal. The other approach is to suppress the modal crosstalk to be low enough that DMGD would no longer be an issue. For the first approach, one needs to design FMF with very low DMGD or apply the DMGD-compensation method using FMFs of positive and negative DMGDs [93, 94]. For the second approach of crosstalk suppression, note that direct detection of all the FMF modes actually relaxes the requirement for crosstalk as mode crosstalk becomes incoherent in intensity detection

due to mode orthogonality. Here we first demonstrate the low-crosstalk approach combined with the low-DMGD approach for the real experiment on a 20km 3-mode fiber. Because among the three modes, the DMGD between the two degenerate LP11 modes is close to zero while between the LP01 and LP11 modes modal crosstalk of the FMF can be low but the DMGD is usually large. Therefore the problem is reduced to suppress the crosstalk between the LP01 and LP11 modes for both the MTC and along the FMF. In Section 4.5 we present simulation results to introduce the possibility of using the low-DMGD approach for 10 Gb/s 10-mode transmission without the need of suppressing mode crosstalk.

4.3 Low-Crosstalk Few-Mode PON

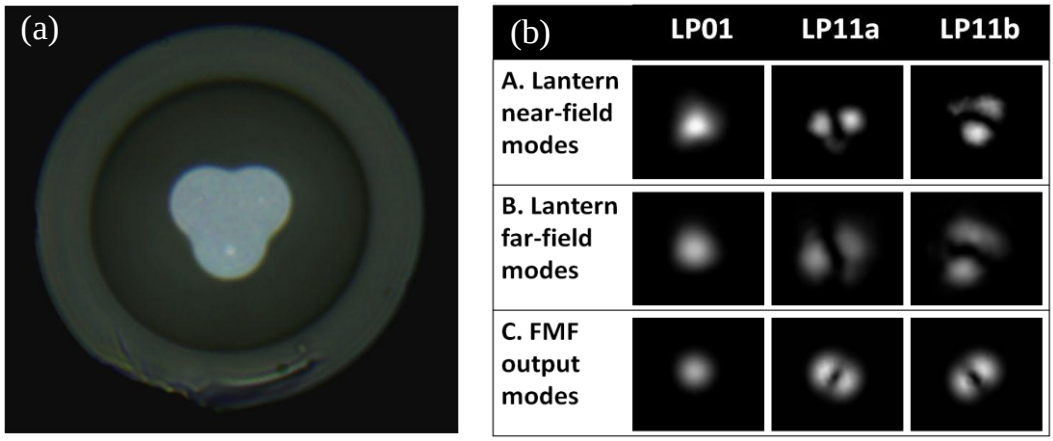

Figure 4-2. (a) The cross-section of the mode-selective lantern output; (b) measured LP01, LP11a & LP11b intensity patterns at the lantern near-field, far-field and the end of lantern-to-20km FMF.

In order to demonstrate the low-crosstalk few-mode PON, we first establish the low-loss and low-crosstalk few-mode segment of the optical distribution network (ODN) consisting of the transmission FMF and the MTC. The implementation of the low-loss and low-crosstalk MTC

can be done in several ways. Generally speaking, all low-loss mode-division multiplexers that are mode-group selective is suitable for this application, including directional couplers [133], free-space phase-selective devices [134] and mode-group selective photonic lanterns [95, 131]. Here the MTC is a mode-selective photonic lantern which converts three single-mode inputs from SSMFs into the LP01, LP11a and LP11b modes of the FMF. The photonic lantern was fabricated by inserting three input fibers into a fluorine-doped capillary with an index difference of 4×10^{-3} and then tapering the entire structure adiabatically. Of the three input fibers, two of them are SMF-28 fibers with propagation constant matched to LP11 modes of the photonic lantern while the other has a slightly larger core of ~15μm and an index difference of 5×10^{-3} so that its propagation constant is matched to that of LP01 mode of the photonic lantern to achieve mode selectivity. The cross-section of the lantern output has a near-triangular core of a diameter of ~27μm as shown in Fig. 4-2(a). The FMF has a depressed cladding index profile that supports 3 modes, the fundamental LP01 mode and two degenerate LP11 modes, at 1310nm, the upstream wavelength of GPON. Additionally, the LP11 modes are near cut-off at 1550nm and thus become very lossy. The attenuations of the LP01 and LP11 modes at 1310nm are 0.33dB/km and 0.35dB/km respectively while at 1550nm the attenuation of the LP11 mode is 0.192dB/km, all comparable to those of SSMF. The FMF modes are about half sizes of the lantern modes. In order to reduce the coupling loss due to the mode-size mismatch, a lens combination was used for free-space lantern-to-FMF coupling. The near-field and far-field output mode intensity patterns of the photonic lantern and those at the end of the 20km FMF are shown in Fig. 4-2(b), demonstrating excellent mode selectivity. The insertion loss of the photonic lantern including the splice loss to the single-mode input fibers was 1.3dB, 0.8dB and 1.4dB for the LP01, LP11a and

LP11b mode, respectively, representing an average 3.5 dB improvement in the combining loss compared to conventional single-mode splitters. The coupling loss from the lantern output to the FMF, mainly due to mode mismatch between the lantern and the FMF as well as the scattering, was estimated to be 2.4dB for LP01 and 6.7dB, 6.2dB for LP11a&b. Those coupling losses can be substantially decreased by using a photonic lantern better matched to the FMF [128]. The crosstalk of the entire few-mode segment shown in Fig. 4-3(a) was measured by the impulse-response method. In order to do so, a narrow pulse was sent into each input port of the photonic lantern, transmitted through 20km FMF and received by a high-speed free-space-coupled photo-detector. The crosstalk levels were optimized to be less than 9dB for all the three inputs, as shown in Fig. 4-3(b). The DMGD between the LP01 and LP11 modes was characterized at the same time to be ~0.6ns over 20km FMF.

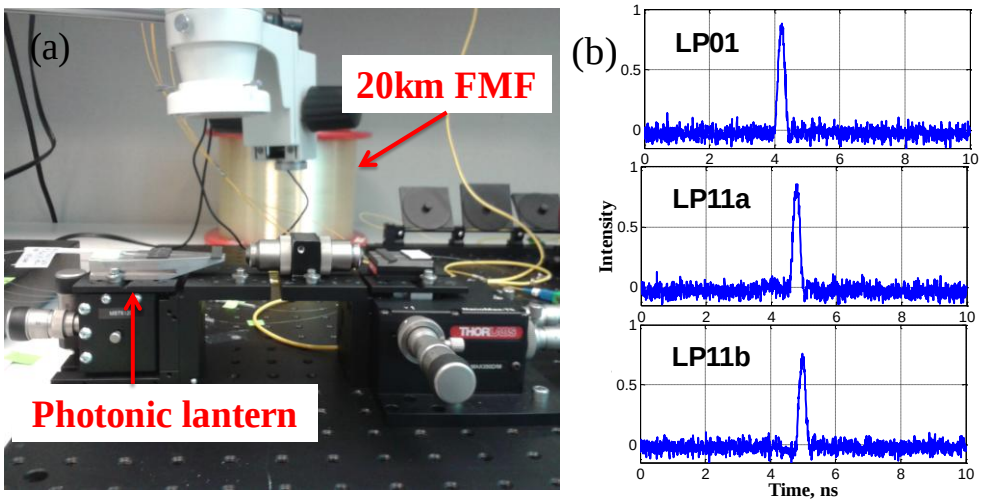

Figure 4-3. (a) Picture of the few-mode segment of the ODN; (b) measured LP01, LP11a and LP11b impulse responses of the few-mode ODN segment.

4.4 Demonstration of the First Few-Mode GPON System

We then demonstrate the world's first few-mode GPON system by seamlessly integrating the few-mode ODN in a commercial GPON system with one Huawei OLT and four Echolife ONUs, as shown in Fig. 4-4. To enable the integration between the few-mode ODN and the otherwise SSMF-based PON optical components, a novel reach extender was added before the OLT to separately detect the upstream data from the FMF in burst mode and to regenerate the data onto a single-mode fiber because the current OLT SFP optical module only accepts single-mode input. Two stages of splitters were created to imitate a real PON network. The WDM filters separate 1310nm and 1490 nm light for the upstream and downstream flow. Since our focus is combining loss for upstream traffic, downstream signals were transmitted over SMF ODN. Modification of the OLT transmitter is required if downstream signals needs to be transported in the few-mode ODN. For upstream, data streams from different ONUs were coupled into the FMF by the 3-mode photonic lantern and transmitted over 20km FMF link. The variable attenuators before the photonic lantern were used to equalize and monitor the power levels. The reach extender regenerates and interleaves upstream and downstream signals, and finally connects to the OLT. Gigabit/s real traffic was monitored by an Ethernet tester.

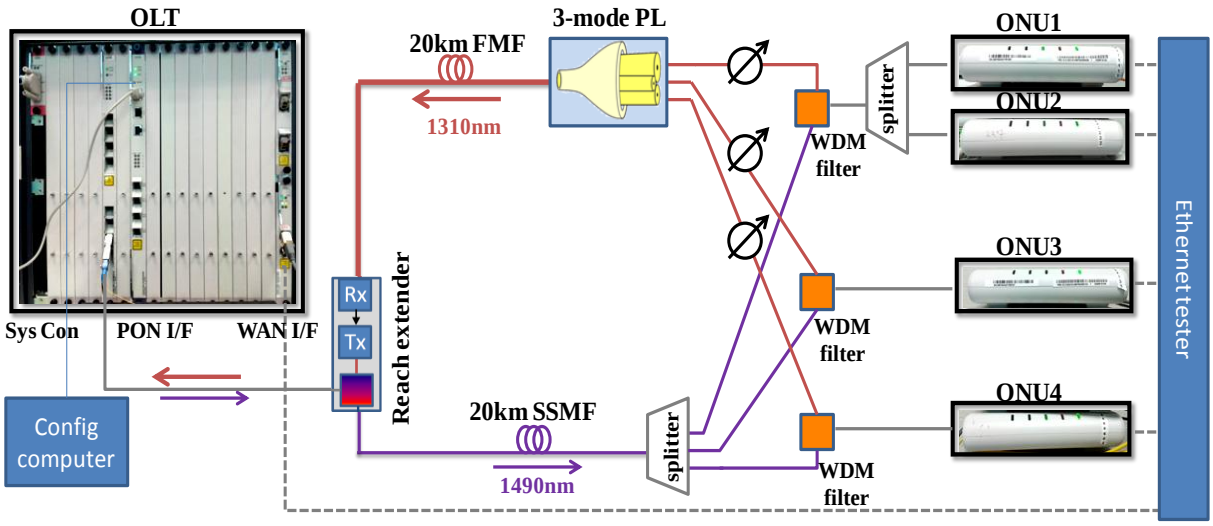

Figure 4-4. Schematic of a few-mode GPON system using a 20km FMF and a mode-selective lantern for upstream transmission. OLT: commercial optical line terminal; ONUs: commercial optical network units.

The upstream transport performance through the few-mode ODN was characterized via bit-error-rate (BER) measurements at 1.25 Gb/s using a 1.3μm DFB laser and an APD ROSA without limiting amplification and clock data recovery. The transmitter output was switched to the three photonic lantern input ports one at a time to test each mode. The BER results are plotted in Fig. 4-5(a). The back-to-back (B2B) receiver sensitivity at a BER of 10-3 is -30 dBm. The B2B eye diagram and those after 20km transmission for each mode are shown as Fig. 4-5(b). The eye diagrams of LP01 and B2B cases are almost identical. The LP11s have slightly degraded performance. Nevertheless, all the modes can achieve a BER of <10-9, which is good enough for successful commercial GPON operation. Compared to B2B, the LP11a and LP11b modes exhibit power penalties of 1.5 dB and 2.7 dB, respectively. We attribute these moderate implementation penalties to imperfect matching between the LP11 modes and the free-space-coupled photo-detector area, which was matched to SSMF inputs. This penalty is expected to be eliminated

using a properly designed photo-detector. The error-free performance of the few-mode ODN allowed us to carry live Ethernet traffic in the few-mode GPON system using a commercial Ethernet tester. Long-term measurement was done with no packet loss observed over tens of millions of Ethernet packets received.

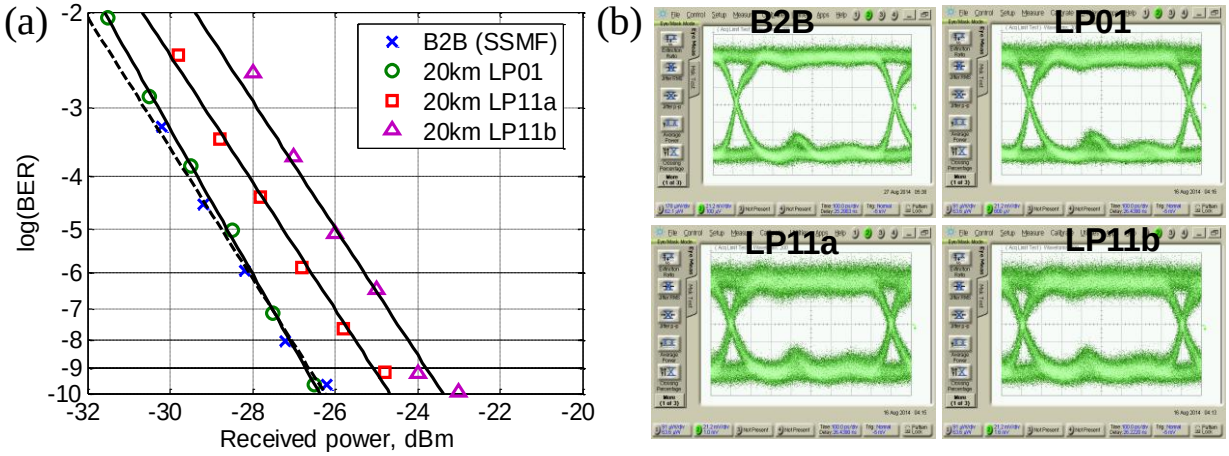

Figure 4-5. (a) BER measurements of the few-mode ODN segment; (b) eye diagrams of the cases of B2B (with SSMF), 20km LP01, LP11a and LP11b transmission.

4.5 Alternatives and Discussion

Even though the low-crosstalk approach has been demonstrated successfully for three-mode transmission, crosstalk suppression for both the MTC and the FMF is still difficult in general, especially when it scales to larger number of modes. On the other hand, the alternative approach only requires the FMF to have low-DMGD between all the modes. As a result the requirement for MTC relaxes to be simply low insertion loss, which can be easily achieved [135]. In this section we consider the alternative low-DMGD approach when the number of modes scale to 10 (i.e., LP01, LP02 and degenerate LP11s/ LP21s/ LP12s/ LP31s modes). Based on

previous works for fewer modes [91, 136], trench-assisted graded-index profile has been found to be useful for DMGD optimization and hence will be applied here as well. The inset of Fig. 4-6 shows the graded-index profile, with a cladding trench for low DMGD, given by

$$n(r)=\begin{cases} n(0)\cdot[1-\Delta_1\cdot(r/a_1)^{\alpha_n}]^{1/2}, & (r\le|a_1|) \\ n_{cl}, & (|a_1|<r\le|a_2|) \\ n_{cl}\cdot(1-\Delta_2), & (|a_2|<r\le|a_3|) \\ n_{cl}, & (r>|a_3|) \end{cases} \qquad (4\text{-}2)$$

where α_n is the power coefficient of the GI profile. With fiber parameters chosen as $a_1=15.32\ \mu m,\ a_2=17.2\ \mu m,\ a_2=22.12\ \mu m,\ \Delta_1=0.4375\%$ and $\Delta_2=0.33\%$, the differential modal group delay of a 10-mode GI FMF (referenced to the average modal group delay) at 1310 nm as a function of the power coefficient is shown in Fig. 4-6. The maximum DMGD (between the fastest and slowest mode) is less than 7 ps/km, achieved near $\alpha_n=2.0$. This fiber design should be able to support few-mode transmission of reach up to 20 km for standard PON (data rate of 2Gb/s) in presence of mode crosstalk. The high sensitivity of DMGD to the power coefficient and other fiber parameters should be studied and improved, possibly using different fiber structures.

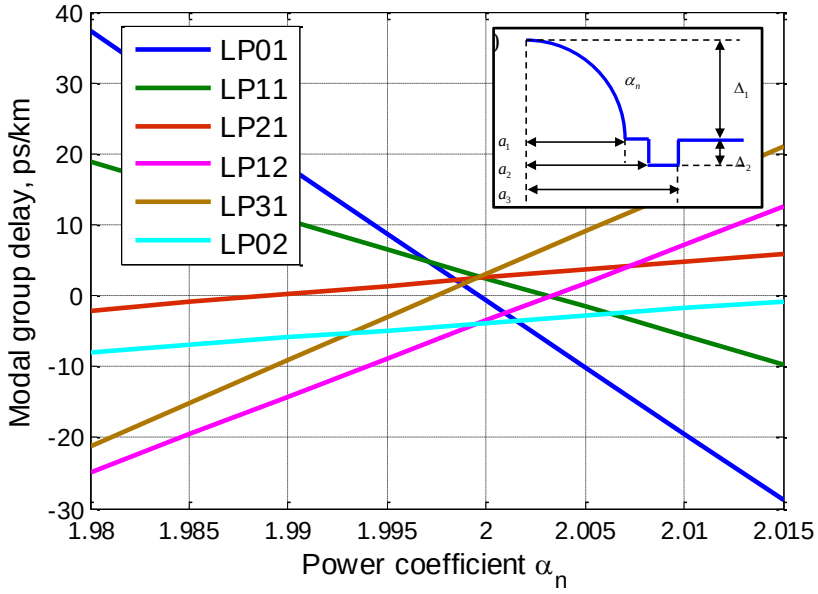

Figure 4-6. Simulation results of modal group delay for 10-mode fiber design of trench-assisted graded-index profile. Inset: the FMF index profile with parameters indicated.

4.6 Scaling to 5-mode PON

Scaling to larger number of modes, which means a larger splitting ratio, is seen as a key requirement for the potential commercialization of the FM PON system. Therefore, we extend the initial 3-mode FM PON to 5-mode FM PON with a record 4dB net gain in power budget, integrated with commercial GPON. This is also the first FM PON with photonic lantern and FMF being fusion spliced together, giving a significant step towards further integration.

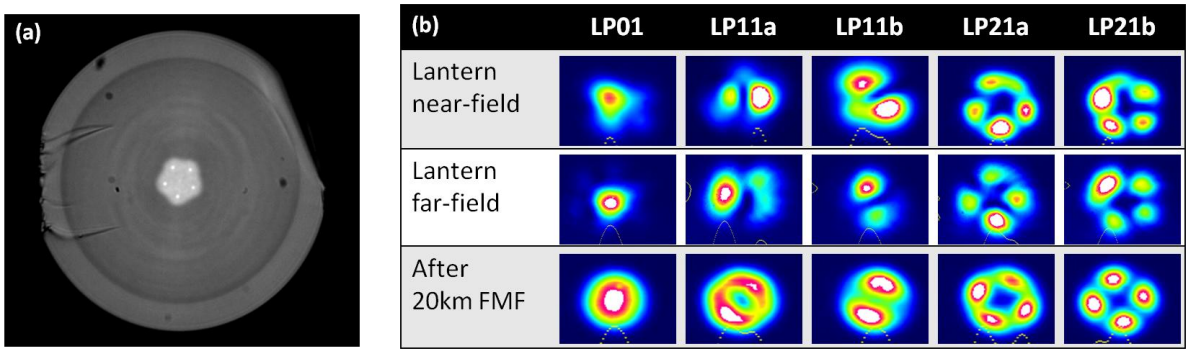

Figure 4-7. (a) The cross-sectional view of the photonic lantern output. (b) Intensity patterns of 5 modes for the near-field and far-field output of the photonic lantern and after 20km propagation via the FMF at 1.3μm.

The key to realizing direct detection without any MIMO processing is to either have very low crosstalk or very small differential group delay between the mode groups [129]. Notice that within a mode group, modes usually have strong crosstalk in between but the differential group delay is negligible. Here we choose the low crosstalk approach and hence have a critical crosstalk requirement for both the photonic lantern and the FMF. The cross-section of the low-loss mode-selective photonic lantern [137] used for this work is shown in Fig. 4-7(a). In order to enable the fusion splicing, the photonic lantern was fabricated by inserting different input fibers into a low-index capillary of a customized size so that it can be adiabatically tapered to the typical diameter of ~125μm. And each input fiber of the photonic lantern was designed to have a propagation constant matched to the desired mode and hence achieved good mode selectivity shown in Fig. 4-7(b). The loss of the photonic lantern itself is < 1dB. The photonic lantern was fusion spliced to a 20km low-crosstalk FMF to improve both the stability and simplicity of the setup. The FMF supports up to the LP21 modes at both the upstream and downstream wavelengths. The index profile of the FMF is shown in Fig. 4-8, allowing large effective index

difference between mode groups for reduced mode crosstalk. Mode patterns have been captured at 1.3μm right after the photonic lantern and after propagation via the 20km FMF, shown in Fig. 4-7(b). The entire link losses for LP01, LP11a&b and LP21a&b at 1.3μm are 10.1dB, 12.5dB, 9.5dB, 10.1dB and 10.1dB respectively. The attenuation of FMF is around 0.4dB/km even for the highest-order mode. On average, the use of the PL increases the system power budget by at least 4 dB. Extra losses are attributed to the coupling losses from the photonic lantern to the FMF because of mode mismatch and the splicing losses of SSMFs to the photonic lantern's 5 input fibers of different core sizes.

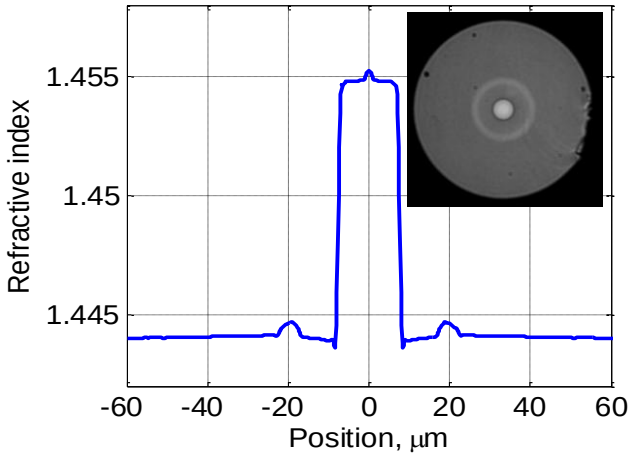

Figure 4-8. Index profile of the few-mode fiber. Inset: cross-sectional view.

The link crosstalk is characterized by the impulse-response method where a narrow pulse is sent into the input port of each mode, transmitted over the photonic lantern and 20km FMF, and received by a high-speed free-space-coupled photo-detector. The crosstalk levels are below 6 dB as shown in Fig. 4-9(a) where it also shows that the differential group delays of the LP11 and LP21 mode are 75ns and 165ns with respect to the LP01 mode. The small peaks at the delays of 206ns and 255ns are the higher-order modes close to cut-off and can be easily suppressed by

tight bends. The bit-error-rate (BER) performance, shown in Fig. 4-10, was measured by using a 1.3μm DFB laser and the same free-space-coupled detector without amplification at 1 Gb/s. Eye diagrams are plotted in Fig. 4-10(b) where crosstalk displays as double eyelids. Because the direct detection of the orthogonal modes adds the intensity of the different modes incoherently, it actually eases the crosstalk requirement largely [130]. Therefore, all modes can achieve a BER of $<10^{-9}$. Power penalties compared to back-to-back (B2B) were due to residual mode crosstalk and imperfect matching between the FMF modes and photo-detector area, which was only intended for single-mode inputs.

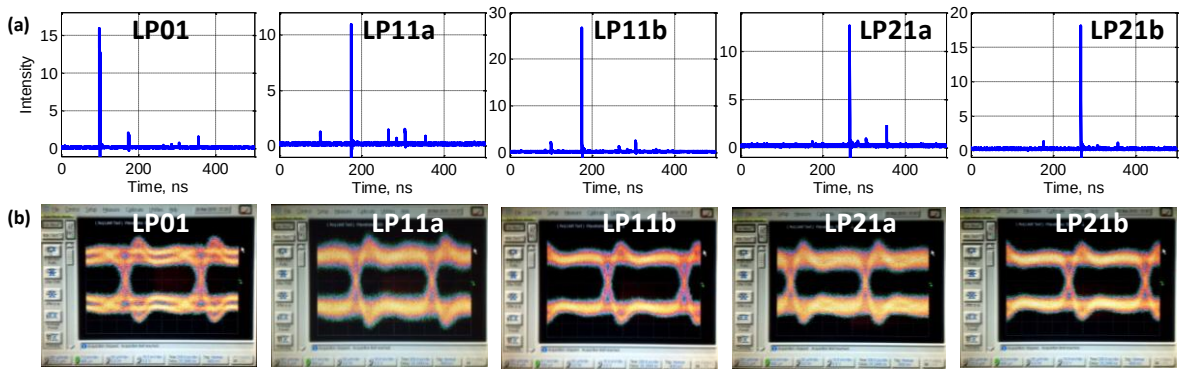

Figure 4-9. Impulse measurements and (b) eye diagrams of the 5-mode optical link composed of the photonic lantern spliced with 20km FMF spool.

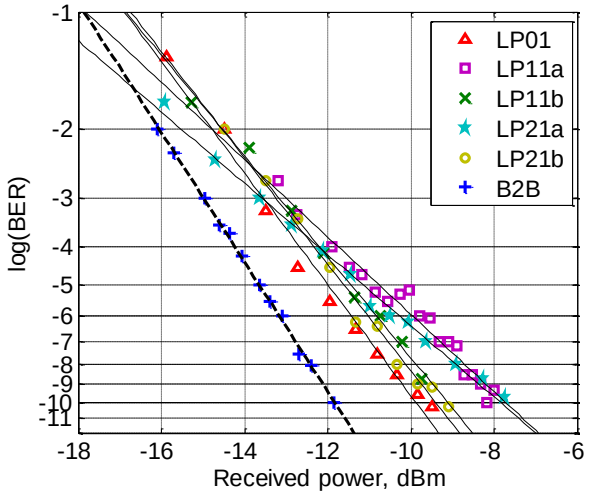

Figure 4-10. BER measurements of the 5-mode optical link

The FMF link was integrated into the optical distribution network of a commercial GPON system as shown in Fig. 4-11. The GPON equipment includes one Huawei optical line terminal (OLT) and eight Echolife optical networking units (ONUs). Two stages of splitting at the ONU side were created to emulate a real PON network. Since our focus is to eliminate the upstream combining loss, downstream transport at 1490nm was separated by WDM filters and was still transmitted via 20km SSMF and split into ONUs by a traditional single-mode splitter. For upstream traffic, data streams from commercial ONUs were sent into each input port of the photonic lantern, converted into different modes and propagated along the FMF for 20km. Because the commercial OLT SFP optical module only accepts single-mode input, a reach extender was added to detect signals from the FMF in burst mode and regenerate the data onto a SSMF before going into the OLT. In addition, the reach extender contains a WDM filter which interleaves upstream and downstream signals. Packet loss of bidirectional traffic was monitored using the Ethernet tester. Transmission on all 5 modes without any packet loss was successfully demonstrated.

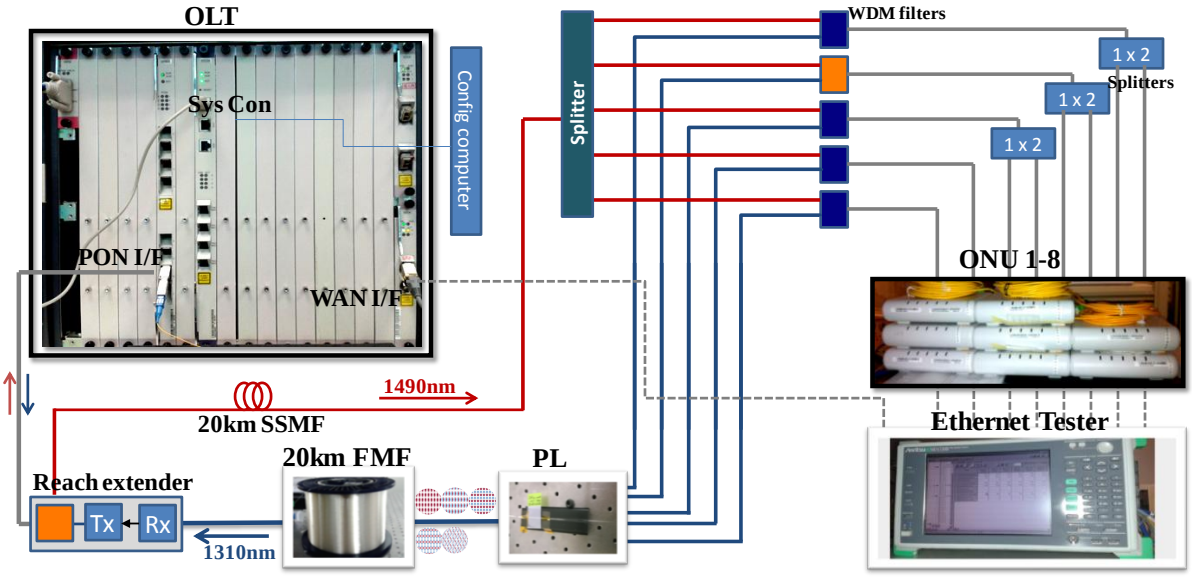

Figure 4-11. Schematic of 5-mode GPON system using the PL spliced to 20km FMF for upstream transmission with commercial Huawei OLT and ONUs. OLT: optical line terminal; ONU: optical networking unit; PL: photonic lantern. Red line represents 1490nm downstream transport; blue line stands for 1310nm downstream transport; and gray line corresponds to: bidirectional transmission.

As a short summary of the section 4.6, we demonstrate the first 5-mode PON which achieved to save an upstream combining loss of at least 4dB. Link crosstalk as low as <6dB has been obtained for the 5 modes with a mode-selective lantern fusion spliced to a 20km FMF. Therefore a BER of $<10^{-9}$ is realized for all the 5 modes and thus enables integration with commercial GPON system. High-density FMF technique realized in access networks may open up the opportunities for future MDM research, development and commercialization.

CHAPTER 5 SUMMARY

This dissertation focuses on two critical requirements of optical fibers for SDM transmission: 1) high mode density and 2) either low modal crosstalk or low DMGD. Because SDM system is only beneficial once integrated, the efforts are not only put on the fiber design and characterization, but also on how to implement such fibers to SDM transmission and networking.

In Chapter 1, a FMMCF has been designed and fabricated to increase the mode density for the first time. The fiber consists of 7 cores each supporting 3 spatial modes per polarization. Low core-to-core crosstalk levels have been achieved for both LP01 and LP11 modes. Data transmission in LP01 / LP11 mode over 1km of FMMCF has been demonstrated with negligible penalty. A SDM transmision of 42 spatial channel has been achieved using this novel fiber as a collaborated work, enabling an aggregate transmission capacity of 255 Tbit/s.

In Chapter 2, we have proposed a coupled multi-core fiber (CMCF) design for SDM transmission. The new design exploits the coupling between the cores of a conventional multi-core fiber instead of avoiding it. This design has advantageous over the conventional multi-core fiber in terms of higher mode density and larger mode effective area. The applications of CMCFs can be either short-distance transmission with low crosstalk or long-haul transmission with low DMGD. As an example, a DMGD design of less than 60ps/km throughout the C band has been achieved for a coupled-3-core fiber.

In addition, we have investigated higher-order supermodes in the latter part of this chapter, based on the weakly-coupled assumption. The angle-dependent couplings are able to strongly affect the modal fields of the higher-order supermodes in different waveguide array

configurations. Therefore higher-order supermodes have been analyzed for the linear arrays, square lattices and ring arrays. General solutions of higher-order supermodes in those structures of arbitrary sizes are provided. In addition, an experimental observation of higher-order supermodes has been achieved for the first time in a coupled few-mode 3-core fiber. This study enriches the concept of supermodes in coupled multi-core waveguides, which may have potential applications not only in MDM systems, but also in other areas related to waveguide optics, such as optical phased arrays, beam combining and fiber imaging systems.

In Chapter 3, we demonstrate, for the first time, a few-mode PON that utilizes mode multiplexing to eliminate the combining losses for upstream traffic. Seamless integration between a few-mode ODN and a commercial GPON system carrying live Ethernet traffic is achieved without any packet loss. Simulation results also indicated the possibility of using the alternative low-DMGD approach. The beneficial combination of SDM and PON may open exciting opportunities for future research, development, and commercialization. As an important extended work, we then scaled the few-mode PON to 5 modes, which achieved to save an upstream combining loss of at least 4dB. Link crosstalk as low as <6dB has been obtained for the 5 modes with a mode-selective lantern fusion spliced to a 20km FMF. Therefore error-free performance has been realized for all the 5 modes and thus enables integration with commercial GPON system. High-density FMF technique realized in access networks may open up the opportunities for future MDM research, development and commercialization.

APPENDIX:
DERIVATIONS

In order to solve the higher-order supermodes for ring-array structure, diagonalization of the coupled matrix $\boldsymbol{M}$ is the key. It takes two steps as follows. Because each sub-matrix of $\boldsymbol{M}$ has the similar form as the coupled matrix of LP_{01} supermodes, the first step is to utilize the previous solution and diagonalize the sub-matrixes all together. In order to do so, a rank-2N modal matrix is defined as

$$\boldsymbol{P}=\begin{bmatrix}\boldsymbol{Q} & \boldsymbol{0}_N\\ \boldsymbol{0}_N & \boldsymbol{Q}\end{bmatrix}, \qquad \text{(A-1)}$$

where $\boldsymbol{0}_N$ is a N-by-N null matrix and $(\boldsymbol{Q})_{lm}=\frac{1}{\sqrt{N}}e^{-i\frac{2\pi l}{N}\cdot m}$ according to Eq. (3-34). $\boldsymbol{P}$ then transforms $\boldsymbol{M}$ into a block matrix composed of diagonal sub-matrixes as below

$$\boldsymbol{D}=\boldsymbol{P}^{-1}\boldsymbol{M}\boldsymbol{P}=\begin{bmatrix}\boldsymbol{Q}^{-1}\boldsymbol{M}_{tt}\boldsymbol{Q} & \boldsymbol{Q}^{-1}\boldsymbol{M}_{tn}\boldsymbol{Q}\\ \boldsymbol{Q}^{-1}\boldsymbol{M}_{nt}\boldsymbol{Q} & \boldsymbol{Q}^{-1}\boldsymbol{M}_{nn}\boldsymbol{Q}\end{bmatrix}=\begin{bmatrix}\boldsymbol{D}_{tt} & \boldsymbol{D}_{tn}\\ \boldsymbol{D}_{nt} & \boldsymbol{D}_{nn}\end{bmatrix}, \qquad \text{(A-2)}$$

where all the diagonal elements can be calculated

$$(\boldsymbol{D}_{tt})_{l,l}=2\kappa_{t_1,t_2}\cdot\cos\left(\frac{2\pi l}{N}\right), \qquad \text{(A-3a)}$$

$$(\boldsymbol{D}_{tn})_{l,l}=2i\kappa_{t_1,n_2}\cdot\sin\left(\frac{2\pi l}{N}\right), \qquad \text{(A-3b)}$$

$$(\boldsymbol{D}_{nt})_{l,l}=-2i\kappa_{t_1,n_2}\cdot\sin\left(\frac{2\pi l}{N}\right), \qquad \text{(A-3c)}$$

$$(\boldsymbol{D}_{nn})_{l,l}=2\kappa_{n_1,n_2}\cdot\cos\left(\frac{2\pi l}{N}\right),\ l=1,2\cdots N. \qquad \text{(A-3d)}$$

$\boldsymbol{D}$ is a block matrix composed of 4 diagonal N-by-N sub-matrixes, which are commutable with each other. Notice that if $(\boldsymbol{D}_{tn})_{l=l_0}=(\boldsymbol{D}_{nt})_{l=l_0}=0$, then $(\boldsymbol{D}_{tt})_{l=l_0}=2\kappa_{t_1,t_2}\cdot\cos\left(\frac{2\pi l_0}{N}\right)$ and $(\boldsymbol{D}_{nn})_{l=l_0}=2\kappa_{n_1,n_2}\cdot\cos\left(\frac{2\pi l_0}{N}\right)$ are eigenvalues already. In addition, a function of a diagonal matrix

is still a diagonal matrix, whose elements are the same function of the original matrix elements, i.e., $f(D)_{lm} = f\left((D)_{ml}\right)$[112]. With these properties, the second step of diagonalization can be operated on $\boldsymbol{D}$ similar to a simple 2-by-2 matrix of $\begin{bmatrix} a & b \\ c & d \end{bmatrix}$

$$\boldsymbol{\Lambda} = \boldsymbol{R}^{-1}\boldsymbol{D}\boldsymbol{R}. \qquad \text{(A-4)}$$

The eigenvalue matrix is solved as

$$\boldsymbol{\Lambda} = \begin{bmatrix} \frac{1}{2}(\boldsymbol{D}_{tt} + \boldsymbol{D}_{nn} + \boldsymbol{D}_R) & \boldsymbol{0}_N \\ \boldsymbol{0}_N & \frac{1}{2}(\boldsymbol{D}_{tt} + \boldsymbol{D}_{nn} - \boldsymbol{D}_R) \end{bmatrix} \qquad \text{(A-5)}$$

and the modal matrix is

$$\boldsymbol{R} = \begin{bmatrix} \boldsymbol{D}_{tt} - \boldsymbol{D}_{nn} + \boldsymbol{D}_R & \boldsymbol{D}_{tt} - \boldsymbol{D}_{nn} - \boldsymbol{D}_R \\ 2\boldsymbol{D}_{nt} & 2\boldsymbol{D}_{nt} \end{bmatrix}, \qquad \text{(A-6)}$$

in which $\boldsymbol{D}_R = \sqrt{(\boldsymbol{D}_{tt} - \boldsymbol{D}_{nn})^2 + 4\boldsymbol{D}_{tn}\boldsymbol{D}_{nt}}$ when $\left(\boldsymbol{D}_{tn}\right)_{l,l} \neq 0$. Therefore the higher-order supermodes are the row vectors of the matrix $\boldsymbol{R}^{-1}\boldsymbol{P}^{-1}$ where $\boldsymbol{P}^{-1} = \boldsymbol{P}^* = \begin{bmatrix} \boldsymbol{Q}^* & \boldsymbol{0}_N \\ \boldsymbol{0}_N & \boldsymbol{Q}^* \end{bmatrix}$ and $\boldsymbol{R}^{-1} = \begin{bmatrix} 2\boldsymbol{D}_{nt} & \boldsymbol{D}_R - (\boldsymbol{D}_{tt} - \boldsymbol{D}_{nn}) \\ -2\boldsymbol{D}_{nt} & \boldsymbol{D}_R + (\boldsymbol{D}_{tt} - \boldsymbol{D}_{nn}) \end{bmatrix}$.

LIST OF REFERENCES

1. T. Li, "The impact of optical amplifiers on long-distance lightwave telecommunications," Proceedings of the IEEE **81**, 1568-1579 (1993).

2. G. Li, "Recent advances in coherent optical communication," Adv. Opt. Photon. **1**, 279-307 (2009).

3. D. Boivin, M. Bigot-Astruc, M. Travagnin, and P. Sillard, "Weakly-coupled Few-mode Fibers for Single-mode and Mode-division-multiplexed Transmissions," in *Optical Fiber Communication Conference*(Optical Society of America, 2013), p. OTh3K. 6.

4. N. Hanzawa, K. Saitoh, T. Sakamoto, T. Matsui, S. Tomita, and M. Koshiba, "Demonstration of mode-division multiplexing transmission over 10 km two-mode fiber with mode coupler," in *Optical Fiber Communication Conference and Exposition (OFC/NFOEC), 2011 and the National Fiber Optic Engineers Conference*(2011), pp. 1-3.

5. E. Ip, N. Bai, Y.-K. Huang, E. Mateo, F. Yaman, S. Bickham, H.-Y. Tam, C. Lu, M.-J. Li, S. Ten, A. P. T. Lau, V. Tse, G.-D. Peng, C. Montero, X. Prieto, and G. Li, "88x3x112-Gb/s WDM Transmission over 50-km of Three-Mode Fiber with Inline Multimode Fiber Amplifier," in *37th European Conference and Exposition on Optical Communications*(Optical Society of America, Geneva, 2011), p. Th.13.C.12.

6. E. Ip, N. Bai, Y.-K. Huang, E. Mateo, F. Yaman, M.-J. Li, S. Bickham, S. Ten, Y. Luo, and G.-D. Peng, "6x6 MIMO transmission over 50+ 25+ 10 km heterogeneous spans of few-mode fiber with inline erbium-doped fiber amplifier," in *Optical Fiber Communication Conference*(Optical Society of America, 2012), p. OTu2C. 4.

7. E. Ip, M.-J. Li, Y.-K. Huang, A. Tanaka, E. Mateo, W. Wood, J. Hu, Y. Yano, and K. Koreshkov, "146λx6x19-Gbaud wavelength-and mode-division multiplexed transmission over 10x50-km spans of few-mode fiber with a gain-equalized few-mode EDFA," in *Optical Fiber Communication Conference*(Optical Society of America, 2013), p. PDP5A. 2.

8. C. Koebele, M. Salsi, L. Milord, R. Ryf, C. A. Bolle, P. Sillard, S. Bigo, and G. Charlet, "40km Transmission of Five Mode Division Multiplexed Data Streams at 100Gb/s with low MIMO-DSP Complexity," in *37th European Conference and Exposition on Optical Communications*(Optical Society of America, Geneva, 2011), p. Th.13.C.13.

9. Y. Li, J. D. Ingham, V. Olle, G. Gorden, R. V. Penty, and I. White, "20 Gb/s Mode-Group-Division Multiplexing employing Hermite-Gaussian Launches over Worst-Case Multimode Fiber Links," in *Optical Fiber Communication Conference*(Optical Society of America, San Francisco, California, 2014), p. W2A.3.

10. S. Matsuo, Y. Sasaki, I. Ishida, K. Takenaga, K. Saitoh, and M. Koshiba, "Recent progress in multi core and few mode fiber," in *Optical Fiber Communication Conference*(Optical Society of America, 2013), p. OM3I. 3.

11. S. Randel, R. Ryf, A. Gnauck, M. A. Mestre, C. Schmidt, R. Essiambre, P. Winzer, R. Delbue, P. Pupalaikis, and A. Sureka, "Mode-multiplexed 6× 20-GBd QPSK transmission over 1200-km DGD-compensated few-mode fiber," in *National Fiber Optic Engineers Conference*(Optical Society of America, 2012), p. PDP5C. 5.

12. R. Ryf, "Space-division Multiplexed Transmission in Novel Few-mode Fibers," in *Frontiers in Optics*(Optical Society of America, 2012), p. FW2D. 1.

13. R. Ryf, N. K. Fontaine, H. Chen, B. Guan, S. Randel, N. Sauer, S. J. B. Yoo, A. Koonen, R. Delbue, P. Pupalaikis, A. Sureka, R. Shubochkin, Y. Sun, and R. Lingle, "23~Tbit/s Transmission over 17-km Conventional 50 um Graded-Index Multimode Fiber," in *Optical Fiber Communication Conference: Postdeadline Papers*(Optical Society of America, San Francisco, California, 2014), p. Th5B.1.

14. R. Ryf, N. K. Fontaine, M. A. Mestre, S. Randel, X. Palou, C. Bolle, A. H. Gnauck, S. Chandrasekhar, X. Liu, and B. Guan, "12 x 12 MIMO transmission over 130-km few-mode fiber," in *Frontiers in Optics*(Optical Society of America, 2012), p. FW6C. 4.

15. R. Ryf, M. A. Mestre, S. Randel, X. Palou, A. H. Gnauck, R. Delbue, P. Pupalaikis, A. Sureka, Y. Sun, and X. Jiang, "Combined SDM and WDM transmission over 700-km Few-Mode Fiber," in *Optical Fiber Communication Conference*(Optical Society of America, 2013), p. OW1I. 2.

16. R. Ryf, S. Randel, N. K. Fontaine, M. Montoliu, E. Burrows, S. Chandrasekhar, A. H. Gnauck, C. Xie, R.-J. Essiambre, and P. Winzer, "32-bit/s/Hz spectral efficiency WDM transmission over 177-km few-mode fiber," in *Optical Fiber Communication Conference*(Optical Society of America, 2013), p. PDP5A. 1.

17. R. Ryf, S. Randel, N. K. Fontaine, X. Palou, E. Burrows, S. Corteselli, S. Chandrasekhar, A. H. Gnauck, C. Xie, R. J. Essiambre, P. J. Winzer, R. Delbue, P. Pupalaikis, A. Sureka, Y. Sun, L. Gruner-Nielsen, R. V. Jensen, and R. Lingle, "708-km combined WDM/SDM transmission over few-mode fiber supporting 12 spatial and polarization modes," in *Optical Communication (ECOC 2013), 39th European Conference and Exhibition on*(2013), pp. 1-3.

18. R. Ryf, S. Randel, A. H. Gnauck, C. Bolle, R. Essiambre, P. J. Winzer, D. W. Peckham, A. McCurdy, and R. Lingle, "Space-division multiplexing over 10 km of three-mode fiber using coherent 6 x 6 MIMO processing," in *Optical Fiber Communication Conference and Exposition (OFC/NFOEC), 2011 and the National Fiber Optic Engineers Conference*(2011), pp. 1-3.

19. R. Ryf, S. Randel, M. A. Mestre, C. Schmidt, A. H. Gnauck, R.-J. Essiambre, P. Winzer, R. Delbue, P. Pupalaikis, and A. Sureka, "209-km single-span mode-and wavelength-multiplexed transmission over hybrid few-mode fiber," in *European Conference and Exhibition on Optical Communication*(Optical Society of America, 2012), p. Tu. 1. C. 1.

20. M. Salsi, C. Koebele, G. Charlet, and S. Bigo, "Mode division multiplexed transmission with a weakly-coupled few-mode fiber," in *Optical Fiber Communication Conference*(Optical Society of America, 2012), p. OTu2C. 5.

21. M. Salsi, C. Koebele, D. Sperti, P. Tran, P. Brindel, H. Mardoyan, S. Bigo, A. Boutin, F. Verluise, and P. Sillard, "Transmission at 2x100Gb/s, over two modes of 40km-long prototype few-mode fiber, using LCOS based mode multiplexer and demultiplexer," in *National Fiber Optic Engineers Conference*(Optical Society of America, 2011), p. PDPB9.

22. V. Sleiffer, Y. Jung, B. Inan, H. Chen, R. van Uden, M. Kuschnerov, D. van den Borne, S. Jansen, V. Veljanovski, and T. Koonen, "Mode-division-multiplexed 3x112-Gb/s DP-QPSK transmission over 80 km few-mode fiber with inline MM-EDFA and blind DSP," in *European Conference and Exhibition on Optical Communication*(Optical Society of America, 2012), p. Tu. 1. C. 2.

23. B. C. Thomsen, "MIMO enabled 40 Gb/s transmission using mode division multiplexing in multimode fiber," in *Optical Fiber Communication (OFC), collocated National Fiber Optic Engineers Conference, 2010 Conference on (OFC/NFOEC)*(2010), pp. 1-3.

24. R. van Uden, C. Okonkwo, H. Chen, H. de Waardt, and A. Koonen, "6×28GBaud 128-SP-QAM Transmission over 41.7 km Few-Mode Fiber with a 6×6 MIMO FDE," in *Optical Fiber Communication Conference*(Optical Society of America, San Francisco, California, 2014), p. W4J.4.

25. S. Yi, R. Lingle, A. McCurdy, D. Peckham, R. Jensen, and L. Gruner-Nielsen, "Few-mode fibers for mode-division multiplexing," in *Photonics Society Summer Topical Meeting Series, 2013 IEEE*(2013), pp. 80-81.

26. C. Koebele, M. Salsi, D. Sperti, P. Tran, P. Brindel, H. Mardoyan, S. Bigo, A. Boutin, F. Verluise, and P. Sillard, "Two mode transmission at 2x100Gb/s, over 40km-long prototype few-mode fiber, using LCOS-based programmable mode multiplexer and demultiplexer," Optics express **19**, 16593-16600 (2011).

27. A. Li, X. Chen, A. Al Amin, J. Ye, and W. Shieh, "Space-division multiplexed high-speed superchannel transmission over few-mode fiber," Lightwave Technology, Journal of **30**, 3953-3964 (2012).

28. S. Randel, R. Ryf, A. Sierra, P. J. Winzer, A. H. Gnauck, C. A. Bolle, R.-J. Essiambre, D. W. Peckham, A. McCurdy, and R. Lingle, "6× 56-Gb/s mode-division multiplexed transmission

over 33-km few-mode fiber enabled by 6× 6 MIMO equalization," Optics Express **19**, 16697-16707 (2011).

29. R. Ryf, M. Mestre, S. Randel, C. Schmidt, A. Gnauck, R. Essiambre, P. Winzer, R. Delbue, P. Pupalaikis, and A. Sureka, "Mode-Multiplexed Transmission Over a 209-km DGD-Compensated Hybrid Few-Mode Fiber Span," Photonics Technology Letters, IEEE **24**, 1965-1968 (2012).

30. V. Sleiffer, P. Leoni, Y. Jung, J. Surof, M. Kuschnerov, V. Veljanovski, S. U. Alam, D. J. Richardson, L. GrÃ¼ner-Nielsen, and Y. Sun, "20x 960-Gb/s Space-division-multiplexed 32QAM transmission over 60 km few-mode fiber," Optics express **22**, 749-755 (2014).

31. V. A. J. M. Sleiffer, H. Chen, Y. Jung, P. Leoni, M. Kuschnerov, A. Simperler, H. Fabian, H. Schuh, F. Kub, D. J. Richardson, S. U. Alam, L. Grüner-Nielsen, Y. Sun, A. M. J. Koonen, and H. de Waardt, "Field demonstration of mode-division multiplexing upgrade scenarios on commercial networks," Optics Express **21**, 31036-31046 (2013).

32. M. Arikawa, E. Le Taillandier de Gabory, T. Ito, and K. Fukuchi, "Improvement of Signal Quality after Long-Haul Transmission over Multi-Core Fiber with Adaptive MIMO-FDE Using Time-Domain Coefficient Selection," in *Optical Fiber Communication Conference*(Optical Society of America, San Francisco, California, 2014), p. Th2A.38.

33. Y. Awaji, N. Wada, Y. Toda, and T. Hayashi, "World first mode/spatial division multiplexing in multi-core fiber using Laguerre-Gaussian mode," in *European Conference and Exposition on Optical Communications*(Optical Society of America, 2011), p. We. 10. P11. 55.

34. S. Chandrasekhar, A. Gnauck, X. Liu, P. Winzer, Y. Pan, E. C. Burrows, B. Zhu, T. Taunay, M. Fishteyn, and M. Yan, "WDM/SDM Transmission of 10 x 128-Gb/s PDM-QPSK over 2688-km 7-Core Fiber with a per-Fiber Net Aggregate Spectral-Efficiency Distance Product of 40,320 km. b/s/Hz," in *European Conference and Exposition on Optical Communications*(Optical Society of America, 2011), p. Th. 13. C. 14.

35. Q. Dayou, E. Ip, H. Ming-Fang, L. Ming-Jun, and W. Ting, "698.5-Gb/s PDM-2048QAM transmission over 3km multicore fiber," in *Optical Communication (ECOC 2013), 39th European Conference and Exhibition on*(2013), pp. 1-3.

36. A. H. Gnauck, S. Chandrasekhar, X. Liu, S. Randel, S. Corteselli, T. Taunay, B. Zhu, and M. Fishteyn, "WDM Transmission of 603-Gb/s Superchannels over 845 km of 7-Core Fiber with 42.2 b/s/Hz Spectral Efficiency," in *European Conference and Exhibition on Optical Communication*(Optical Society of America, Amsterdam, 2012), p. Th.2.C.2.

37. K. Igarashi, T. Tsuritani, I. Morita, Y. Tsuchida, K. Maeda, M. Tadakuma, T. Saito, K. Watanabe, K. Imamura, R. Sugizaki, and M. Suzuki, "1.03-Exabit/skm Super-Nyquist-

WDM transmission over 7,326-km seven-core fiber," in *Optical Communication (ECOC 2013), 39th European Conference and Exhibition on*(2013), pp. 1-3.

38. K. Imamura, H. Inaba, K. Mukasa, and R. Sugizaki, "19-core multi core fiber to realize high density space division multiplexing transmission," in *Photonics Society Summer Topical Meeting Series, 2012 IEEE*(2012), pp. 208-209.

39. T. Kobayashi, H. Takara, A. Sano, T. Mizuno, H. Kawakami, Y. Miyamoto, K. Hiraga, Y. Abe, H. Ono, M. Wada, Y. Sasaki, I. Ishida, K. Takenaga, S. Matsuo, K. Saitoh, M. Yamada, H. Masuda, and T. Morioka, "2x344 Tb/s propagation-direction interleaved transmission over 1500-km MCF enhanced by multicarrier full electric-field digital back-propagation," in *Optical Communication (ECOC 2013), 39th European Conference and Exhibition on*(2013), pp. 1-3.

40. M. Koshiba, "Recent progress in multi-core fibers for ultralarge-capacity transmission," in *OptoeElectronics and Communications Conference (OECC), 2010 15th*(2010), pp. 38-39.

41. E. Le Taillandier de Gabory, M. Arikawa, Y. Hashimoto, T. Ito, and K. Fukuchi, "A shared carrier reception and processing scheme for compensating frequency offset and phase noise of space-division multiplexed signals over multicore fibers," in *Optical Fiber Communication Conference*(Optical Society of America, 2013), p. OM2C. 2.

42. E. Le Taillandier De Gabory, M. Arikawa, T. Ito, and K. Fukuchi, "DWDM transmission of 128Gb/s PM-16QAM signal over 1815km of 7-core MCF using shared carrier reception for improving the received signal quality," in *Optical Communication (ECOC 2013), 39th European Conference and Exhibition on*(2013), pp. 1-3.

43. I. Morita, "Long-distance and high-capacity transmission with multicore fiber," in *Photonics Society Summer Topical Meeting Series, 2013 IEEE*(2013), pp. 127-128.

44. K. Mukasa, K. Imamura, Y. Tsuchida, and R. Sugizaki, "Multi-core fibers for large capacity SDM," in *Optical Fiber Communication Conference and Exposition (OFC/NFOEC), 2011 and the National Fiber Optic Engineers Conference*(2011), pp. 1-3.

45. K. Nakajima, Y. Goto, T. Matsui, and S. Tomita, "Multi-core fiber technologies for extremely advanced transmission," in *OptoeElectronics and Communications Conference (OECC), 2011 16th*(2011), pp. 248-249.

46. B. J. Puttnam, J.-M. Delgado-Mendinueta, J. Sakaguchi, R. S. Luis, W. Klaus, Y. Awaji, N. Wada, A. Kanno, and T. Kawanishi, "105Tb/s Transmission System Using Low-cost, MHz Linewidth DFB Lasers Enabled by Self-Homodyne Coherent Detection and a 19-Core Fiber," in *Optical Fiber Communication Conference*(Optical Society of America, 2013), p. OW1I. 1.

47. D. Qian, E. Ip, M.-F. Huang, M.-j. Li, A. Dogariu, S. Zhang, Y. Shao, Y.-K. Huang, Y. Zhang, X. Cheng, Y. Tian, P. Ji, A. Collier, Y. Geng, J. Linares, C. Montero, V. Moreno, X. Prieto, and T. Wang, "1.05Pb/s Transmission with 109b/s/Hz Spectral Efficiency using Hybrid Single- and Few-Mode Cores," in *Frontiers in Optics 2012/Laser Science XXVIII*(Optical Society of America, Rochester, New York, 2012), p. FW6C.3.

48. J. Sakaguchi, Y. Awaji, N. Wada, A. Kanno, T. Kawanishi, T. Hayashi, T. Taru, T. Kobayashi, and M. Watanabe, "109-Tb/s (7x97x172-Gb/s SDM/WDM/PDM) QPSK transmission through 16.8-km homogeneous multi-core fiber," in *Optical Fiber Communication Conference/National Fiber Optic Engineers Conference 2011*(Optical Society of America, Los Angeles, California, 2011), p. PDPB6.

49. J. Sakaguchi, W. Klaus, B. J. Puttnam, J. M. D. Mendinueta, Y. Awaji, N. Wada, Y. Tsuchida, K. Maeda, M. Tadakuma, K. Imamura, R. Sugizaki, T. Kobayashi, Y. Tottori, M. Watanabe, and R. V. Jensen, "19-core MCF transmission system using EDFA with shared core pumping coupled in free-space optics," in *Optical Communication (ECOC 2013), 39th European Conference and Exhibition on*(2013), pp. 1-3.

50. J. Sakaguchi, B. J. Puttnam, W. Klaus, Y. Awaji, N. Wada, A. Kanno, T. Kawanishi, K. Imamura, H. Inaba, and K. Mukasa, "19-core fiber transmission of 19x100x172-Gb/s SDM-WDM-PDM-QPSK signals at 305Tb/s," in *National Fiber Optic Engineers Conference*(Optical Society of America, 2012), p. PDP5C. 1.

51. J. Sakaguchi, B. J. Puttnam, W. Klaus, J.-M. Delgado-Mendinueta, Y. Awaji, N. Wada, A. Kanno, and T. Kawanishi, "Large-capacity transmission over a 19-core fiber," in *Optical Fiber Communication Conference*(Optical Society of America, 2013), p. OW1I. 3.

52. T. Sakamoto, K. Saitoh, N. Hanzawa, K. Tsujikawa, M. Lin, M. Koshiba, and F. Yamamoto, "Crosstalk suppressed hole-assisted 6-core fiber with cladding diameter of 125 μm," in *Optical Communication (ECOC 2013), 39th European Conference and Exhibition on*(2013), pp. 1-3.

53. Y. Sasaki, K. Takenaga, Y. Arakawa, S. Tanigawa, S. Matsuo, K. Saitoh, and M. Koshiba, "Large-effective-area uncoupled 10-core fiber with two-pitch layout," in *Optical Fiber Communication Conference*(Optical Society of America, 2012), p. OM2D. 4.

54. H. Takahashi, K. Igarashi, and T. Tsuritani, "Long-haul transmission using multicore fibers," in *Optical Fiber Communication Conference*(Optical Society of America, San Francisco, California, 2014), p. Tu2J.2.

55. H. Takara, "Multi-core fiber transmission technologies for Peta b/s per fiber capacity," in *Optical Communication (ECOC 2013), 39th European Conference and Exhibition on*(2013), pp. 1-3.

56. H. Takara, "Ultra-large-capacity multi-core fiber transmission technologies," in *Photonics Society Summer Topical Meeting Series, 2013 IEEE*(2013), pp. 133-134.

57. H. Uemura, Y. Sasaki, S. Nishimoto, T. Uematsu, K. Takenaga, K. Omichi, R. Goto, S. Matsuo, and K. Saitoh, "Mode Multiplexer/Demultiplexer Based on a Partially Elongated Multi-Core Fiber," in *Optical Fiber Communication Conference*(Optical Society of America, San Francisco, California, 2014), p. Tu3D.3.

58. B. Zhu, X. Liu, S. Chandrasekhar, T. Taunay, M. Fishteyn, M. Yan, J. M. Fini, E. Monberg, and F. Dimarcello, "112-Tb/s (7x160x107Gb/s) space-division multiplexed DWDM transmission over a 76.8-km multicore Fiber," in *European Conference and Exposition on Optical Communications*(Optical Society of America, 2011), p. Tu. 5. B. 5.

59. S. Chandrasekhar, A. Gnauck, X. Liu, P. Winzer, Y. Pan, E. Burrows, T. Taunay, B. Zhu, M. Fishteyn, and M. Yan, "WDM/SDM transmission of 10 x 128-Gb/s PDM-QPSK over 2688-km 7-core fiber with a per-fiber net aggregate spectral-efficiency distance product of 40,320 km· b/s/Hz," Optics express **20**, 706-711 (2012).

60. J. H. Chang, H. G. Choi, and Y. C. Chung, "Achievable capacity improvement by using multi-level modulation format in trench-assisted multi-core fiber system," Optics Express **21**, 14262-14271 (2013).

61. K. Igarashi, K. Takeshima, T. Tsuritani, H. Takahashi, S. Sumita, I. Morita, Y. Tsuchida, M. Tadakuma, K. Maeda, T. Saito, K. Watanabe, K. Imamura, R. Sugizaki, and M. Suzuki, "110.9-Tbit/s SDM transmission over 6,370 km using a full C-band seven-core EDFA," Optics Express **21**, 18053-18060 (2013).

62. K. Igarashi, T. Tsuritani, I. Morita, Y. Tsuchida, K. Maeda, M. Tadakuma, T. Saito, K. Watanabe, K. Imamura, and R. Sugizaki, "Super-Nyquist-WDM transmission over 7,326-km seven-core fiber with capacity-distance product of 1.03 Exabit/s· km," Optics express **22**, 1220-1228 (2014).

63. S. Matsuo, Y. Sasaki, T. Akamatsu, I. Ishida, K. Takenaga, K. Okuyama, K. Saitoh, and M. Kosihba, "12-core fiber with one ring structure for extremely large capacity transmission," Optics express **20**, 28398-28408 (2012).

64. S. Naderi Shahi, and S. Kumar, "A multi-core or multi-fiber WDM system," Optics Communications **294**, 289-293 (2013).

65. J. Sakaguchi, Y. Awaji, N. Wada, A. Kanno, T. Kawanishi, T. Hayashi, T. Taru, T. Kobayashi, and M. Watanabe, "Space division multiplexed transmission of 109-Tb/s data signals using homogeneous seven-core fiber," Lightwave Technology, Journal of **30**, 658-665 (2012).

66. J. Sakaguchi, B. J. Puttnam, W. Klaus, Y. Awaji, N. Wada, A. Kanno, T. Kawanishi, K. Imamura, H. Inaba, K. Mukasa, R. Sugizaki, T. Kobayashi, and M. Watanabe, "305 Tb/s Space Division Multiplexed Transmission Using Homogeneous 19-Core Fiber," Lightwave Technology, Journal of **31**, 554-562 (2013).

67. A. Sano, H. Takara, T. Kobayashi, H. Kawakami, H. Kishikawa, T. Nakagawa, Y. Miyamoto, Y. Abe, H. Ono, K. Shikama, M. Nagatani, T. Mori, Y. Sasaki, I. Ishida, K. Takenaga, S. Matsuo, K. Saitoh, M. Koshiba, M. Yamada, H. Masuda, and T. Morioka, "409-Tb/s + 409-Tb/s crosstalk suppressed bidirectional MCF transmission over 450 km using propagation-direction interleaving," Optics Express **21**, 16777-16783 (2013).

68. H. Takara, H. Ono, Y. Abe, H. Masuda, K. Takenaga, S. Matsuo, H. Kubota, K. Shibahara, T. Kobayashi, and Y. Miaymoto, "1000-km 7-core fiber transmission of 10 x 96-Gb/s PDM-16QAM using Raman amplification with 6.5 W per fiber," Optics express **20**, 10100-10105 (2012).

69. K. Takenaga, Y. Arakawa, Y. Sasaki, S. Tanigawa, S. Matsuo, K. Saitoh, and M. Koshiba, "A large effective area multi-core fiber with an optimized cladding thickness," Optics express **19**, B543-B550 (2011).

70. B. Zhu, J. M. Fini, M. F. Yan, X. Liu, S. Chandrasekhar, T. F. Taunay, M. Fishteyn, E. M. Monberg, and F. V. Dimarcello, "High-capacity space-division-multiplexed DWDM transmissions using multicore fiber," Lightwave Technology, Journal of **30**, 486-492 (2012).

71. B. Zhu, T. Taunay, M. Fishteyn, X. Liu, S. Chandrasekhar, M. Yan, J. Fini, E. Monberg, and F. Dimarcello, "112-Tb/s space-division multiplexed DWDM transmission with 14-b/s/Hz aggregate spectral efficiency over a 76.8-km seven-core fiber," Optics Express **19**, 16665-16671 (2011).

72. N. Bai, "Mode-division Multiplexed Transmission in Few-mode Fibers," (University of Central Florida Orlando, Florida, 2013).

73. G. Li, N. Bai, N. Zhao, and C. Xia, "Space-division multiplexing: the next frontier in optical communication," Adv. Opt. Photon. **6**, 413-487 (2014).

74. D. Richardson, J. Fini, and L. Nelson, "Space-division multiplexing in optical fibres," Nature Photonics **7**, 354-362 (2013).

75. P. J. Winzer, "Optical networking beyond WDM," Photonics Journal, IEEE **4**, 647-651 (2012).

76. P. J. Winzer, "Spatial multiplexing: The next frontier in network capacity scaling," in *Optical Communication (ECOC 2013), 39th European Conference and Exhibition on*(2013), pp. 1-4.

77. L. Ming-Jun, B. Hoover, V. N. Nazarov, and D. L. Butler, "Multicore fiber for optical interconnect applications," in *Opto-Electronics and Communications Conference (OECC), 2012 17th*(2012), pp. 564-565.

78. V. Francois, and F. Laramee, "Multicore Fiber Optimization for Application to Chip-to-Chip Optical Interconnects," Lightwave Technology, Journal of **31**, 4022-4028 (2013).

79. B. Zhu, T. Taunay, M. Yan, J. Fini, M. Fishteyn, E. Monberg, and F. Dimarcello, "Seven-core multicore fiber transmissions for passive optical network," Optics Express **18**, 11117-11122 (2010).

80. K. Saitoh, M. Koshiba, K. Takenaga, and S. Matsuo, "Crosstalk and core density in uncoupled multicore fibers," Photonics Technology Letters, IEEE **24**, 1898-1901 (2012).

81. K. Saitoh, and S. Matsuo, "Multicore fibers for large capacity transmission," Nanophotonics **2**, 441-454 (2013).

82. T. Hayashi, T. Taru, O. Shimakawa, T. Sasaki, and E. Sasaoka, "Ultra-low-crosstalk multi-core fiber feasible to ultra-long-haul transmission," in *National Fiber Optic Engineers Conference*(Optical Society of America, 2011), p. PDPC2.

83. K. Imamura, K. Mukasa, and R. Sugizaki, "Trench assisted multi-core fiber with large Aeff over 100 μm^2 and low attenuation loss," in *European Conference and Exposition on Optical Communications*(Optical Society of America, 2011), p. Mo. 1. LeCervin. 1.

84. K. Takenaga, Y. Arakawa, S. Tanigawa, N. Guan, S. Matsuo, K. Saitoh, and M. Koshiba, "Reduction of crosstalk by trench-assisted multi-core fiber," in *Optical Fiber Communication Conference*(Optical Society of America, 2011), p. OWJ4.

85. H. Takara, A. Sano, T. Kobayashi, H. Kubota, H. Kawakami, A. Matsuura, Y. Miyamoto, Y. Abe, H. Ono, and K. Shikama, "1.01-Pb/s (12 SDM/222 WDM/456 Gb/s) crosstalk-managed transmission with 91.4-b/s/Hz aggregate spectral efficiency," in *European Conference and Exhibition on Optical Communication*(Optical Society of America, 2012), p. Th. 3. C. 1.

86. D. Gloge, "Weakly Guiding Fibers," Appl. Opt. **10**, 2252-2258 (1971).

87. S. Berdagué, and P. Facq, "Mode division multiplexing in optical fibers," Appl. Opt. **21**, 1950-1955 (1982).

88. N. Bai, E. Ip, Y.-K. Huang, E. Mateo, F. Yaman, M.-J. Li, S. Bickham, S. Ten, J. Liñares, and C. Montero, "Mode-division multiplexed transmission with inline few-mode fiber amplifier," Optics express **20**, 2668-2680 (2012).

89. N. Bai, and G. Li, "Equalizer tap length requirement for mode group delay-compensated fiber link with weakly random mode coupling," Optics express **22**, 4247-4255 (2014).

90. B. Neng, and L. Guifang, "Adaptive Frequency-Domain Equalization for Mode-Division Multiplexed Transmission," Photonics Technology Letters, IEEE **24**, 1918-1921 (2012).

91. L. Grüner-Nielsen, Y. Sun, J. W. Nicholson, D. Jakobsen, K. G. Jespersen, R. Lingle Jr, and B. Pálsdóttir, "Few mode transmission fiber with low DGD, low mode coupling, and low loss," Journal of Lightwave Technology **30**, 3693-3698 (2012).

92. R. Ryf, S. Randel, A. H. Gnauck, C. Bolle, A. Sierra, S. Mumtaz, M. Esmaeelpour, E. C. Burrows, R.-J. Essiambre, and P. J. Winzer, "Mode-division multiplexing over 96 km of few-mode fiber using coherent 6x6 MIMO processing," Lightwave Technology, Journal of **30**, 521-531 (2012).

93. T. Sakamoto, T. Mori, T. Yamamoto, L. Ma, N. Hanzawa, S. Aozasa, K. Tsujikawa, and S. Tomita, "Transmission over large-core few-mode photonic crystal fiber using distance-independent modal dispersion compensation technique," Optics express **19**, B478-B485 (2011).

94. T. Sakamoto, T. Mori, T. Yamamoto, and S. Tomita, "Differential Mode Delay Managed Transmission Line for WDM-MIMO System Using Multi-Step Index Fiber," Lightwave Technology, Journal of **30**, 2783-2787 (2012).

95. S. G. Leon-Saval, N. K. Fontaine, J. R. Salazar-Gil, B. Ercan, R. Ryf, and J. Bland-Hawthorn, "Mode-selective photonic lanterns for space-division multiplexing," Optics express **22**, 1036-1044 (2014).

96. S. Yerolatsitis, and T. A. Birks, "Tapered mode multiplexers based on standard single-mode fibre," in *Optical Communication (ECOC 2013), 39th European Conference and Exhibition on*(2013), pp. 1-3.

97. S. Yerolatsitis, I. Gris-SÃ¡nchez, and T. A. Birks, "Adiabatically-tapered fiber mode multiplexers," Optics express **22**, 608-617 (2014).

98. N. Bai, E. Ip, T. Wang, and G. Li, "Multimode fiber amplifier with tunable modal gain using a reconfigurable multimode pump," Optics express **19**, 16601-16611 (2011).

99. G. Le Cocq, Y. Quiquempois, A. Le Rouge, G. Bouwmans, H. El Hamzaoui, K. Delplace, M. Bouazaoui, and L. Bigot, "Few mode Er3+ doped fiber with micro-structured core for mode division multiplexing in the C-band," Optics Express **21**, 31646-31659 (2013).

100. F. Ferreira, D. Fonseca, A. Lobato, B. Inan, and H. Silva, "Reach Improvement of Mode Division Multiplexed Systems Using Fiber Splices," Photonics Technology Letters, IEEE **25**, 1091-1094 (2013).

101. T. Hayashi, T. Taru, O. Shimakawa, T. Sasaki, and E. Sasaoka, "Design and fabrication of ultra-low crosstalk and low-loss multi-core fiber," Optics express **19**, 16576-16592 (2011).

102. X. Cen, R. Amezcua-Correa, B. Neng, E. Antonio-Lopez, D. May-Arrioja, A. Schulzgen, M. Richardson, J. Linares, C. Montero, E. Mateo, Z. Xiang, and L. Guifang, "Low-crosstalk few-mode multi-core fiber for high-mode-density space-division multiplexing," in *Optical Communications (ECOC), 2012 38th European Conference and Exhibition on*(2012), pp. 1-3.

103. X. Cen, R. Amezcua-Correa, B. Neng, E. Antonio-Lopez, D. May-Arriojo, A. Schulzgen, M. Richardson, J. Linares, C. Montero, E. Mateo, Z. Xiang, and L. Guifang, "Hole-assisted few-mode multi-core fiber for high-density space-division multiplexing," in *Photonics Society Summer Topical Meeting Series, 2012 IEEE*(2012), pp. 206-207.

104. C. Xia, R. Amezcua-Correa, N. Bai, E. Antonio-Lopez, D. M. Arrioja, A. Schulzgen, M. Richardson, J. Liñares, C. Montero, and E. Mateo, "Hole-assisted few-mode multicore fiber for high-density space-division multiplexing," Photonics Technology Letters, IEEE **24**, 1914-1917 (2012).

105. K. Saitoh, T. Matsui, T. Sakamoto, M. Koshiba, and S. Tomita, "Multi-core hole-assisted fibers for high core density space division multiplexing," in *OECC 2010 Technical Digest*(2010).

106. K. Okamoto, *Fundamental of optical waveguides* (Academic Press, 2005).

107. R. G. H. van Uden, R. A. Correa, E. A. Lopez, F. M. Huijskens, XiaC, LiG, SchülzgenA, H. de Waardt, A. M. J. Koonen, and C. M. Okonkwo, "Ultra-high-density spatial division multiplexing with a few-mode multicore fibre," Nat Photon **8**, 865-870 (2014).

108. J. K. Butler, D. E. Ackley, and D. Botez, "Coupled-mode analysis of phase-locked injection laser arrays," App. Phy. Lett. **44**, 293-295 (1984).

109. E. Kapon, J. Katz, and A. Yariv, "Supermode analysis of phase-locked arrays of semiconductor lasers," Opt. Lett. **9**, 125-127 (1984).

110. A. Hardy, and W. Streifer, "Coupled modes of multiwaveguide systems and phased arrays," J. Lightw. Technol. **4**, 90-99 (1986).

111. C. N. Alexeyev, A. V. Volyar, and M. A. Yavorsky, "Linear azimuthons in circular fiber arrays and optical angular momentum of discrete optical vortices," Phys. Rev. A **80**, 063821 (2009).

112. C. N. Alexeyev, A. V. Volyar, and M. A. Yavorsky, "Energy transfer, orbital angular momentum, and discrete current in a double-ring fiber array," Phys. Rev. A **84**, 063845 (2011).

113. J. Zhou, "Analytical formulation of super-modes inside multi-core fibers with circularly distributed cores," Opt. Exp. **22**, 673-688 (2014).

114. N. Bai, and G. Li, "Adaptive frequency-domain equalization for mode-division multiplexed transmission," Photonics Technology Letters, IEEE **24**, 1918-1921 (2012).

115. N. Bai, C. Xia, and G. Li, "Adaptive frequency-domain equalization for the transmission of the fundamental mode in a few-mode fiber," Optics express **20**, 24010-24017 (2012).

116. C. Xia, N. Bai, I. Ozdur, X. Zhou, and G. Li, "Supermodes for optical transmission," Opt. Exp. **19**, 16653-16664 (2011).

117. R. Ryf, R. J. Essiambre, S. Randel, M. A. Mestre, C. Schmidt, and P. J. Winzer, "Impulse response analysis of coupled-core 3-core fibers," in *Proc. IEEE European Conference on Optical Communication*(2012), p. Mo. 1. F. 4.

118. G. Li, X. Cen, and B. Neng, "Systems And Methods For Optical Transmission Using Supermodes," (Google Patents, 2012).

119. C. Xia, N. Bai, R. Amezcua-Correa, E. Antonio-Lopez, A. Schulzgen, M. Richardson, X. Zhou, and G. Li, "Supermodes in strongly-coupled multi-core fibers," in *Proc. IEEE Optical Fiber Communication Conference*(Optical Society of America, 2013), p. OTh3K. 5.

120. N. Kishi, and E. Yamashita, "A simple coupled-mode analysis method for multiple-core optical fiber and coupled dielectric waveguide structures," in *Microwave Symposium Digest, 1988., IEEE MTT-S International*(IEEE, 1988), pp. 739-742.

121. A. W. Snyder, "Coupled-mode theory for optical fibers," JOSA **62**, 1267-1277 (1972).

122. H. Kubota, H. Takara, T. Nakagawa, M. Matsui, and T. Morioka, "Intermodal group velocity dispersion of few-mode fiber," IEICE Electronics Express **7**, 1552-1556 (2010).

123. A. Yariv, and Yeh, P., *Photonics : optical electronics in modern communications* (Oxford University Press, 2007).

124. K. Okamoto, *Fundamentals of Optical Waveguides* (Academic Press, 2006).

125. J. Nicholson, A. Yablon, S. Ramachandran, and S. Ghalmi, "Spatially and spectrally resolved imaging of modal content in large-mode-area fibers," Opt. Exp. **16**, 7233-7243 (2008).

126. M. Fujiwara, K.-I. Suzuki, N. Yoshimoto, M. Oguma, and S. Soma, "Increasing splitting ratio of 10Gb/s-class PONs by using FW-DMF that acts as low loss splitter for upstream and conventional splitter for downstream," in *Optical Fiber Communications Conference and Exhibition (OFC), 2014*(IEEE, 2014), pp. 1-3.

127. C. Ning, L. Zhenxing, and F. J. Effenberger, "Large splitting and long reach passive optical networks with mode coupling receivers," in *Optical Communication (ECOC), 2010 36th European Conference and Exhibition on*(2010), pp. 1-3.

128. C. Xia, A. M. Velázquez-Benítez, J. E. A. Lopez, W. He, A. Schülzgen, F. Effenburger, R. A. Correa, and G. Li, "TDMA Few-Mode Passive Optical Network," in *Asia Communications and Photonics Conference*(Optical Society of America, 2014), p. ATh2F. 2.

129. C. Xia, N. Chand, A. Velázquez-Benítez, Z. Yang, X. Liu, J. E. Antonio-Lopez, H. Wen, B. Zhu, N. Zhao, and F. Effenberger, "Time-division-multiplexed few-mode passive optical network," Optics express **23**, 1151-1158 (2015).

130. C. L. Xia, Xiang; Wen, He; Zhu, Benyuan; Li, Guifang et al., "Demonstration of World's first Few-mode GPON," ECOC 2014 **Postdeadline Paper** (2014).

131. N. K. Fontaine, S. G. Leon-Saval, R. Ryf, J. R. S. Gil, B. Ercan, and J. Bland-Hawthorn, "Mode-selective dissimilar fiber photonic-lantern spatial multiplexers for few-mode fiber," in *Optical Communication (ECOC 2013), 39th European Conference and Exhibition on*(2013), pp. 1-3.

132. S. Randel, R. Ryf, C. Schmidt, M. A. Mestre, P. J. Winzer, and R. Essiambre, "MIMO processing for space-division multiplexed transmission," in *Signal Processing in Photonic Communications*(Optical Society of America, 2012), p. SpW3B. 4.

133. B. Huang, C. Xia, G. Matz, N. Bai, and G. Li, "Structured directional coupler pair for multiplexing of degenerate modes," in *National Fiber Optic Engineers Conference*(Optical Society of America, 2013), p. JW2A. 25.

134. G. Labroille, B. Denolle, P. Jian, P. Genevaux, N. Treps, and J.-F. Morizur, "Efficient and mode selective spatial mode multiplexer based on multi-plane light conversion," Optics express **22**, 15599-15607 (2014).

135. N. K. Fontaine, R. Ryf, J. Bland-Hawthorn, and S. G. Leon-Saval, "Geometric requirements for photonic lanterns in space division multiplexing," Optics express **20**, 27123-27132 (2012).

136. F. Ferreira, D. Fonseca, and H. Silva, "Design of Few-Mode Fibers With Arbitrary and Flattened Differential Mode Delay," Photonics Technology Letters, IEEE **25**, 438-441 (2013).

137. A. M. Velazquez-Benitez, J. C. Alvarado-Zacarias, G. Lopez-Galmiche, E. Antonio-Lopez, A. Schülzgen, D. Van Ras, P. Sillard, C. M. Okonkwo, and R. Amezcua-Correa, "Six Spatial Modes Photonic Lanterns," in *Optical Fiber Communication Conference*(Optical Society of America, 2015), p. W3B. 3.